POLITECHNIKA POZNAŃSKA

WYDZIAŁ INŻYNIERII MATERIAŁOWEJ I FIZYKI TECHNICZNEJ

INSTYTUT INŻYNIERII MATERIAŁOWEJ

ROZPRAWA DOKTORSKA

Analiza przemian fazowych oraz funkcjonalizacja stopów trójskładnikowych Ti-Nb-Zr poprzez tworzenie układów kompozytowych oraz modyfikacje powierzchni

mgr inż. Mateusz MARCZEWSKI

Promotor*:* prof. dr hab. Mieczysław Jurczyk

Promotor pomocniczy: dr hab. inż. Andrzej Miklaszewski, prof. PP

Poznań, 2021

SPIS TREŚCI

STRESZCZENIE PRACY

Cel: Celem badań była synteza stopów o strukturze β oraz pseudo β w układzie trójskładnikowym Ti-Zr-Nb metodą mechanicznej syntezy i metalurgii proszków. Stopy poddano następnie modyfikacji w zakresie wytwarzania układów kompozytowych oraz elektrochemicznej obróbki powierzchni. Cele szczegółowe obejmowały: (a) syntezę oraz analizę porównawczą 9 stopów o ultra drobnoziarnistej mikrostrukturze o różnej zawartości niobu (od 16 do 34% at.) oraz cyrkonu (od 14 do 30% at.) otrzymanych metodą mechanicznej syntezy oraz prasowania na zimno i spiekania, (b) syntezę oraz analizę porównawczą wybranego dwufazowego stopu α+β oraz jednofazowego stopu β, otrzymanych metodą prasowania na zimno oraz spiekania, w odniesieniu do stopów prasowanych na gorąco, (c) syntezę kompozytów, zawierających Bioszkło 45S5 (BG) wraz ze srebrem, miedzią lub cynkiem wraz ze zbadaniem ich właściwości, w tym właściwości bakteriobójczych oraz biologicznych, (d) modyfikację powierzchni poprzez trawienie oraz osadzanie elektrochemiczne mieszaniny wodorotlenku wapnia z hydroksyapatytem oraz charakterystykę właściwości wytworzonej warstwy powierzchniowej.

Metoda: Stopy trójskładnikowe Ti-Zr-Nb oraz ich kompozyty, zawierające od 3 do 9% wag. Bioszkła 45S5 oraz 1% wag. dodatku srebra, miedzi lub cynku, zostały wytworzone metodą mechanicznej syntezy. Modyfikację powierzchniową wykonano dwuetapowo poprzez trawienie elektrochemiczne w wodnym roztworze kwasu fosforowego (V) i kwasu fluorowodorowego, a następnie osadzanie elektrochemiczne w wodnym roztworze azotanu wapnia, wodorofosforanu amonu oraz kwasu chlorowodorowego. Otrzymane biomateriały zostały zbadane z wykorzystaniem dyfraktometru rentgenowskiego celem analizy strukturalnej, nanoindentera i twardościomierza celem analizy właściwości mechanicznych, potencjostatu-galwanostatu celem analizy odporności korozyjnej, mikroskopu świetlnego oraz skaningowego celem analizy mikrostruktury oraz technik osadzanej kropli celem wyznaczenia kątów zwilżalności. Wykonano ponadto badania aktywności bakteriobójczej oraz testy biologiczne *in vitro* wytworzonych materiałów.

Wyniki: Zr oraz Nb jako stabilizatory fazy Ti(β) umożliwiły wytworzenie struktury jednofazowej stopów. Wykorzystanie procesu mechanicznej syntezy prowadzi do uzyskania ultra drobnoziarnistej mikrostruktury. Kompozyty, zawierające Bioszkło 45S5 wykazują obniżony moduł Younga oraz lepsze właściwości korozyjne. Dodatek 1% wag. srebra, miedzi lub cynku poprawia właściwości bakteriobójcze względem kultury typu *S. mutans* w odniesieniu do mikrokrystalicznego Ti. Modyfikacja powierzchniowa poprzez wytworzenie powłoki wodorotlenku wapnia i hydroksyapatytu poprawia odporność korozyjną oraz zwilżalność stopu, co wpływa na wzrost komórek kostnych. Proliferacja komórek kostnych (osteoblastów i fibroblastów) na wytworzonych materiałach jest wyższa lub równa w porównaniu z wzorcową próbką komercyjnie czystego tytanu (Grade 2).

Wnioski: Wytworzone stopy Ti-Zr-Nb, jak i również ich biokompozyty z ultra drobnoziarnistą mikrostrukturą posiadają interesujące właściwości mając na uwadze ich ewentualne zastosowanie na implanty tkanki twardej, tj. implanty stomatologiczne lub endoprotezy stawu biodrowego. Zaobserwowano wzrost mikrotwardości i wyraźne obniżenie modułu Younga względem mikrokrystalicznego Ti. Funkcjonalizacja stopu przez tworzenie kompozytów lub obróbkę powierzchniową, prowadzi do poprawy odporności korozyjnej, właściwości hydrofilowych oraz redukcji modułu Younga.

ABSTRACT

Aim: The aims of this thesis were to produce ternary Ti-Zr-Nb alloys with β and pseudo-β structure by the mechanical alloying approach. The produced alloys were modified by the composite formation and electrochemical surface modification. The detailed aims included: (a) the formation and the comparative analysis of 9 ultrafine-grained alloys with niobium (from 16 to 34 at. %) and zirconium (from 14 to 30 at. %) content produced with the mechanical alloying and consolidated with cold pressing and sintering approach, (b) the formation and the comparative analysis of the selected dual-phase α+β and single-phase β alloys produced by conventional cold pressing with sintering, and hot pressing approach, (c) composite formation with 45S5 Bioglass (BG) and silver, copper, or zinc content and their characterization with antibacterial activity and biological tests included, (d) surface modification with electrochemical etching and electrochemical deposition of the calcium hydroxide and hydroxyapatite mixture and the evaluation of so produced coating.

Methods: Ternary Ti-Zr-Nb alloys and the composites with 45S5 Bioglass (from 3 to 9 wt. %) and 1 wt. % silver, copper, or zinc content were produced with the mechanical alloying approach. Electrochemical surface modification was done at two stages, with the first stage of electrochemical etching in the solution of orthophosphoric acid and hydrogen fluoride and the second stage of electrochemical deposition in the solution of calcium nitrate, diammonium phosphate, and hydrogen chloride. The produced alloys were examined with the use of an X-ray diffractometer for crystallographic analysis, nanoindenter and microhardness tester for the mechanical properties analysis, potentiostat for corrosion tests, optical and scanning electron microscope for the structure analysis, and the drop shape analyzer for the wettability tests. Materials were additionally tested for their antibacterial activity and biological properties.

Results: Zr and Nb as β-stabilizer has been proved to form a single-phase structure in the right composition range and process conditions. Moreover, the use of mechanical alloying has lead to ultrafine-grained structure formation. The composites with 45S5 Bioglass addition have lower Young modulus and better corrosion properties than the base material. The addition of silver can additionally improve corrosion properties. 1 wt. % of silver, copper, and zinc addition has revealed the high antibacterial activity against *S. mutans*. Surface modification with the calcium hydroxide and hydroxyapatite coating deposition has lead to the corrosion properties and wettability improvement, which should further impact the bone tissue growth on the materials' surface. The proliferation of the bone cells (both osteoblasts and fibroblasts) all the produced materials was equal or even better than that of commercially pure titanium Grade 2.

Conclusions: All studies have proved Ti-Zr-Nb and their biocomposites attractive in the hard tissue implants as dental or hip implants. Moreover, eliminating toxic aluminum and vanadium (present in Ti6Al4V) from the materials composition does not provide the degradation of the materials' properties as hardness. On the other hand, some of the properties were improved as reduced Young's modulus in contrast to the pure titanium. Moreover, further functionalization was proposed as surface and composite functionalization leading to the improvement of corrosion properties, wettability, and reduction of Young's modulus to the values closer to the bones.

1. Wstęp

Stopy tytanu, a w szczególności stop Ti6Al4V, zawierający aluminium oraz wanad, należą do najczęściej wybieranych materiałów na implanty tkanki twardej. Do elementów, wytworzonych ze stopów tytanu, które mają mieć trwały kontakt z ustrojem ludzkim należą między innymi zespolenia kostne, śruby stabilizujące, implanty stomatologiczne, czy trzon endoprotezy kości udowej [1]. Medycyna (w tym ortopedia) wymaga coraz lepszych rozwiązań ze względu na starzejące się społeczeństwo. W 2017 roku 13% światowej populacji stanowili ludzie w wieku powyżej 60 roku życia (wskaźnik ten wynosi aż 25% dla Europy). Przy ciągłym przewidywalnym wzroście 3% rocznie ilość osób w tym wieku może wzrosnąć do 25% w roku 2050 z wyjątkiem Afryki [2]. Zaburzenia układu mięśniowo-szkieletowego dotyczą głównie osób w starszym wieku, co wymusza poszukiwanie coraz to lepszych i skuteczniejszych rozwiązań, umożliwiających ciągłą poprawę warunków i komfortu życia [2,3]. Jednym z nich jest próba zastąpienia stopu Ti6Al4V stopami tytanu o lepszych właściwościach użytkowych w kontekście ich zastosowania w medycynie. Jest to możliwe poprzez wytworzenie stopów β, które po stopach α, w tym czystego technicznie tytanu, oraz stopach α+β, w tym wspomnianego stopu Ti6Al4V, stanowią kolejną generację stopów tytanu [1,4–6]. Umożliwiają one wyeliminowanie toksycznego aluminium oraz wanadu, które wykazują właściwości neurodegeneracyjne, prowadząc do powstania schorzeń, takich jak choroba Alzheimera i Parkinsona [7–9]. Zastąpienie tych elementów pierwiastkami jak niob i cyrkon umożliwia poprawę biokompatybilności tych stopów [10]. Stopy typu β charakteryzują się niższą wartością modułu Younga względem stopów poprzednich generacji, znacznie bardziej zbliżonych do kości. Lepsze dopasowanie właściwości mechanicznych implantu oraz kości prowadzi do ograniczenia występowania zjawiska. tzw. „stress shielding", w którym niedostatecznie obciążona kość ulega resorpcji oraz prowadzi do poluzowania implantu, co wymusza konieczność powtórnej implantacji [11].

Stopy β, zawierające dodatki w postaci stabilizatorów fazy β, czyli takich, które prowadzą do obniżenia temperatury przemiany alotropowej α⇌β, wynoszącej dla czystego tytanu 882°C. Ti(α) jest to odmiana alotropowa tytanu, występująca w strukturze krystalicznej heksagonalnej zwartej w grupie symetrii P63/mmc, natomiast Ti(β) w strukturze regularnej przestrzennie centrowanej w grupie symetrii Im-3m [1,12–14]. Stopy β mogą występować w układach dwu-, trój-, cztero- lub więcej składnikowych. Do układów dwuskładnikowych należą między innymi takie stopy jak Ti-Nb lub Ti-Mo, do układów trójskładnikowych

Ti-Zr-Nb lubTi-Nb-Mo, do układów czteroskładnikowych Ti-Nb-Ta-Zr [6]. Stopy Ti-Zr-Nb w szerokim zakresie składów chemicznych otrzymywane metodą mechanicznej syntezy nie zostały wcześniej dostatecznie zbadane. Wykorzystanie metod metalurgii proszków, polegających na poddaniu materiału proszkowego powtarzającym się procesom zgrzewania na zimno, kruszenia oraz ponownego zgrzewania w wysokoenergetycznych młynkach, daje możliwość szerokiej modyfikacji właściwości stopów. Związane jest to ze znacznym rozdrobnieniem struktury materiału względem metod tradycyjnych takich jak topienie łukowe, prowadząc do wytworzenia materiałów o wielkości elementów mikrostruktury nawet poniżej 100 nm. Reakcje pomiędzy wyjściowymi proszkami mogą zachodzić w niskiej temperaturze, w tym pokojowej, ograniczając zastosowanie wysokiej temperatury tylko do konsolidacji otrzymanych materiałów [15]. Dotychczasowe próby wytworzenia tej grupy stopów obejmowały wybrane składy chemiczne, takie jak Ti20Nb13Zr (% at.) [16].

Poprawę właściwości stopów można uzyskać również poprzez tworzenie układów kompozytowych. Dodatek Bioszkła 45S5 umożliwia, np. dalsze obniżanie modułu Younga, zwiększenie twardości, poprawę odporności korozyjnej oraz biokompatybilności w testach *in vitro* [17]. Tworzenie kompozytów na bazie układu Ti-Mo z dodatkiem bioceramiki połączone z modyfikacją warstwy wierzchniej przyczyniło się, jak donoszą badania, do znacznej poprawy właściwości badanych materiałów [18].

W zastosowaniu na implanty stomatologiczne, bardzo ważną rolę pełni mechanizm interakcji materiału z bakterią typu *S. mutans*, powodującej chorobę próchniczą zębów. Infekcja spowodowana adhezją patogenu do powierzchni wszczepu oraz jej późniejszy rozwój, mogą być powodem nieudanego zabiegu implantacji [19,20]. Z tego powodu, dość istotną rolą w projektowaniu materiałów na implanty stomatologiczne jest wykorzystanie pierwiastków bakteriobójczych. Należy do nich miedź, która wykazuje aktywność antyseptyczną jako dodatek do tytanu oraz innych stopów, w tym magnezu i żelaza (np. stal austenityczna) [21]. Cu charakteryzuje się również wysoką biokompatybilnością związaną z uwalnianiem niewielkiej ilości jonów Cu^{2+} [22]. Podobne zachowanie względem *S. mutans* wykazuje srebro [23,24] oraz cynk [25]. Każdy z tych pierwiastków może pełnić rolę czynnika bakteriobójczego nie tylko jako dodatkowy składnik stopu, ale również jako modyfikator powierzchni materiału [26–28].

Bardzo ważną rolę w procesie projektowania implantów, pełni ich warstwa powierzchniowa, mająca bardzo duży wpływ na ich ostateczną użyteczność oraz ryzyko ewentualnego niepowodzenia wszczepu [29]. Obok wspomnianych metod implantacji pierwiastków bakteriobójczych, istotną rolę pełnią również powłoki mające na celu zwiększenie

biokompatybilności. Jedną z grup są powłoki na bazie fosforanów wapnia (np. hydroksyapatytu), które mogą być nakładane z użyciem metod, takich jak natryskiwanie plazmowe, osadzanie elektroforetyczne [30], osadzanie hydrotermalne [31,32], osadzanie elektrochemiczne w tym wysokonapięciowe [33] lub biomimetyczne [34]. Ich wytwarzanie wpływa znacząco na poprawę procesu osteointegracji, czyli narastania tkanki kostnej w materiał [33,35]. Wodorotlenek wapnia wykazuje również działanie bakteriobójcze, co znajduje zastosowanie w stomatologii do sterylizacji kanałów korzeniowych [36–38].

W związku z powyższym, w ramach realizowanej pracy doktorskiej zostały wytworzone stopy trójskładnikowe Ti-Zr-Nb o szerokim zakresie koncentracji niobu oraz cyrkonu metodą mechanicznej syntezy, będące wcześniej przedmiotem badań, obejmujących jedynie pojedyncze składy chemiczne. Następnie celem dalszej poprawy ich właściwości, w tym aktywności bakteriobójczej oraz proliferacji komórek kostnych, materiały te zostały poddane dalszym modyfikacjom poprzez tworzenie układów kompozytowych zawierających Bioszkło 45S5 wraz ze srebrem miedzą lub cynkiem, a także obróbkę powierzchni z wytworzeniem powłok będących mieszaniną wodorotlenku wapnia oraz hydroksyapatytu.

[1]   M. Geetha, A.K. Singh, R. Asokamani, A.K. Gogia, Ti based biomaterials, the ultimate choice for orthopaedic implants - A review, Prog. Mater. Sci. 54 (2009) 397–425. https://doi.org/10.1016/j.pmatsci.2008.06.004.

[2]   M. Spector, Biomedical materials to meet the challenges of the aging epidemic, Biomed. Mater. 13 (2018). https://doi.org/10.1088/1748-605X/aab171.

[3]   V.M. Goldberg, J.A. Buckwalter, W.C. Hayes, K.J. Koval, Orthopaedic challenges in an aging population., Instr. Course Lect. 46 (1997) 417–422.

[4]   L.C. Zhang, L.Y. Chen, A Review on Biomedical Titanium Alloys: Recent Progress and Prospect, Adv. Eng. Mater. 21 (2019). https://doi.org/10.1002/adem.201801215.

[5]   M. Kaur, K. Singh, Review on titanium and titanium based alloys as biomaterials for orthopaedic applications, Mater. Sci. Eng. C. 102 (2019) 844–862. https://doi.org/10.1016/j.msec.2019.04.064.

[6]   M.T. Mohammed, Z.A. Khan, A.N. Siddiquee, Beta Titanium Alloys: The Lowest Elastic Modulus for Biomedical Applications: A Review Surface Modifications through FSP View project MACHINING View project, Int. J. Chem. Nucl. Metall. Mater. Eng. 8 (2014) 726–731. https://www.researchgate.net/publication/265396160.

[7]   L.S. Rhoads, W.T. Silkworth, M.L. Roppolo, M.S. Whittingham, Cytotoxicity of nanostructured vanadium oxide on human cells in vitro, Toxicol. Vitr. 24 (2010) 292–296. https://doi.org/10.1016/j.tiv.2009.08.010.

[8]   L.A. Dragan-Raileanu, C.E. Cotrutz, C. Munteanu, S. Strugaru, P. Avram, B. Istrate, T. Petreus, In vitro study regarding the cytotoxicity of some TiNbZr alloys, Ann. Rom. Soc. Cell Biol. 18 (2013) 186–191.

[9]   C.C. Gomes, L.M. Moreira, V.J.S.V. Santos, A.S. Ramos, J.P. Lyon, C.P. Soares, F.V. Santos, Assessment of the genetic risks of a metallic alloy used in medical implants, Genet. Mol. Biol. 34 (2011) 116–121. https://doi.org/10.1590/S1415-47572010005000118.

[10]   E. Eisenbarth, D. Velten, M. Müller, R. Thull, J. Breme, Biocompatibility of β-stabilizing elements of titanium alloys, Biomaterials. 25 (2004) 5705–5713. https://doi.org/10.1016/j.biomaterials.2004.01.021.

[11]   J. Nagels, M. Stokdijk, P.M. Rozing, Stress shielding and bone resorption in shoulder arthroplasty, J. Shoulder Elb. Surg. 12 (2003) 35–39. https://doi.org/10.1067/mse.2003.22.

[12]   D. Kuroda, M. Niinomi, M. Morinaga, Y. Kato, T. Yashiro, Design and mechanical properties of new β type titanium alloys for implant materials, Mater. Sci. Eng. A. 243 (1998) 244–249. https://doi.org/10.1016/s0921-5093(97)00808-3.

[13]   H.J. Rack, J.I. Qazi, Titanium alloys for biomedical applications, Mater. Sci. Eng. C. 26 (2006) 1269–1277. https://doi.org/10.1016/j.msec.2005.08.032.

[14]   A.T. Sidambe, Biocompatibility of advanced manufactured titanium implants-A review, Materials (Basel). 7 (2014) 8168–8188. https://doi.org/10.3390/ma7128168.

[15]   C. Suryanarayana, Mechanical Alloying: A Novel Technique to Synthesize Advanced Materials, Research. 2019 (2019) 1–17. https://doi.org/10.34133/2019/4219812.

[16]   M.A. Hussein, C. Suryanarayana, N. Al-Aqeeli, Fabrication of nano-grained Ti-Nb-Zr biomaterials using spark plasma sintering, Mater. Des. 87 (2015) 693–700. https://doi.org/10.1016/j.matdes.2015.08.082.

[17]   K. Jurczyk, K. Niespodziana, M.U. Jurczyk, M. Jurczyk, Synthesis and characterization of titanium-45S5 Bioglass nanocomposites, Mater. Des. 32 (2011) 2554–2560. https://doi.org/10.1016/j.matdes.2011.01.047.

[18]   K. Jurczyk, A. Miklaszewski, M.U. Jurczyk, M. Jurczyk, Development of β type Ti23Mo-45S5 bioglass nanocomposites for dental applications, Materials (Basel). 8 (2015) 8032–8046. https://doi.org/10.3390/ma8125441.

[19]   Y. Fujioka-Hirai, Y. Akagawa, S. Minagi, H. Tsuru, Y. Miyake, H. Suginaka, Adherence of Streptococcus mutans to implant materials, J. Biomed. Mater. Res. 21 (1987) 913–920. https://doi.org/10.1002/jbm.820210707.

[20]   R. Buergers, M. Rosentritt, G. Handel, Bacterial adhesion of Streptococcus mutans to provisional fixed prosthodontic material, J. Prosthet. Dent. 98 (2007) 461–469. https://doi.org/10.1016/S0022-3913(07)60146-2.

[21]   E.L. Zhang, S. Fu, R.X. Wang, H.X. Li, Y. Liu, Z.Q. Ma, G.K. Liu, C.S. Zhu, G.W. Qin, D.F. Chen, Role of Cu element in biomedical metal alloy design, Rare Met. 38 (2019) 476–494. https://doi.org/10.1007/s12598-019-01245-y.

[22]   R. Liu, K. Memarzadeh, B. Chang, Y. Zhang, Z. Ma, R.P. Allaker, L. Ren, K. Yang, Antibacterial effect of copper-bearing titanium alloy (Ti-Cu) against Streptococcus mutans and Porphyromonas gingivalis, Sci. Rep. 6 (2016). https://doi.org/10.1038/srep29985.

[23]   L.F. Espinosa-Cristóbal, G.A. Martínez-Castañón, R.E. Martínez-Martínez, J.P. Loyola-Rodríguez, N. Patiño-Marín, J.F. Reyes-Macías, F. Ruiz, Antibacterial effect of silver nanoparticles against Streptococcus mutans, Mater. Lett. 63 (2009) 2603–2606. https://doi.org/https://doi.org/10.1016/j.matlet.2009.09.018.

[24]   K. Jurczyk, M.M. Kubicka, M. Ratajczak, M.U. Jurczyk, K. Niespodziana, D.M. Nowak, M. Gajecka, M. Jurczyk, Antibacterial activity of nanostructured Ti-45S5 bioglass-Ag composite against Streptococcus mutans and Staphylococcus aureus, Trans. Nonferrous Met. Soc. China (English Ed. 26 (2016) 118–125. https://doi.org/10.1016/S1003-6326(16)64096-7.

[25]   M.M. Almoudi, A.S. Hussein, M.I. Abu Hassan, N. Mohamad Zain, A systematic review on antibacterial activity of zinc against Streptococcus mutans, Saudi Dent. J. 30 (2018) 283–291. https://doi.org/10.1016/j.sdentj.2018.06.003.

[26]   M. Kaczmarek, K. Jurczyk, J.K. Koper, A. Paszel-Jaworska, A. Romaniuk, N. Lipińska, J. Żurawski, P. Urbaniak, J. Jakubowicz, M.U. Jurczyk, In vitro biocompatibility of anodized titanium with deposited silver nanodendrites, J. Mater. Sci. 51 (2016) 5259–5270. https://doi.org/10.1007/s10853-016-9829-3.

[27]   K. Vasilev, J. Cook, H.J. Griesser, Antibacterial surfaces for biomedical devices, Expert Rev. Med. Devices. 6 (2009) 553–567. https://doi.org/10.1586/erd.09.36.

[28]   H. Chouirfa, H. Bouloussa, V. Migonney, C. Falentin-Daudré, Review of titanium surface modification techniques and coatings for antibacterial applications, Acta Biomater. 83 (2019) 37–54. https://doi.org/10.1016/j.actbio.2018.10.036.

[29]   A. Jemat, M.J. Ghazali, M. Razali, Y. Otsuka, Surface Modifications and Their Effects on Titanium Dental Implants, Biomed Res. Int. 2015 (2015) 791725. https://doi.org/10.1155/2015/791725.

[30]   L.Á. De Sena, M.C. De Andrade, A.M. Rossi, G.A. De Soares, Hydroxyapatite deposition by electrophoresis on titanium sheets with different surface finishing, J. Biomed. Mater. Res. 60 (2002) 1–7. https://doi.org/10.1002/jbm.10003.

[31]   K. Hamada, M. Kon, T. Hanawa, K. Yokoyama, Y. Miyamoto, K. Asaoka, Hydrothermal modification of titanium surface in calcium solutions, Biomaterials. 23 (2002) 2265–2272. https://doi.org/10.1016/S0142-9612(01)00361-1.

[32]   S. Ban, K. Matsuo, N. Mizutani, J. Hasegawa, Hydrothermal-Electrochemical Deposition of Calcium Phosphates on Various Metals, Dent. Mater. J. 18 (1999) 259–270. https://doi.org/10.4012/dmj.18.259.

[33]   S. Abbasi, M.R. Bilesan, F. Golestani-Fard, In vitro evaluation of the biocompatibility and bioactivity of plasma electrolyte oxidized titania/calcium phosphate nanocoatings on Ti, J. Mater. Sci. 54 (2019) 4277–4286. https://doi.org/10.1007/s10853-018-3147-x.

[34]   Q. Zhang, Y. Leng, R. Xin, A comparative study of electrochemical deposition and biomimetic deposition of calcium phosphate on porous titanium, Biomaterials. 26 (2005) 2857–2865. https://doi.org/10.1016/j.biomaterials.2004.08.016.

[35]   Y. Li, I.S. Lee, F.Z. Cui, S.H. Choi, The biocompatibility of nanostructured calcium phosphate coated on micro-arc oxidized titanium, Biomaterials. 29 (2008) 2025–2032. https://doi.org/10.1016/j.biomaterials.2008.01.009.

[36]   C. Moseke, W. Braun, A. Ewald, Electrochemically deposited Ca(OH)2 coatings as a bactericidal and osteointegrative modification of Ti implants, Adv. Eng. Mater. (2009). https://doi.org/10.1002/adem.200800154.

[37]   G.Y. Han, S.H. Park, T.C. Yoon, Antimicrobial activity of Ca(OH)2 containing pastes with enterococcus faecalis in vitro, J. Endod. 27 (2001) 328–332. https://doi.org/10.1097/00004770-200105000-00004.

[38]   K. Liu, H. Zhang, M. Lu, L. Liu, Y. Yan, Z. Chu, Y. Ge, T. Wang, C. Tang, Enhanced bioactive and osteogenic activities of titanium by modification with phytic acid and calcium hydroxide, Appl. Surf. Sci. 478 (2019) 162–175. https://doi.org/10.1016/j.apsusc.2019.01.219.

2. Cel i zakres pracy

Celem pracy było wytworzenie stopów o strukturze β oraz pseudo β w układzie trójskładnikowym Ti-Zr-Nb metodą mechanicznej syntezy, a następnie ich modyfikacja poprzez tworzenie układów kompozytowych oraz elektrochemiczną obróbkę powierzchni. Podjęte działania miały na celu poprawę biozgodności poprzez eliminację dodatków o działaniu toksycznym w tym neurotoksycznym jak aluminium oraz wanad. Tworzenie tego typu stopów ma również zapewnić lepsze dopasowanie właściwości użytkowych materiałów w zastosowaniach medycznych. Dalsza modyfikacja poprzez tworzenie układów kompozytowych miała zredukować moduły Younga stopów, poprawić ich odporność korozyjną, zwiększyć biokompatybilność oraz prowadzić do uzyskania aktywności antybakteryjnej, badanej dla znajdującego się w jamie ustnej szczepu bakterii *S. mutans*. Celem polepszenia właściwości biologicznych oraz odporności korozyjnej badanych układów poddano je obróbce powierzchniowej.

Do szczegółowych zadań realizowanych w ramach załączonych do rozprawy publikacji należały:

a) wytworzenie stopów o różnej zawartości niobu (od 16 do 34% at.) oraz cyrkonu (od 14 do 30% at.) metodą mechanicznej syntezy wykorzystując proszki wysokiej czystości Ti oraz Nb, a także opiłki Zr, przy czasie mielenia 10 h. Wytworzone proszki były następnie prasowane jednoosiowo na zimno pod ciśnieniem 600 MPa i spiekane w temperaturach od 600 do 1000°C przez 30 min. Charakterystyka wytworzonych materiałów obejmowała: analizę strukturalną stopów w trakcie mielenia oraz po konsolidacji z wykorzystaniem dyfraktometru rentgenowskiego (do tego celu wykorzystano również metodę Williamsona-Halla oraz analizę Rietvelda), analizę zwilżalności, pomiary potencjodynamiczne odporności korozyjnej oraz badania mechaniczne, obejmujące pomiary mikrotwardości i modułu E metodą nanoindentacji. Wykorzystując metodę spekroskopii dyspersji energii (ang. energy dispersive spectrometry - EDS) określono skład chemiczny finalnych materiałów. Z kolei analizę mikrostruktury wybranego stopu jednofazowego β oraz dwufazowego α+β wykonano metodą dyfrakcji elektronów wstecznie rozproszonych (ang. electron backscatter diffraction – EBSD),

b) wytworzenie wybranego dwufazowego stopu α+β Ti14Zr16Nb (% at.) oraz jednofazowego stopu β Ti23Zr25Nb (% at.) mechaniczną syntezą oraz poprzez prasowanie na zimno oraz spiekanie w temperaturach od 600 do 1000°C, a także poprzez indukcyjne prasowanie na gorąco w temperaturze 600°C oraz pod ciśnieniem 71 MPa przez 10 min. Charakterystyka wytworzonych materiałów obejmowała: analizę strukturalną stopów w trakcie mielenia oraz

po konsolidacji z wykorzystaniem dyfraktometru rentgenowskiego (tak samo jak w przypadku poprzednich układów wykorzystano również metodę Williamsona-Halla oraz analizę Rietvelda), badania mechaniczne, obejmujące pomiary nanoindentacji oraz mikrotwardości wybranych stopów, analizę porowatości stopów wytworzonych tradycyjnie oraz prasowanych na gorąco z wykorzystaniem histogramów obrazów z mikroskopu optycznego. Badane materiały po trawieniu w odczynniku Krolla były ponadto obserwowane z wykorzystaniem skaningowego mikroskopu elektronowego (ang. scanning electron microscope – SEM) celem odwzorowania i obserwacji mikrostruktury materiałów. SEM umożliwił również obserwację proszków przed i po mieleniu. Składy chemiczne finalnych materiałów zostały określone z wykorzystaniem metody EDS,

c) wytworzenie kompozytów na bazie stopu Ti23Zr25Nb (% at.), z dodatkiem od 3 do 9% wag. dodatku Bioszkła 45S5 wraz z 1% wag. dodatkiem bakteriobójczym w postaci srebra, miedzi lub cynku metodą mechanicznej syntezy w czasie 16 h oraz metodą prasowania na zimno pod ciśnieniem 600 MPa oraz spiekanych w temperaturze 800°C. Badania, podobnie jak w przypadku materiałów niemodyfikowanych obejmowały analizę strukturalną, obserwację proszków, badania mechaniczne (pomiar mikrotwardości oraz nanoindentacji odniesiony do układów Ti-Zr-Nb wytwarzanych metodą topienia łukowego oraz pianki na bazie stopu Ti23Zr25Nb), badania zwilżalności oraz odporności korozyjnej, a także analizę porowatości. Dodatkowo w przypadku tych materiałów wykonano mapy rozkładu poszczególnych pierwiastków, wchodzących w skład kompozytu z wykorzystaniem techniki EDS, ocenę aktywności antybakteryjnej w stosunku do bakterii *S. mutans* oraz testy MTS (Non-Radioactive Cell Proliferation Assay) celem określenia biokompatybilności kompozytów względem niemodyfikowanego stopu Ti23Zr25Nb (% at.) z wykorzystaniem osteoblastów oraz fibroblastów,

d) modyfikacja powierzchni poprzez trawienie elektrochemiczne w wodnym roztworze 1 M kwasu fosforowego (V) oraz 2% kwasu fluorowodorowego stopu Ti23Zr25Nb (% at.) pod napięciem +10 V względem potencjału stacjonarnego przez 60 min celem rozwinięcia powierzchni, a następnie osadzanie elektrochemiczne mieszaniny wodorotlenku wapnia z hydroksyapatytem w wodnym roztworze 0.042 M azotanu wapnia, 0.025 M wodorofosforanu amonu oraz 0.1 M kwasu chlorowodorowego pod napięciem -10 V przez 60 min. Badane materiały po modyfikacji powierzchniowej zostały poddane analizie strukturalnej z użyciem dyfraktometru rentgenowskiego, ocenie odporności korozyjnej, pomiarom zwilżalności. Obserwację morfologii warstw wykonano z użyciem mikroskopu SEM, analizę rozkładu wapnia oraz fosforu metodą EDS. Przeprowadzono również badania

chropowatości próbek po każdym etapie wytwarzania, a także testy biologiczne MTS mające ocenić biozgodność badanych układów.

3. Wyniki badań

3.1. Analiza układów trójskładnikowych Ti-Nb-Zr

Stopy Ti-Nb-Zr, zawierające od 16 do 34% at. niobu oraz od 14 do 30% at. cyrkonu zostały wytworzone metodami mechanicznej syntezy i metalurgii proszków. Konsolidację przeprowadzono poprzez prasowanie na zimno oraz spiekanie w atmosferze ochronnej argonu wysokiej czystości w temperaturach 600, 750, 800, 850 oraz 1000°C przez 30 min z chłodzeniem w wodzie [1,2].

Analiza strukturalna wybranych stopów Ti14Zr16Nb (% at.) oraz Ti23Zr25Nb (% at.) w czasie od 15 min do 10 h mechanicznej syntezy wykazała występowanie w trakcie procesu przemiany fazowej Ti(α)$\rightarrow$Ti(β) w obu materiałach (**Rysunek 1** oraz Rysunek 2 [1]). Mielenie mikrokrystalicznych proszków wyjściowych tytanu, niobu oraz cyrkonu po 10 h prowadziło do powstawania jednofazowej struktury Ti(β) lub dwufazowej struktury Ti(α)+Ti(β) w zależności od zawartości dodatków stopowych (Rysunek 1 [2]). Metoda Williamsona-Halla, potwierdziła wysoki stopień rozdrobnienia materiałów, o czym świadczył wyznaczony rozmiar krystalitów w przedziale od 14 do 28 nm, przy jednoczesnej wielkości mikro odkształceń na poziomie od 9 do 23‰ (Rysunek 2 [2]).
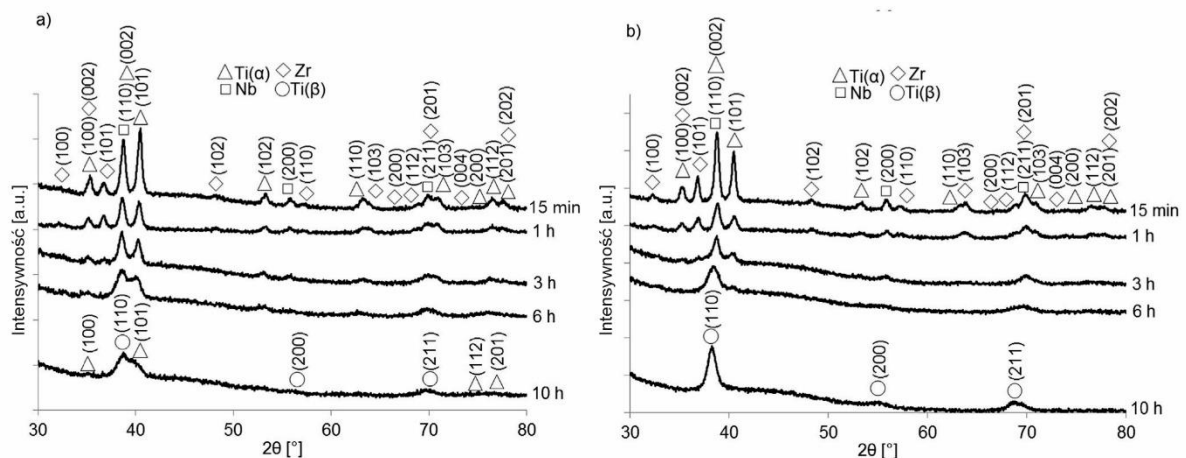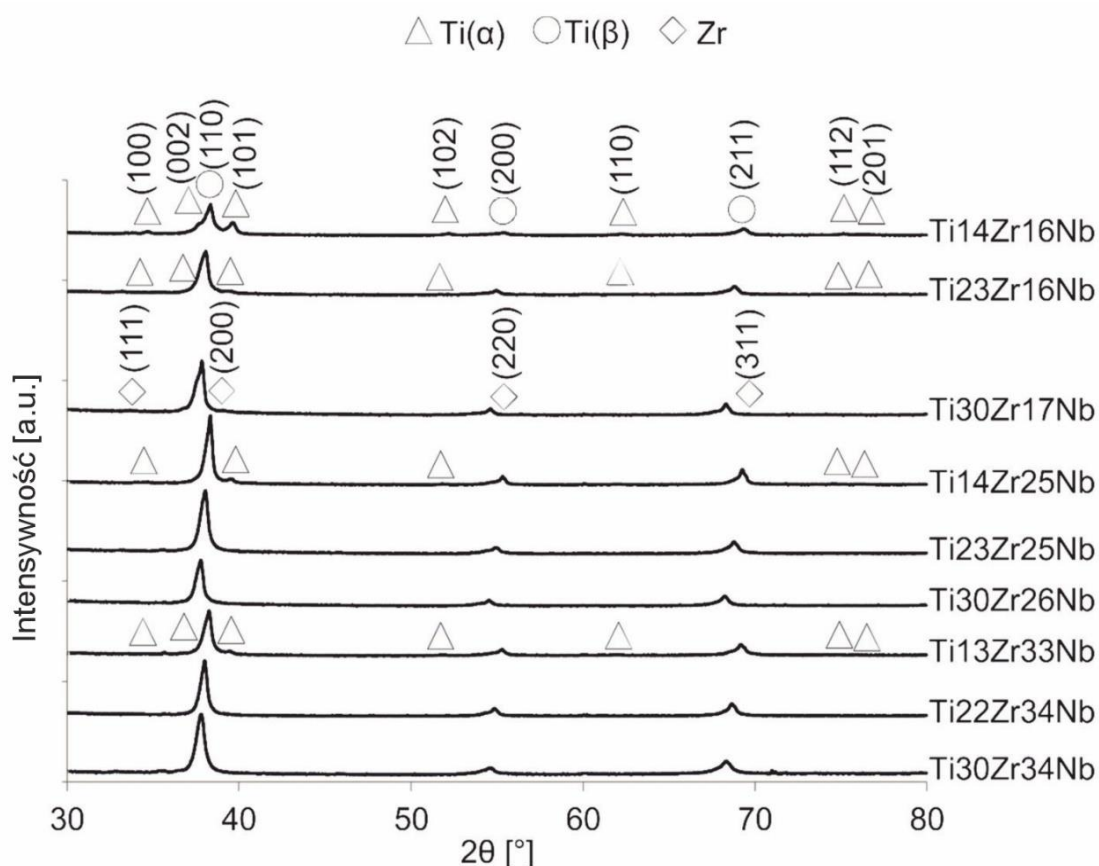

Rysunek 1. Dyfraktogramy rentgenowskie stopów Ti14Zr16Nb (a) oraz Ti23Zr25Nb (b) w czasie mielenia [1].

Temperatura spiekania oraz skład wytworzonych stopów wywierały istotny wpływ na strukturę krystalograficzną stopów. Analiza dyfraktogramów rentgenowskich materiałów po spiekaniu została przeprowadzona metodą Rietvelda, co umożliwiło określenie udziałów fazowych oraz parametrów sieci krystalograficznych badanych materiałów (Tabela 2 [2]). Struktury badanych stopów po przeprowadzonym procesie konsolidacji można było rozdzielić na dwie grupy. W pierwszej z nich poza fazą Ti(β) występowały fazy Zr (ref. code

01-088-2329), NbZr (ref. code 01-071-9970) oraz Nb0.81Zr0.19 (ref. code 00-049-1455). W tych stopach niezależnie od parametrów procesu spiekania w strukturze nie występowała faza Ti(α). Należały do nich następujące materiały: Ti30Zr17Nb, Ti23Zr25Nb, Ti30Zr26Nb, Ti22Zr34Nb oraz Ti30Zr34Nb (% at.). Do drugiej grupy stopów, w których poza fazami Zr oraz Nb0.81Zr0.19 występowała faza Ti(α) należały stopy Ti14Zr16Nb, Ti23Zr16Nb, Ti14Zr25Nb oraz Ti13Zr33Nb (% at.). Uzyskanie struktury jednofazowej β w przypadku sześciu stopów, tj. Ti30Zr17Nb, Ti23Zr25Nb, Ti30Zr26Nb, Ti22Zr34Nb oraz Ti30Zr34Nb, było możliwe po spiekaniu w temperaturze 600°C, czyli znacznie poniżej temperatury przemiany fazowej Ti(α)→Ti(β) czystego tytanu, która wynosi 882°C. Ponadto w przypadku wszystkich stopów, z wyjątkiem tych zawierających 13-14% at. Zr w wyższych temperaturach spiekania (zawsze powyżej 750°C) występuje czysty Zr o strukturze regularnej ściennie centrowanej. Dodatek niobu wykazywał znacznie większy wpływ na stabilizację fazy Ti(β), a cyrkonu na wzrost jej parametru sieci krystalicznej. Najmniejsza wartość ok. 3.3218 Å charakteryzowała stop Ti14Zr16Nb spiekany w 750°C, natomiast najwyższa ok. 3.3770 Å stop Ti30Zr26Nb spiekany w 1000°C. Dyfraktogramy stopów spiekanych w temperaturze 750°C zostały przedstawione na **Rysunku 2** oraz Rysunku 4 [2].


Rysunek 2. Dyfraktogramy rentgenowskie stopów trójskładnikowych Ti-Zr-Nb o różnym składzie chemicznym w procentach atomowych spiekanych w temperaturze 750°C [2].

Właściwości stopów Ti-Zr-Nb mogą zostać znacząco poprawione poprzez zastosowanie metody indukcyjnego prasowania na gorąco. Umożliwiła ona znaczące zmniejszenie porowatości wytworzonego materiału w wyniku jednoczesnego oddziaływania wysokiej temperatury oraz ciśnienia prasowania. Jej redukcja w przypadku stopu Ti23Zr25Nb (% at.) była możliwa z ok. 20-28% dla próbek prasowanych na zimno do ok. 2% (Tabela 2 [1]). Ponadto struktura krystaliczna tego stopu po prasowaniu na gorąco w temperaturze 600°C była taka sama jak w przypadku próbki prasowanej na zimno i spiekanej w wyższej temperaturze, tj. 750-800°C. W przypadku stopu Ti14Zr16Nb (% at.) przy jednoczesnym oddziaływaniu ciśnienia (71 MPa) i temperatury (600°C) możliwe było wytworzenie struktury dwufazowej α+β o wyraźnie większym udziale fazy Ti(β) niż przy dwustopniowej konsolidacji proszków (Tabela 1 [1]). **Rysunek 3** oraz Rysunek 6 [1] przedstawia mikrostrukturę nietrawionego stopu Ti23Zr25 (% at.), oraz różnicę w rozkładzie porowatości w przypadku stopu prasowanego na zimno i spiekanego swobodnie w 800°C oraz prasowanego na gorąco w 600°C.
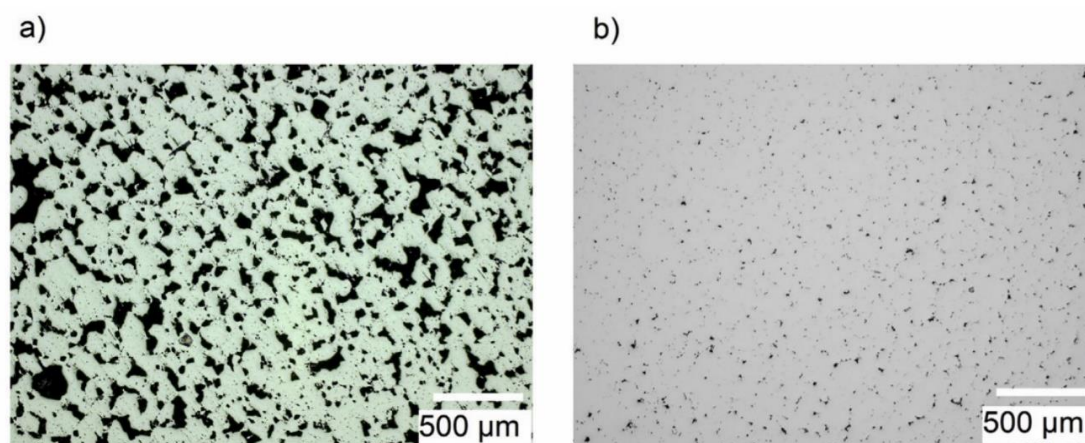
Rysunek 3. Powierzchnia nietrawionego stopu Ti23Zr25Nb (% at.) prasowanego na zimno i spiekanego swobodnie w 800°C (a) oraz prasowanego na gorąco w 600°C (b) [1].

Wytworzone stopy posiadały ultradrobnoziarnistą strukturą po spiekaniu, co zostało potwierdzone metodą dyfrakcji elektronów wstecznie rozproszonych (ang. electron backscatter diffraction – EBSD) wskazującą na średnią wielkość ziarna stopu Ti23Zr25Nb (% at.) spiekanego w temperaturze 750°C równą 1.2-1.7 μm. Badanie to wskazało również na różnice w rozkładzie dezorientacji ziarnowych Ti(β) w stopie dwufazowym α+β Ti14Zr16Nb (% at.) oraz jednofazowym β Ti23Zr25Nb (% at.). W przypadku materiału zawierającego większą zawartość dodatków, wykazano znacznie mniejszy udział granic niskokątowych, co było spowodowane niepełnym zanikiem tego typu granic przez granice wysokokątowe podczas rekrystalizacji materiału w wyniku spiekania (**Rysunek 4** oraz Rysunek 6, 7 [2]).
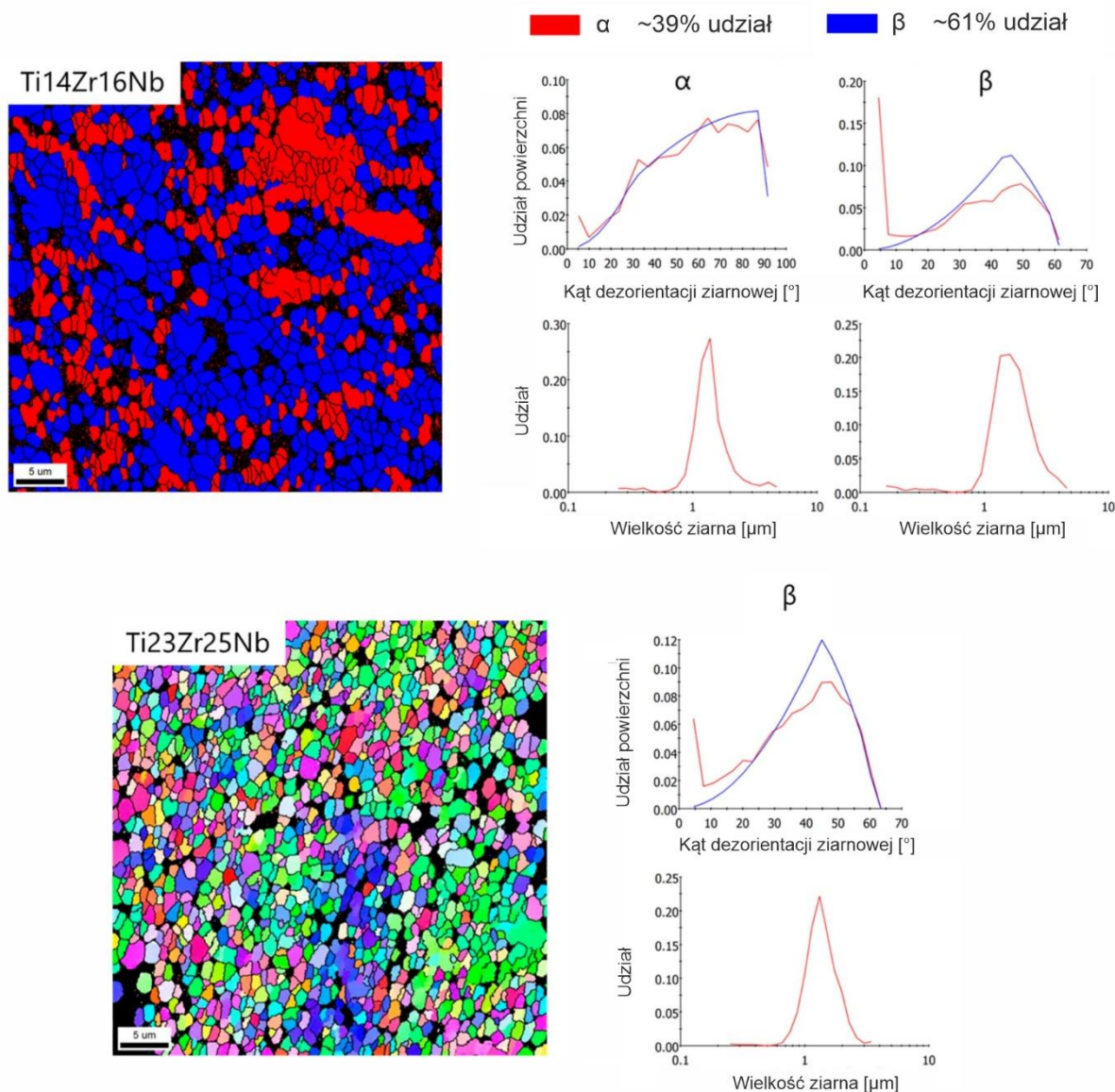
Rysunek 4. Mapki EBSD oraz histogramy kątów dezorientacji ziarnowej oraz wielkości ziarna dla stopów Ti14Zr16Nb (% at.) oraz Ti23Zr25Nb (% at.) spiekanych w temperaturze 750°C [2].

Moduł Younga wyznaczony metodą nanoindentacji dla wybranych stopów o strukturze β oraz pseudo β wynosił od ok. 68 do ok. 78 GPa, co było wartością mniejszą niż w przypadku dwufazowego stopu α+β – ok. 85 GPa (Rysunek 9 [2]). Ponadto, w przypadku stopów Ti14Zr16Nb oraz Ti23Zr25Nb (% at.) prasowanych na zimno i spiekanych swobodnie w 600°C był mniejszy niż w przypadku stopów prasowanych na gorąco w tej samej temperaturze (97-100 GPa), co wynikało z wyraźnie większej porowatości tych materiałów, oraz stopu Ti18Zr24Nb (% at.) wytworzonego metodą topienia łukowego (ok. 92 GPa) - Rysunek 5 [3]. Wszystkie uzyskane wyniki dla wytworzonych stopów były korzystniejsze względem czystego technicznie tytanu Grade 2 – 141 GPa (Rysunek 9 [1]). Twardość wyznaczona dla wszystkich stopów była bardzo zbliżona. Dla wybranych stopów β oraz pseudo β, jak również stopu jednofazowego α Ti14Zr16Nb (% at.), spiekanych

w temperaturze 750°C wartości mieściły się w zakresie 380-410 HV0.3 (Tabela 3 [2]). Pomiary kątów zwilżalności wybranych materiałów wykazały ich hydrofilowość, co wiąże się z kątami zwilżalności mniejszymi od 90° w przypadku obu stosowanych cieczy pomiarowych: diiodometanu oraz gliceryny. Nie powinno to mieć negatywnego wpływu na narastanie komórek kostnych jak w przypadku powierzchni hydrofobowych. Swobodna energia powierzchniowa materiałów wyznaczona metodą OWRK (Owens, Wendt, Rabel oraz Kaelble) mieściła się w zakresie od 29 do 40 mN/m (Tabela 3 [2]). Ponadto, wytworzone materiały charakteryzowała dobra odporność korozyjna w roztworze Ringera. Pomimo wyższych prądów korozyjnych oraz niższego potencjału korozyjnego od czystego technicznie tytanu, posiadały zbliżony przebieg krzywych polaryzacji z wyraźnym zakresem pasywnym (Rysunek 8 [2]).
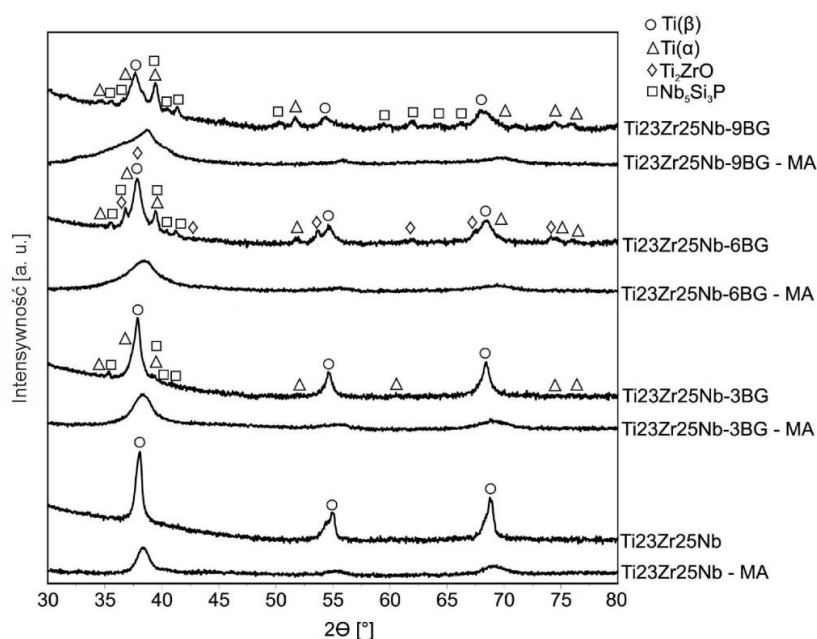
3.2. Kompozyty na bazie stopu Ti23Zr25Nb (% at.)

Dalsza poprawa właściwości stopów była realizowana w zakresie wytwarzania układów kompozytowych, zawierających od 3 do 9% wag. Bioszkła 45S5 (Ti23Zr25Nb-3BG, Ti23Zr25N-6BG oraz Ti23Zr25Nb-9BG) wraz z zawartością 1% wag. dodatków bakteriobójczych: srebra, miedzi lub cynku (Ti23Zr25Nb-9BG-Ag, Ti23Zr25Nb-9BG-Cu oraz Ti23Zr25Nb-9BG-Zn). Konsolidację proszków przeprowadzono w atmosferze ochronnej argonu (podobnie jak w przypadku stopów) w temperaturze 800°C przez 30 min z chłodzeniem w wodzie [4].

Bioszkło 45S5 hamowało powstawanie fazy Ti(β) w trakcie mechanicznej syntezy. Dla 3% wag. dodatku uzyskano materiały o strukturze jednofazowej. Przy dodatku rzędu 6% wag. po 16 h procesu MA w strukturze pojawiają się zawartości innych faz. Dalsze zwiększanie zawartości BG do 9% wag. w materiale prowadzi do uzyskania struktury wielofazowej z wyraźnie występującymi refleksami, pochodzącymi od proszków wyjściowych, czyli Ti(α), Nb/Ti(β) oraz Zr (Rysunek 2 [4]). Wykazano również istotny wpływ bioceramiki na rozdrobnienie struktury proszku podczas mielenia. Wielkość krystalitów, wyznaczona metodą Williamsona-Halla, zmalała od ok 29 nm do ok. 3 nm w kompozycie Ti23Zr25Nb-9BG. Dodatkowe zmniejszenie wielkości do ok. 2.4 nm zostało spowodowane dodatkiem srebra (Rysunek 3 [4]). Bioszkło 45S5 wpłynęło również na zmniejszenie zawartości fazy Ti(β) po procesie spiekania, a jej udział wynosił ok. 96% w kompozycie Ti23Zr25Nb-3BG. Łączny udział roztworów stałych na bazie tytanu (α, β) był najwyższy wśród kompozytów oraz wynosił ponad 98%. Świadczy to o rozpuszczeniu się pierwiastków, wchodzących w skład

BG, głownie w tych fazach, prowadząc jednocześnie do zwiększenia rozmiaru komórki elementarnej Ti(β). Zawartość tej fazy znacząco malała wraz ze zwiększaniem zawartości bioszkła, aż do 65% w przypadku Ti23Zr25Nb-9BG. Dalsza redukcja zawartości tej fazy nastąpiła w przypadku kompozytów domieszkowanych miedzią oraz cynkiem do odpowiednio ok. 59% oraz 55%, co jest związane z wydzieleniem się większej ilości stabilizującego fazę Ti(β) niobu w postaci fazy Nb_5Si_3P. Wzrost stężenia BG wpłynął ponadto na parametr sieci krystalicznej, który zwiększył się z 3.3524 Å dla niemodyfikowanego stopu Ti23Zr25Nb (% at.) do 3.3720 Å dla kompozytu, zawierającego 9% dodatku. Zmniejszenie się parametru komórki elementarnej w kompozycie Ti23Zr25Nb-6BG do 3.3577 Å spowodowane jest wydzieleniem się fazy Ti_2ZrO, ograniczającej ilość cyrkonu rozpuszczonego w roztworze stałym na bazie Ti(β). Podobne zjawisko zaobserwowano w przypadku kompozytów z dodatkiem Ag i Zn, w obu przypadkach prowadząc do redukcji parametru komórki elementarnej poniżej 3.3600 Å (Tabela 2 [4]). Homogeniczność rozkładu dodatków, wchodzących w skład badanych materiałów została potwierdzona z wykorzystaniem spektroskopii dyspersji energii (ang. energy dispersive spectroscopy - EDS) oraz przedstawione w postaci mapek rozkładu poszczególnych pierwiastków (Rysunek 7 oraz Rysunek 8 [4]). Dyfraktogramy kompozytów, zawierających od 3 do 9% wag. BG oraz spiekanych swobodnie w 800°C, zostały przedstawione na **Rysunku 5** oraz Rysunku 5 [4]. Dyfraktogramy zostały zestawione z proszkami po mechanicznej syntezie oraz niemodyfikowanym stopem Ti23Zr25Nb (% at.).

Rysunek 5. Dyfraktogramy rentgenowskie kompozytów na bazie stopu Ti23Zr25Nb (% at.), zawierających od 3 do 9% wag. Bioszkła 45S5 spiekanych swobodnie w 800°C w porównaniu do niemodyfikowanego stopu Ti23Zr25Nb (% at.) oraz proszków po mechanicznej syntezie (MA) [4].
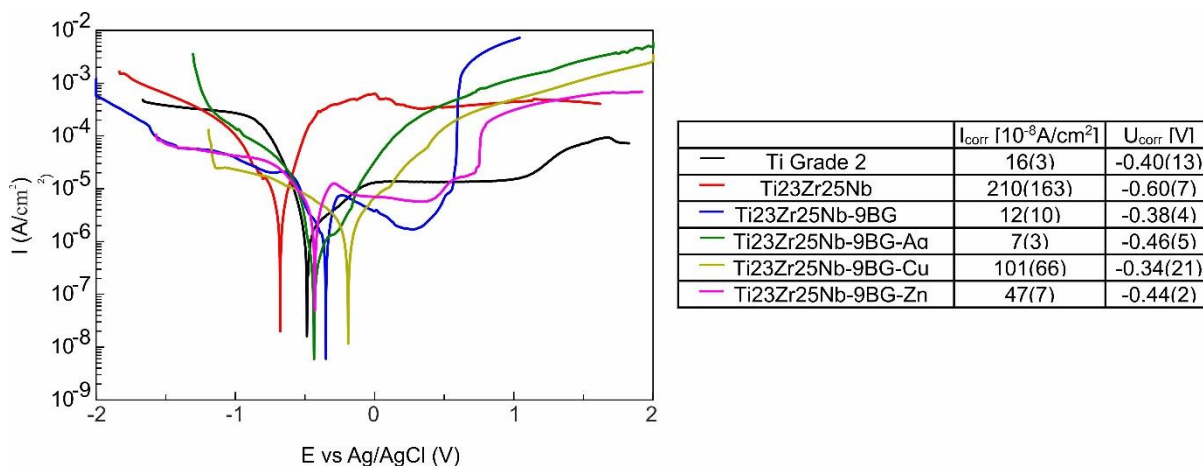
Moduł Younga dla kompozytów, zawierających Bioszkło 45S5 wynosił od ok. 43 GPa do ok. 72 GPa (Rysunek 10 [4]) przy porowatości od ok. 15 do ok. 23% (Tabela 3 [4]). Najmniejsza wartość (43 GPa) charakteryzuje kompozyt Ti23Zr25Nb-9BG, który odznacza się jednocześnie najniższą twardością (ok. 218 HV0.3 – Tabela 4 [4]) oraz największą porowatością (23%). Modyfikacja w ten sposób stopu Ti23Zr25Nb okazała się efektywniejsza od wytwarzania pianek o porowatości ok. 70% z wykorzystaniem wodorowęglanu amonu, w przypadku których moduł Younga został zredukowany do ok. 56 GPa. **Rysunek 6** oraz Rysunek 5 [3] przedstawia krzywe obciążenie-głębokość dla stopu Ti23Zr25Nb po różnych sposobach konsolidacji proszków oraz modyfikacji w odniesieniu do czystego technicznie tytanu Grade 2 oraz stopu Ti18Zr24Nb (% at.) topionego łukowo. Wartość ta jest wyraźnie bliższa tej charakteryzującej kość, prowadząc do lepszego dopasowania właściwości mechanicznych.
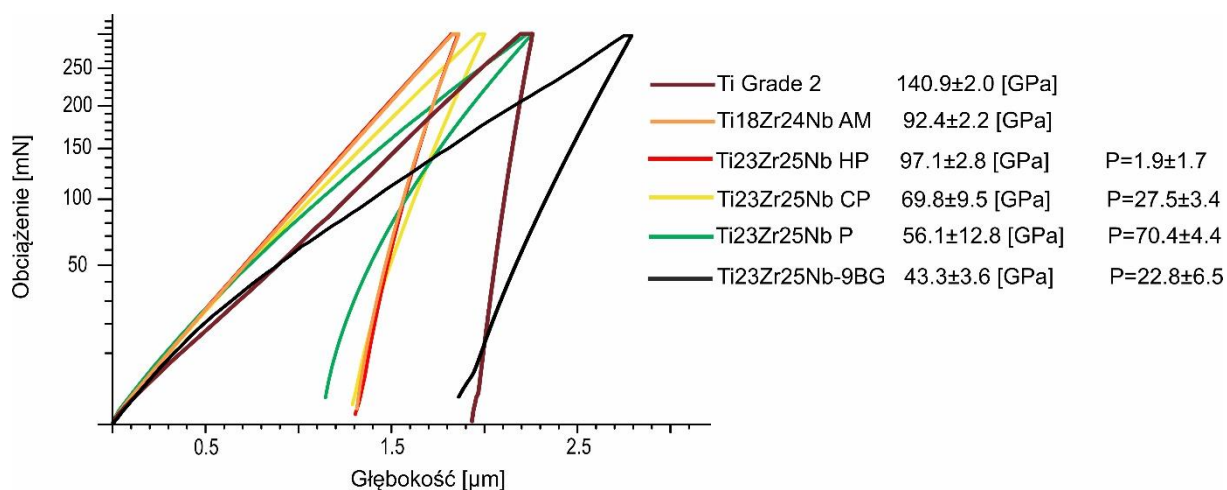
Rysunek 6. Krzywe obciążenie-głębokość pomiarów nanoindentacji stopu Ti23Zr25Nb (% at.) prasowanego na gorąco w 600°C (HP), prasowanego na zimno oraz spiekanego swobodnie w 800°C (CP+S), spienionego z wykorzystaniem wodorowęglanu amonu (P) oraz modyfikowanego 9% wag. Bioszkłem 45S5 (9BG). Wyniki zostały odniesione do czystego technicznie tytanu Grade 2 oraz stopu Ti18Zr24Nb (% at.) wytworzonego metodą topienia łukowego (AM). Wyznaczono również porowatości badanych materiałów (P) metodą planimetryczną [3].

Podobnie jak w przypadku stopów Ti-Zr-Nb, tak również w przypadku kompozytów, zawierających bioszkło oraz modyfikowanych dodatkiem bakteriobójczym srebra, miedzi lub cynku kąty zwilżalności były mniejsze niż 90°. Potwierdziło to hydrofilowość badanych materiałów. Wyznaczona swobodna energia powierzchniowa wynosiła od ok. 35 mN/m (Ti23Zr25Nb-6BG oraz Ti23Zr25Nb-9BG-Zn) do ok 42 mN/m (Ti23Zr25Nb-9BG-Ag). Wartości te były bardzo zbliżone do tych, charakteryzujących stopy Ti-Zr-Nb bez dodatków. Dodatek bioszkła wpływa na znaczną poprawę odporności korozyjnej stopu Ti23Zr25Nb (% at.), prowadząc w przypadku kompozytu Ti23Zr25Nb-9BG do obniżenia prądu korozyjnego (ok. $12*10^{-8}$A/cm^2) oraz potencjału korozyjnego (ok. -0.38 V) do wartości

bliskich czystemu technicznie tytanowi Grade 2 (odpowiednio ok. $16*10^{-8}$A/cm^2 oraz ok. -0.40 V). Dalsze obniżenie prądów korozyjnych (ok. $7*10^{-8}$A/cm^2) przy zbliżonym potencjale korozyjnym (ok. -0.46 V) było możliwe poprzez modyfikację kompozytu Ti23Zr25Nb-9BG srebrem. Mogło to być spowodowane zwiększeniem stabilności warstwy pasywnej poprzez dodatek metalu szlachetnego (**Rysunek 7** oraz Rysunek 11, 12 [4]).

|	I$_{corr}$ [10^{-8}A/cm^2]	U$_{corr}$ [V]
Ti Grade 2	16(3)	-0.40(13)
Ti23Zr25Nb	210(163)	-0.60(7)
Ti23Zr25Nb-9BG	12(10)	-0.38(4)
Ti23Zr25Nb-9BG-Ag	7(3)	-0.46(5)
Ti23Zr25Nb-9BG-Cu	101(66)	-0.34(21)
Ti23Zr25Nb-9BG-Zn	47(7)	-0.44(2)

Rysunek 7. Krzywe polaryzacji kompozytów zawierających 9% Bioszkła 45S5 oraz srebro, miedź lub cynk. Wyniki zostały odniesione do czystego technicznie tytanu Grade 2 oraz stopu Ti23Zr25Nb (% at.) spiekanego swobodnie w 800°C [4].

3.3. Modyfikacja powierzchni stopu Ti23Zr25Nb (% at.)

Stop Ti23Zr25Nb (% at.) był modyfikowany powierzchniowo. Obróbka składała się z dwóch procesów. Pierwszy z nich polegał na trawieniu elektrochemicznym w wodnym roztworze 1 M kwasu fosforowego (V) oraz 2% kwasu fluorowodorowego pod napięciem +10 V względem potencjału obwodu otwartego (OCP) przez 60 min. Następnie przeprowadzono osadzanie elektrochemiczne w wodnym roztworze 0.042 M azotanu wapnia, 0.025 M wodorofosforanu amonu oraz 0.1 M kwasu chlorowodorowego pod napięciem –10 V względem OCP przez 60 min [3]. Zaproponowana modyfikacja powierzchni prowadzi do powstania powłoki zawierającej wodorotlenek wapnia (Ca(OH)$_2$) oraz hydroksyapatyt (Ca$_5$(PO$_4$)$_3$OH) – Rysunek 1 [3].

Trawienie elektrochemiczne umożliwiło rozwinięcie powierzchni, prowadząc do powstania wżerów oraz porów na powierzchni materiału, co w dalszej kolejności przyczyniło się do łatwiejszego osadzania jonów wapnia oraz fosforu – Rysunek 2 [3]. Obecność obu jonów po przeprowadzonym drugim etapie obróbki powierzchniowej została potwierdzona z wykorzystaniem spekroskopii dyspersji energii (ang. energy dispersive spectrometry - EDS), a rozkład obu pierwiastków został przedstawiony w postaci mapek.

Potwierdziły one również większy udział wapnia w stosunku do fosforu na powierzchni stopu (Rysunek 3 [3]). Dyfrakcja rentgenowska umożliwiła określenie struktury krystalicznej wytworzonej powłoki, która była mieszaniną wodorotlenku wapnia oraz hydroksyapatytu (**Rysunek 8** oraz Rysunek 1 [3]).
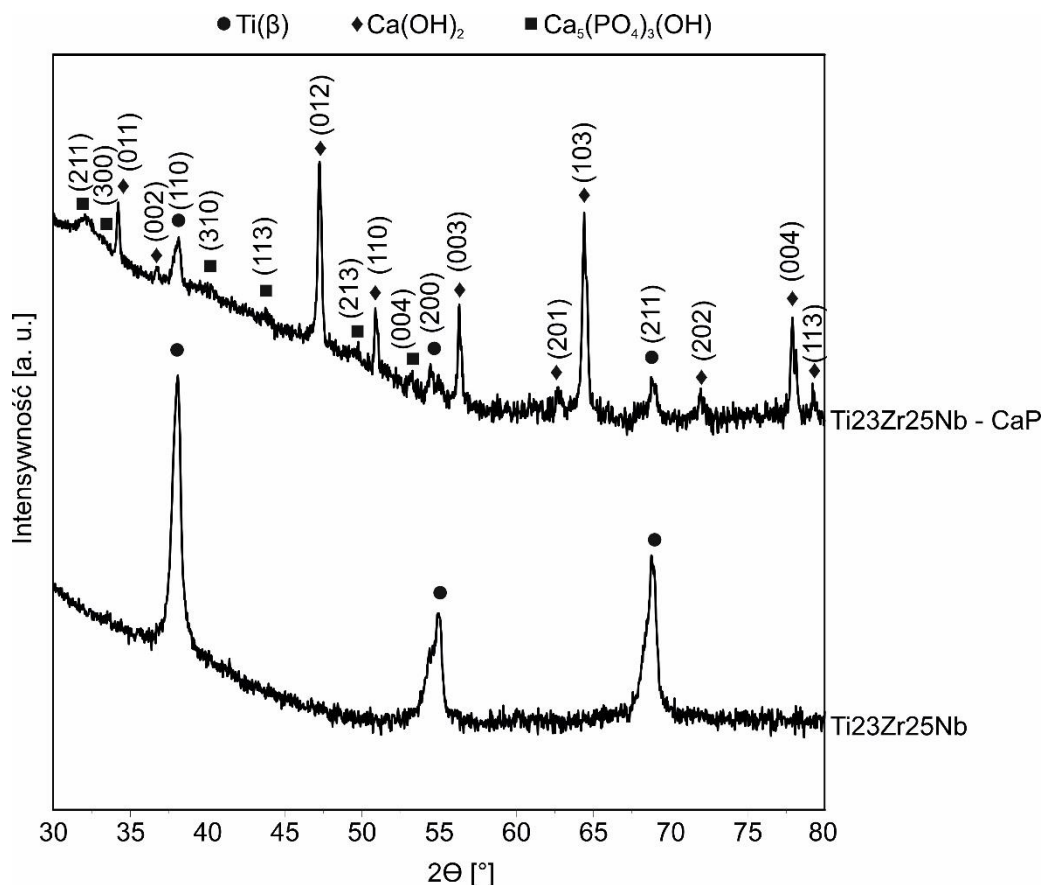
Rysunek 8. Dyfraktogram powłoki na stopie Ti23Zr25Nb (% at.) po osadzaniu elektrochemicznym w roztworze 0.042 M Ca(NO₃)₂ + 0.025 M (NH₄)₂HPO₄ + 0.1 M HCl pod napięciem -10 V względem OCP przez 60 min (CaP), odniesiony do niemodyfikowanego stopu Ti23Zr25Nb (% at.) [3].

Otrzymano powłokę o grubości ok. 50 µm, co zostało zmierzone z wykorzystaniem obrazów przekroju poprzecznego próbki po procesie osadzania (**Rysunek 9** oraz Rysunek 4 [3]).
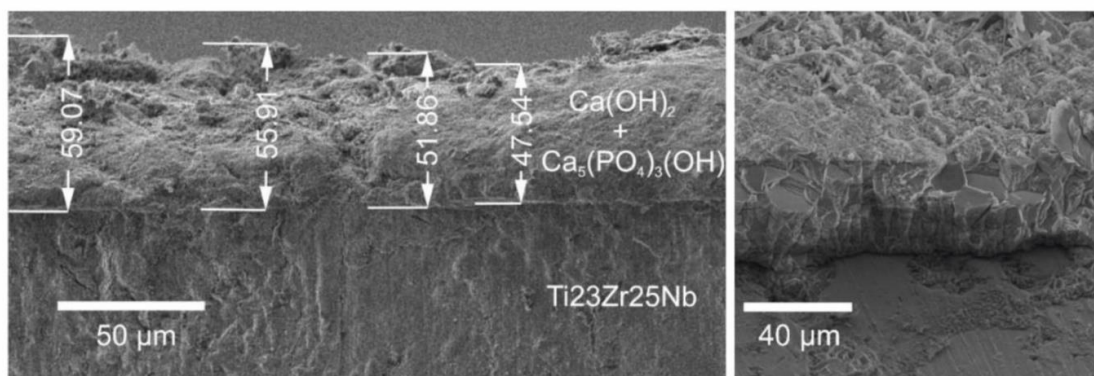
Rysunek 9. Powłoka na stopie Ti23Zr25Nb (% at.) po osadzaniu elektrochemicznym w roztworze 0.042 M Ca(NO₃)₂ + 0.025 M (NH₄)₂HPO₄ + 0.1 M HCl pod napięciem -10 V względem OCP przez 60 min w przekroju poprzecznym po lewej (po lewej) oraz widoku pochylonym pod kątem 51° (po prawej) [3].

Analiza profilów badanych próbek potwierdziła wyraźne rozwinięcie powierzchni po trawieniu (Rysunek 6 [3]). Wartość parametrów Ra, Rz oraz Rt (Tabela 1 [3]). wzrosła odpowiednio do ok. 6, 39 oraz 30 μm z 1, 13 oraz 8 μm dla próbki niemodyfikowanej. Późniejsze osadzanie prowadziło do spadku chropowatości (Ra ≈ 3 μm, Rz ≈ 27 μm oraz Rt ≈ 19 μm). Modyfikacja powierzchni doprowadziła do poprawy odporności korozyjnej stopu Ti23Zr25Nb (% at.) – Rysunek 7 [3]. Była ona jednak mniej efektywna niż w przypadku stopów modyfikowanych bioszkłem, to jest kompozytów Ti23Zr25Nb-9BG oraz Ti23Zr25Nb-9BG-Ag. W ich przypadku doszło do zmniejszenia wartości prądów korozyjnych do ok. $10*10^{-8}$ A/cm^2, w porównaniu do ok. $10*10^{-7}$ A/cm^2 dla stopów modyfikowanych powierzchniowo. Obróbka powierzchniowa umożliwiła jednakże znaczne poprawienie właściwości hydrofilowych, o czym świadczy wyraźne zmniejszenie kątów zwiłżalności dla gliceryny do ok. 33° oraz dla dioodometanu do ok. 12°. Jednocześnie swobodna energia powierzchniowa wzrosła z ok. 35 do 58 mN/m (Tabela 2 [3]).

3.4. Ocena aktywności bakteriobójczej oraz właściwości biologicznych (testy MTS)

W ramach badań materiałów przeprowadzono ocenę aktywności bakteriobójczej stopu Ti23Zr25Nb (% at.), kompozytów Ti23Zr25Nb-9BG oraz Ti23Zr25-9BG-Ag (Cu, Zn) względem bakterii *S. mutans* ATCC 2517 [4]. Materiały te wraz ze stopem modyfikowanym powierzchniowo poprzez wytworzenie powłoki Ca(OH)$_2$ oraz hydroksyapatytu, zostały również poddane testom biokompatybilności *in vitro* celem zbadania intensywności wzrostu komórek kostnych na powierzchniach wytworzonych preparatów. Do tego celu wykorzystano dwie linie komórek macierzystych: normalne ludzkie osteoblasty (NHost, CC-2538) oraz ludzkie fibroblasty więzadeł ozębnej (HPdLF, CC-7049) [3], hodowanych na badanych materiałach przez 24, 72 oraz 120 h.

Wszystkie kompozyty, zawierające dodatki bakteriobójcze, to jest srebro, miedź oraz cynk, wykazały obniżoną adhezję bakterii, spowodowaną ograniczeniem tworzenia się biofilmu na tych kompozytach. Współczynnik redukcji, odniesiony do liczby jednostek, tworzących kolonie bakteryjne na czystym technicznie tytanie, w przypadku tych materiałów jest wyższy niż 90% (**Tabela 1** oraz Tabela 5 [4]). Wysoka aktywność bakteriobójcza względem stopu Ti23Zr25Nb oraz kompozytu Ti23Zr25Nb-9BG jest również widoczna na zdjęciach, przedstawiających hodowle bakteryjne po 24 h inkubacji (Rysunek 13 [4]).

Tabela 1. Aktywność bakteriobójcza materiałów względem bakterii S. mutans [4]

Materiał	CFU/mL po 4 h inkubacji	CFU/mL po 20 h inkubacji	RF %
Ti23Zr25Nb	$<1.0 \cdot 10^3$	$3.2 \cdot 10^4$	78.67
Ti23Zr25Nb-9BG	$<1.0 \cdot 10^3$	$2.4 \cdot 10^4$	84
Ti23Zr25Nb-9BG-Ag	$<1.0 \cdot 10^3$	$3.1 \cdot 10^3$	97.93
Ti23Zr25Nb-9BG-Cu	$<1.0 \cdot 10^3$	$8.5 \cdot 10^3$	94.33
Ti23Zr25Nb-9BG-Zn	$<1.0 \cdot 10^3$	$3.5 \cdot 10^3$	97.67
tytan Grade 2 (próbka kontrolna)	$<1.0 \cdot 10^3$	$2.0 \cdot 10^5$	-

CFU – jednostka tworząca kolonię (ang. colony-forming unit); RF - współczynnik redukcji (ang. reduction factor)

W przypadku badanych preparatów nie zaobserwowano żadnego efektu cytotoksycznego. Intensywność wzrostu komórek kostnych była jednak zależna od składu chemicznego materiału oraz sposobu przygotowania powierzchni. Proliferacja obu lini komórek kostnych po 120 h była intensywniejsza dla próbki modyfikowanej elektrochemicznie niż dla czystego technicznie tytanu oraz stopu Ti23Zr25Nb (% at.). Bardzo korzystne wyniki zaobserwowano również dla kompozytów, w przypadku których względna żywotność komórek względem czystego technicznie tytanu Grade 2 (RVC) była zdecydowanie wyższa od 100% po 72 h hodowli. Po 100 h hodowli proliferacja osteoblastów była intensywniejsza, natomiast w przypadku fibroblastów wyższa lub zbliżona do tytanu (**Rysunek 10** oraz Rysunek 10, 11 [3]).
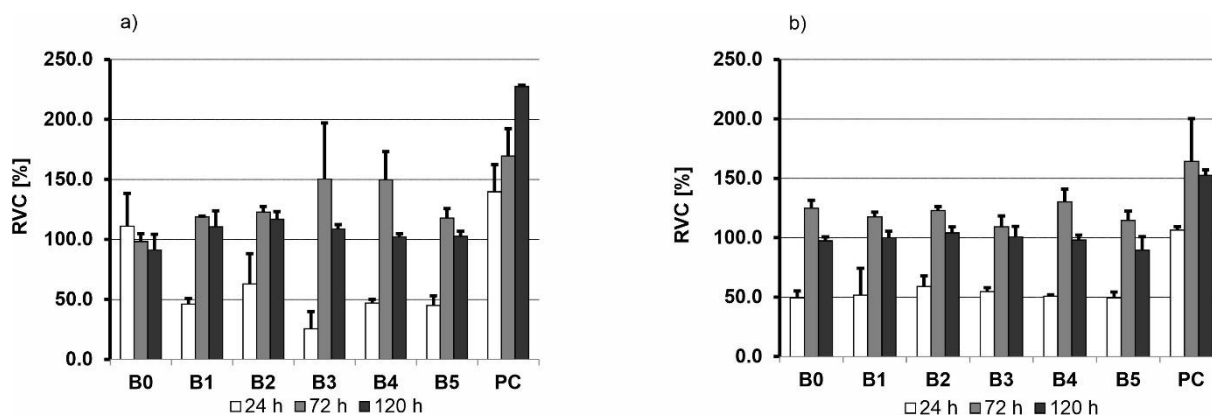
Rysunek 10. Wyniki testu MTS po 24, 72 oraz 120 h celem określenia żywotności komórek NHost (a) oraz HPdLF (b) stopu Ti23Zr25Nb (B0), elektrochemiczne modyfikowanego (B1), kompozytu Ti23Zr25Nb-9BG (B2), Ti23Zr25Nb-9BG-Ag (B3), Ti23Zr25Nb-9BG-Cu (B4), Ti23Zr25Nb-9BG-Zn (B5) oraz kontroli pozytywnej (PC) [3].

3.5. Artykuły wchodzące w skład jedno-tematycznego cyklu publikacji

[1]   **M. Marczewski**, A. Miklaszewski, M. Jurczyk, Structure evolution analysis in ultrafine-grained Zr and Nb-based beta titanium alloys, J. Alloys Compd. 765 (2018) 459-469. https://doi.org/10.1016/j.jallcom.2018.06.224. **(IF 4.175; 100 pkt MNiSW)**

[2]   **M. Marczewski**, A. Miklaszewski, X. Maeder, M. Jurczyk, Crystal Structure Evolution, Microstructure Formation, and Properties of Mechanically Alloyed Ultrafine-Grained Ti-Zr-Nb Alloys at $36 \leq Ti \leq 70$ (at. %), Materials (Basel). 13 (2020). https://doi.org/10.3390/ma13030587. **(IF 3.075; 140 pkt MNiSW)**

[3]   **M. Marczewski**, M.U. Jurczyk, K. Kowalski, A. Miklaszewski, P.K. Wirstlein, M. Jurczyk, Composite and surface functionalization of ultrafine-grained Ti23Zr25Nb alloy for medical applications, Materials (Basel). 13 (2020). https://doi.org/10.3390/ma13225252. **(IF 3.075; 140 pkt MNiSW)**

[4]   **M. Marczewski**, M. Jurczyk, P. Pecyna, M. Ratajczak, M. Gajecka, M.U. Jurczyk, The Effect of 45S5 Bioglass and Ag, Cu, or Zn Addition on the Crystal Structure, Properties, and Antibacterial Effect of Bulk Ti23Zr25Nb Biocomposites, Metals (Basel). 10 (2020). https://doi.org/10.3390/met10091115. **(IF 2.117; 70 pkt MNiSW)**

4. Podsumowanie

W ramach realizowanych badań naukowych wytworzono stopy trójskładnikowe na bazie tytanu, zawierające niob oraz cyrkon. Były one również modyfikowanie objętościowo poprzez dodatek Bioszkła 45S5 oraz srebra, miedzi lub cynku. Tak wytworzone kompozyty były zestawione z próbkami po obróbce powierzchniowej, polegającej na wytworzeniu powłoki, będącej mieszaniną wodorotlenku wapnia oraz hydroksyapatytu. Pozwoliło to na sformułowanie następujących wniosków:

a) dłuższy czas syntezy stopów prowadzi do wzrostu zawartości fazy Ti(β),

b) po konsolidacji proszków, istnieje możliwość wytworzenia stopów jednofazowych Ti-Nb-Zr o strukturze β z ultra drobnym ziarnem, np. stopu Ti23Zr25Nb (% at.),

c) dodatek stopowy niobu wykazuje lepsze właściwości stabilizujące fazę Ti(β), natomiast cyrkonu wpływa na zmianę parametru sieci krystalicznej,

d) dodatek bioszkła prowadzi do uzyskania struktury wielofazowej (utrata struktury jednofazowej β) po przeprowadzonym procesie spiekania,

e) wprowadzenie bioszkła do stopów Ti-Nb-Zr wpływa na poprawę odporności korozyjnej oraz obniżenie modułów Younga badanych materiałów (43.3 GPa dla stopu zawierającego 9% wag. Bioszkła 45S5) poniżej modułu Younga, charakteryzującego piankę na bazie stopu Ti23Zr25Nb, co daje możliwość ograniczenia występowania zjawiska „stress shielding",

f) modyfikacja kompozytu , zawierającego 9% wag. Bioszkła 45S5 srebrem pozwala na dalsze obniżenie prądów korozyjnych do wartości niższych od komercyjnego, czystego technicznie tytanu Grade 2,

g) kompozyty Ti23Zr25Nb-9BG-Ag (Cu, Zn) posiadają wysoką aktywność bakteriobójczą względem bakterii *S.mutans*, powodującej próchnicę zębów, co daje możliwość ograniczenia powikłań powszczepowych materiału,

h) proliferacja komórek kostnych (fibroblastów oraz osteoblastów) na badanych materiałach jest równa lub wyższa w odniesieniu do czystego technicznie tytanu Grade 2,

i) obróbka powierzchniowa wpływa na poprawę odporności korozyjnej stopu Ti23Zr25Nb (% at.), jednakże w sposób mniej efektywny niż tworzenie układów kompozytowych.

Publikacje

Artykuł nr 1:

M. Marczewski, A. Miklaszewski, M. Jurczyk,

Structure evolution analysis in ultrafine-grained Zr and Nb-based beta titanium alloys

Structure evolution analysis in ultrafine-grained Zr and Nb-based beta titanium alloys

M. Marczewski, A. Miklaszewski[*], M. Jurczyk

Institute of Materials Science and Engineering, Poznan University of Technology, Jana Pawla II No 24, 61-138 Poznan, Poland

ARTICLE INFO

ABSTRACT

Titanium beta type alloys with an ultrafine grain microstructure are interesting biomaterials that exhibit an excellent mechanical, physicochemical and biological properties. This study aimed to develop a new Ti14Zr16Nb and Ti23Zr25Nb (at. %) alloys. These materials were prepared by the combination of mechanical alloying and powder metallurgy approach with cold powder compaction and sintering or interchangeably hot pressing. The details of the processing method were presented for structure evolution analysis. The samples were characterized by an X-ray diffraction method, scanning electron microscopy observation, chemical composition determination, sinters porosity measurements and finally mechanical properties evaluation. The microscopic studies confirmed the ultrafine grain structure of the sinters. The mechanically alloyed Ti23Zr25Nb material upon sintering at 600 °C for 10 min led to the formation of the single β type phase structure. The present study has demonstrated that ultrafine structure for Ti14Zr16Nb and Ti23Zr25Nb systems proposed for medical implant applications can be fabricated by the application of hot pressing of mechanically alloyed powders at the temperature below $\alpha \rightarrow \beta$ transus (600 °C).

1. Introduction

Titanium alloys are one of the most popular materials used in medicine. They are applied in the hard tissue implants as hip or dental implants, screws, nails, etc [1]. There might be some medical issues related to the use of the commercially available materials as Ti6Al4V. The presence of aluminium and vanadium may cause medical disorders as neurological disorders (Alzheimer disease, etc.). Because of that fact, many researchers try to find their replacement [1—4]. By the elimination of toxic elements, it is possible to prepare Ti-type alloys with excellent biocompatibility. Ti—6Al—7Nb, which has been developed for surgical implants, is also attractive for dental applications [5]. Recently, other alloys as Ti—40Zr, Ti—5Al—13Ta, and Ti—43.1Zr—10.2Al—3.6 V have been also proposed [5,6].

Ti-Nb-Zr alloys are one of the other substitutes. It is due to the fact of their chemical composition the phase (β-type titanium alloys) structure, and mechanical properties stay attractive in the biomedical field of application. The alloyed cubic titanium structure allows making the Young modulus much lower even 50 GPa. Above relation minimize the risk of mechanical unfit between the bone tissue and the implant. The problems of bones resorption and loosening of the implants due to of stress-shielding effect could be in above manner significantly reduced [1,7—9].

Some researchers at the base of theoretical studies of beta Ti-type binary and ternary systems, try to calculate theoretical values of Young modulus which depend on the contents of the element [10]. The most favourable Young modulus (50 GPa) was estimated for Ti(β) alloy with 25 at. % of niobium and 6.25 at. % of zirconium [10]. The content of niobium and zirconium may influence the titanium alloy cell toxicity. Cell toxicity can also be influenced by others factors as surface properties or manufacturing steps [11].

There are also many others elements, stabilizing β-structure as tantalum, molybdenum or palladium. All of these elements allow us to decrease the Young modulus and make it much more similar to the Young modulus of bone. At this point of discussion, it is essential to mention that proper processing condition should also be however maintained. Formation of other phases like α or ω-phase, during for example heat treatment procedures may provide

* Corresponding author.
E-mail address: andrzej.miklaszewski@put.poznan.pl (A. Miklaszewski).

an increase of the modulus. On the other hand, martensite phases as α' and α'' decrease it [1,7,9].

The Ti-Nb-Zr alloys could be produced in multiple manners. So far, the most popular one stay: vacuum arc remelting (VAR), vacuum induction melting (VIM), induction skull melting (ISM), plasma arc melting (PAM), electron beam melting (EBM) [12,13]. Very interesting and possessing high potential in the meaning of final products possible cost reduction approach, stays powder metallurgy (PM) method [2,4,14].

One of the methods of Ti-based alloys powder preparation is the mechanical alloying (MA) which allows to obtained nanocrystalline materials [2,4]. Mechanical alloying could be controlled with some parameters like; milling time, additional agents (lubricants, etc.), ball-to-powder mass ratio (BPR), milling atmosphere, milling temperatures (cryomilling as the process conducted at lower temperatures), materials of vial, reactor and balls, type of used mill, vibration frequency (milling speed), etc. [15]. Mechanical alloying allow to improve material properties because of the nanocrystalline or ultrafine structure transition and what was also confirmed in other research new phase formation. One of the other example could be the hardness improvement because of the grain boundary strengthening mechanism. Moreover, this process has the tremendous economic benefit (the process of MA stays uncomplicated and just cheaper than vacuum arc melting or other
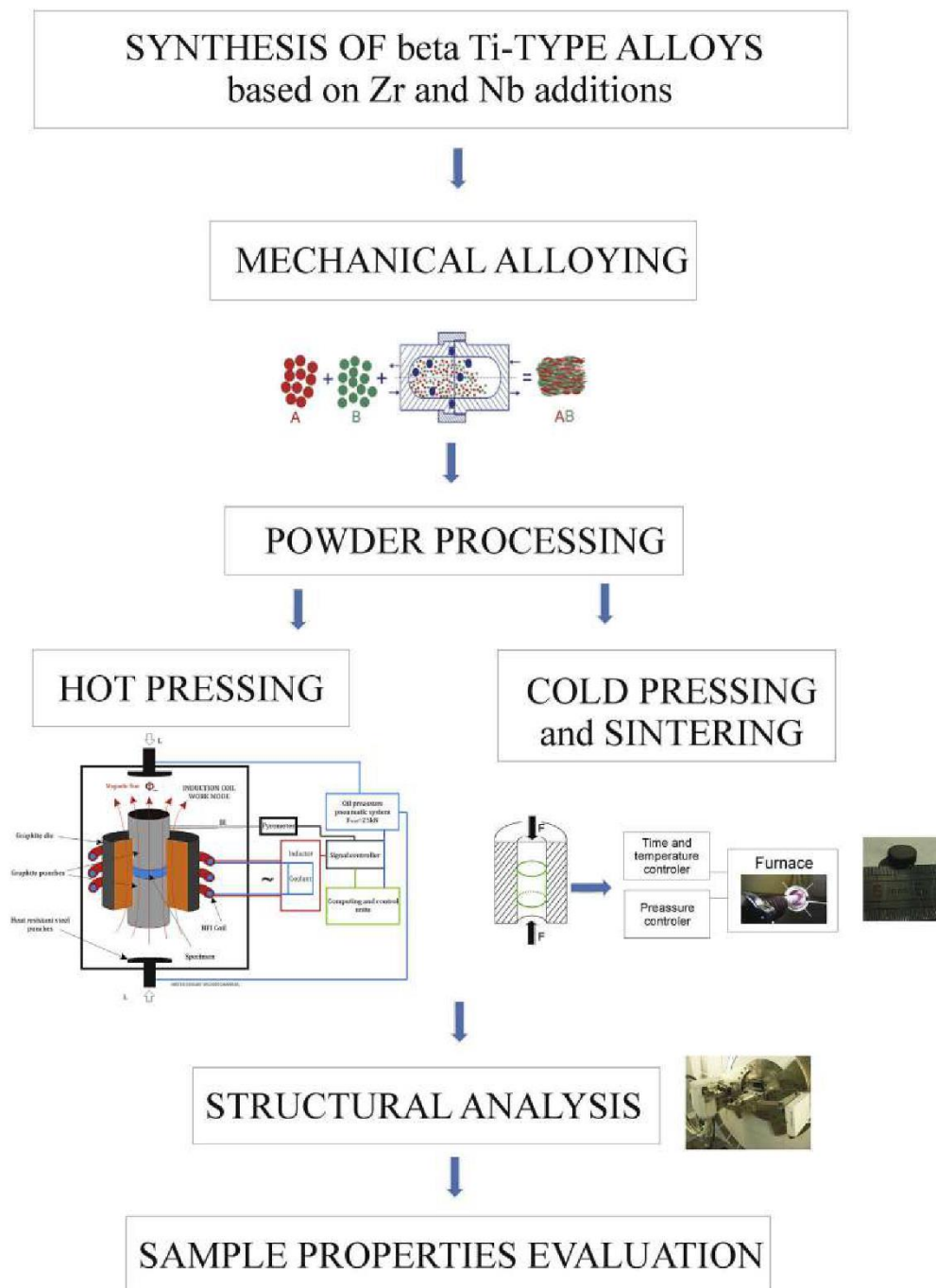

Fig. 1. Processing scheme assumed for nanocrystalline beta titanium alloys consolidation and sintering.

conventional methods), it is not difficult to perform, and it gives the better homogenising effects [2].

New perspectives appear for the transitional sized materials that exhibit better mechanical and physicochemical properties in comparison to their microcrystalline counterparts [16,17]. Recent studies showed for instance that for the titanium example, size transition could considerably improve not only the mechanical properties but also the biocompatibility [17–21]. For example, the strength of the titanium could be nearly twice of that of conventional CP titanium [22].

Also, other properties like corrosion resistance, which tests were performed for microcrystalline Ti-Nb-Zr alloys showed that these materials are passive in Ringer's solution without fluorides and in Ringer's solution with 1000 ppm of fluorides at 5 or 7.5 pH. It was also observed that corrosion resistance of this alloys decreases with fluorides content and lower pH [23].

While Ti-based biomaterials have been successful at encouraging bone ingrowth both in vivo and in clinical trials, the range of materials and microstructures available is still rather limited. To optimize titanium alloys for medical implant applications use, several studies have focused on the design of biomaterials with planned architecture to fulfil physicochemical, mechanical as well as regeneration requirements. For example, current studies remain focused on fabricating Ti-based porous biomaterials to promote bone or tissue ingrowth into pores and to provide biological anchorage. Several factors have been demonstrated to have an influence on bone ingrowth into porous implants, such as the porous structure (pore size, pore shape, porosity and interconnecting pore size) of the implant, duration of implantation, biocompatibility, implant stiffness, micromotion between the implant and adjacent bone, etc. Additionally, the architecture of a porous implant has been suggested to have a significant effect on the implant integration with newly grown bone [24,25]. The goals in the development of new Ti-based biomaterials are: (i) to avoid potentially toxic elements (such as vanadium), (ii) to produce titanium alloys with a low modulus and high fatigue strength, (iii) to improve biocompatibility by the bulk or surface modification approach. Currently, it is possible to prepare β-type titanium alloys with excellent biocompatibility [21].

The significant progress for the Ti-Nb-Zr type alloys was made by Hussain team [2] for Ti20Nb13Zr (at. %) composition. It should, however be noted that proposed composition, not allowed to form a single Ti(β) phase even for a high-temperature range of processing 1200 °C (visible highly intense Ti(α) peaks). To form a single β-phase type structure, other research was done on the Ti30Ta10Nb20Zr (wt.%) [26].

Proposed in this work Ti23Zr25Nb alloy composition processed at 600 °C, is characterized by a single Ti(β) phase type structure. Less expensive mixture and significant processing temperature reduction remain as an evident improvement achieved in this work in oppose to the previously mentioned research [2,26]. According to our knowledge, nobody manufactured titanium-niobium-zirconium (Ti14Zr16Nb and Ti23Zr25Nb (at. %)) type alloys within ultrafine grain structure and studied their phase transformation or microstructure till now. The profitability of undertaken actions of composition and processing condition change could only be justified by the expected property enhanced. Biomaterials in the same, with the ultrafine grain titanium-based alloy structure, defines a new biomaterial group, with better mechanical properties, that consequently may provide the savings in health care system and accelerate recovery time expectations for the markedly growing group of final consumers.

2. Experimental details and research methodology

2.1. Chemicals and materials

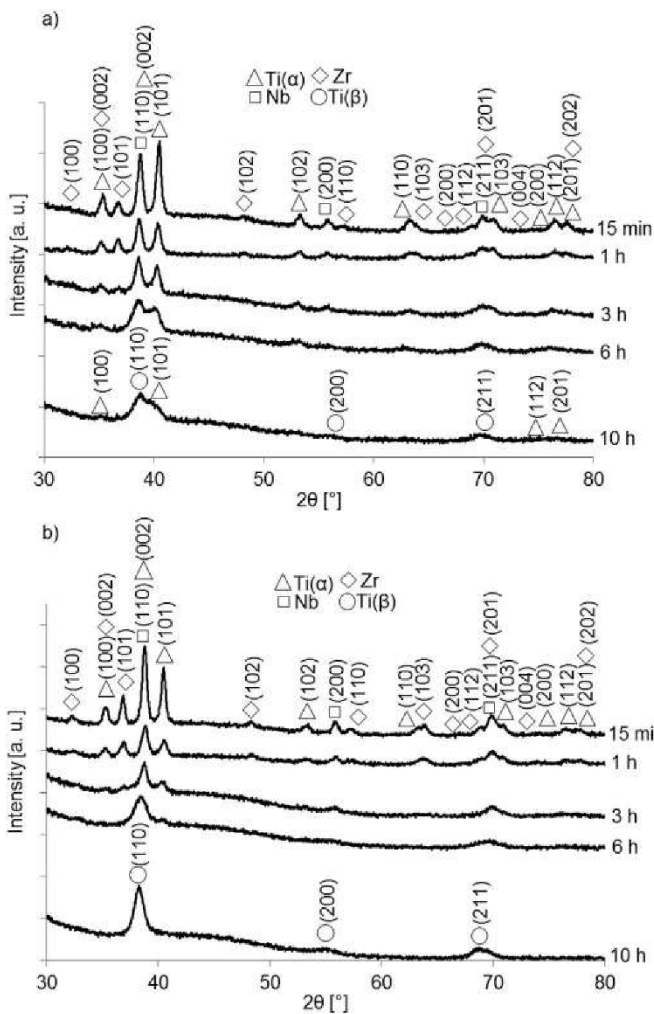The commercial Ti (Alfa Aesar, 99.9% purity, CAS:7440-32-6), Nb

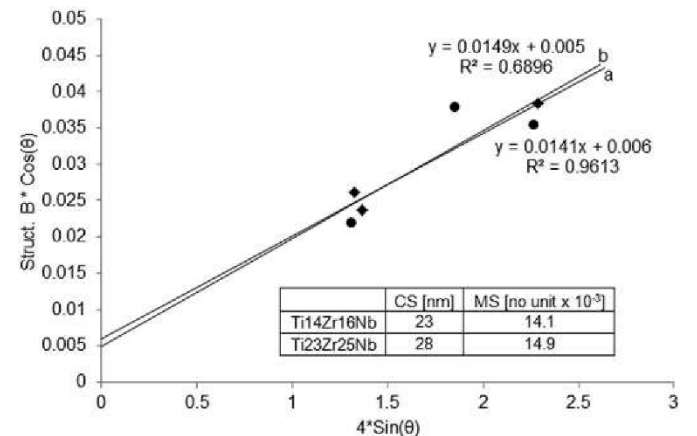**Fig. 2.** XRD spectra of Ti14Zr16Nb (a) and Ti23Zr25Nb (b) powders mechanically alloyed for different times.

Fig. 3. Linear Williamson-Hall plots with estimated crystallite size (CS) and microstrain (MS) factors based on the XRD spectra of Ti14Zr16Nb (a) and Ti23Zr25Nb (b) powder materials after 10 h of mechanical alloying.

powders (Sigma Aldrich, 99.8% purity, CAS:7440-03-1) and Zr fillings from sponge (Sigma Aldrich, ≥ 99%, CAS:7440-67-7) were used. The experiments were carried out on Ti14Zr16Nb and Ti23Zr25Nb (at. %) alloys.

2.2. Sample preparation

Mechanical alloying was performed using SPEX 8000 Mixer Mill (SPEX® SamplePrep, Metuchen, NJ, USA). Argon was a protective atmosphere. Round bottom stainless vials were used. Elemental
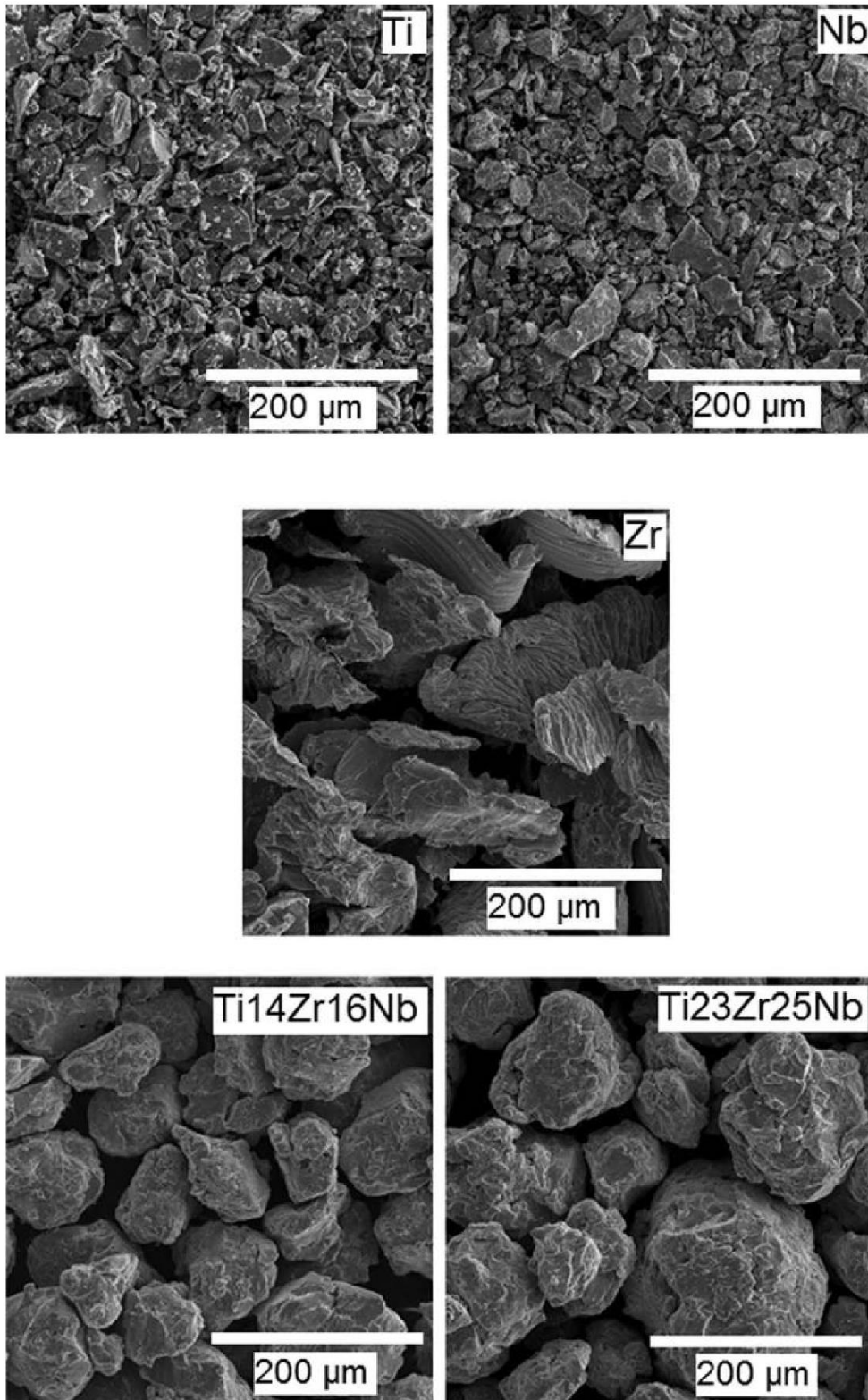
Fig. 4. SEM microphotographs of Ti, Zr, Nb elemental powders and Ti14Zr16Nb as well as Ti23Zr25Nb powder agglomerates after 10 h of MA.

powders (Ti, Zr and Nb, all μm in size) was weighted, blended and poured into vials in the glove box (LabMaster 130) filled with automatically controlled argon atmosphere ($O_2 < 2$ ppm and $H_2O < 1$ ppm). MA process was lasted up to 10 h in all cases. In the next step, the produced powders were processed by powder metallurgy process by the application both cold and hot processing methods according to the scheme depictured in Fig. 1. In the case of hot pressing, induction coil module was used for a conductive die heating by the Joule's heat generated on it the surface. Additional the module allows to control, during sintering procedure the force, temperature, and vacuum with the 0.1s duration. Control temperature measurement variance is kept at $\pm 25\,°C$ variability. The diameter and height of the obtained bulk samples were 6 mm and 4 mm, respectively. For traditional cold compaction and sintering approach, the pressure of 600 MPa was adopted for powders consolidation. The samples were next sealed in a quartz tube filled with an argon atmosphere after several vacuum flushing. Four

temperatures of sintering as 600, 750, 800, 850 and 1000 °C were proposed within a 1800s heating argon atmosphere regime with following fast water cooling. Hot pressing was conducted at 600 °C for 300 s within a 600 s heating up step in a vacuum condition (50 Pa) with an acting pressure of 71 MPa.

2.3. Materials characterization

The crystallographic structure of the samples during different processing stages was investigated at room temperature using a Panalytical Empyrean XRD equipment with CuKα radiation (Almelo, Netherlands). The conditions of XRD measurements was as follows: voltage 45 kV, anode current 40 mA, 2 Theta range 30–80 [°], time per step 60.325 [s/step], step size 0.0334 [°]. Obtained spectra were refined for parameters and variables as a background and profile coefficients, lattice parameters, linear absorption coefficients. The instrumental broadening effect for
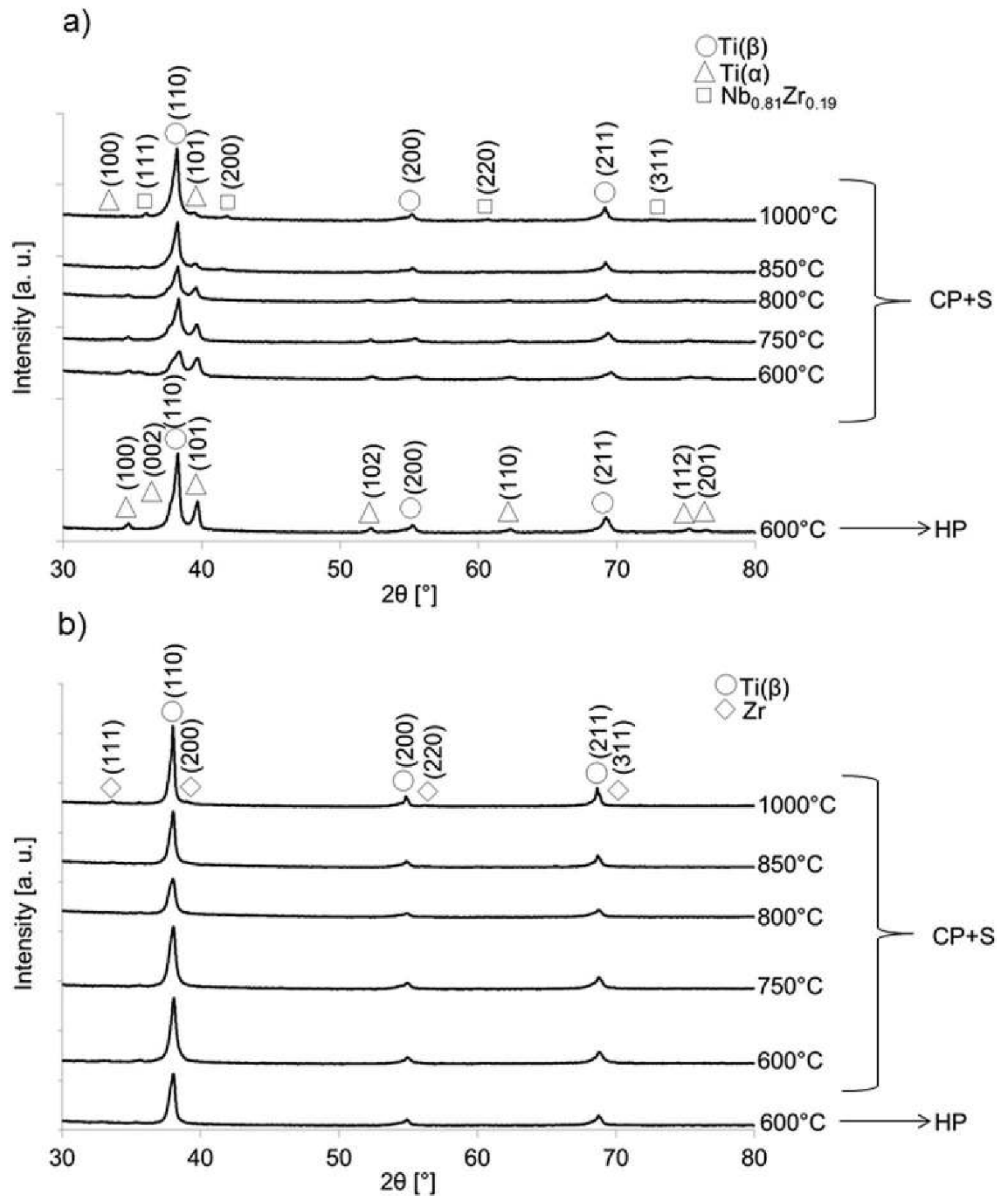
Fig. 5. XRD spectra of bulk Ti14Zr16Nb (a) and Ti23Zr25Nb (b) samples sintered at different temperatures for 0.5 h in an argon atmosphere and hot pressed at 600 °C for 10 min in vacuum conditions.

collected data was eliminated by subtracting the full width at half-maximum (β_o) of a standard (Si) sample from β of the respective Bragg peaks. The Williamson-Hall (W-H) analysis method was used to study crystallite size and lattice strain on the peak broadening of the obtained mechanical alloyed powders spectra for assumed uniform deformation model. Each point at linear W-H analysis is assigned to a specific diffraction line, after the point collection, a linear regression should give a linear fit which allows to estimate the material strain component from the slope and the size component from the intercept.

The lattice parameter estimation as also phase quantitative analysis was based on the Rietveld profile fitting method realized on the Maud software. Apply approach involve the simulation of the diffraction pattern based on the analyzed structural model for:

- Ti(α) (ref. code 01-071-4632),
- Ti(β) (ref. code 01-074-7075),
- Nb0.81Zr0.19 (ref. code 00-049-1455),
- Zr (ref. code 01-088-2329).

The calculated pattern of the model structure was fitted to the observed one by minimization of the sum of the squares and after refinement using Marquardt least squares algorithm which achieves high goodness of fit (S < 2,5). For clearance, residual pattern indicators of modelled data as:

- R_{wp} — weighted pattern residual indicator
- R_{exp} — expected residual indicator
- S — goodness of fit were revealed.

Scanning electron microscope (SEM, VEGA 5135 Tescan, Brno, Czech Republic) with energy dispersive spectrometer (EDS, PTG Prison Avalon, Princeton Gamma Tech., Princeton, NY, USA) was used to characterize microstructure and chemical composition of the prepared samples. EDS analyzer was calibrated using a typical Cu calibration procedure.

The porosity of the porous materials was estimated by GIMP software from the histograms analysis of optical microscope photographs. The densities of the samples were calculated by the formula $\rho = (1 - P/100) \times \rho_{th}$, where ρ and ρ_{th} are the density of the porous material and its corresponding theoretical density calculated from the rule of the mixtures. The microhardness measurements were carried out on samples in order to determine average hardness by Innovatest Nexus Vickers tester with an applied load of 300 g and loading time 10 s.

The modulus analysis of selected samples based on the EIT (indentation modulus) estimation, was realized on CSM Instruments with Berkovich tip. The measurement was carried out with nanoindenter using DIN 50 359/ISO 14577 standard, and load parameters of the test as;

$$F = 300\text{mN}/20\text{s}$$

$$C = 5\text{s}$$

Obtained results were compared with the commercially available rod titanium (Grade 2) sample at the annealed state.

3. Results and discussion

3.1. Powder stage

The aim of this research was a synthesis of Ti14Zr16Nb and Ti23Zr25Nb alloys by mechanical alloying and powder metallurgy methods. The crystallographic structure changes during MA was investigated. Fig. 2 shows XRD patterns of the mechanically alloyed Ti, Zr and Nb powders for different milling times. In both cases, after 15 min of MA of Ti14Zr16Zr (Fig. 2a) and Ti23Zr25Nb (Fig. 2b) mixtures, the characteristics lines of Ti (α), Zr and Nb are visible. After 3 h of MA, the (101) plane from hexagonal Zr crystal structure almost disappeared, and additionally, after 6 h new phase Ti(β) (2 theta = 38.59(2) for Ti14Zr16Zr and 2 theta = 38.41(1) for Ti23Zr25Nb [°]) is forming for considered alloys compositions. The high plastic deformations of the powders result in a high density of dislocation lines and subsequently, subgrains formation that may finally lead also to amorphisation [15]. After 10 h of mechanical alloying the crystallite sizes calculated by the application of Williamson-Hall approach were 23 and 28 nm for Ti14Zr16Nb and Ti23Zr25Nb alloys, respectively (Fig. 3). During the MA process, the transformation from Ti(α) to Ti(β) phase is observed. The zirconium and niobium contents and milling time are main parameters which control this transformation. Finally, it is necessary to mention that application of MA process reduces not only the elements of the microstructure of so produced alloys but also increases the microstrain (in average $14-15 \times 10^{-3}$) of so produced materials (Fig. 3).

Fig. 4 shows SEM microphotographs of starting powders (Ti, Zr and Nb) and Ti14Zr16Nb and Ti23Zr25Nb agglomerates obtained after 10 h of MA process. Most of the agglomerated particles have a size which varies from 50 to 150 μm. Some of the Ti14Zr16Nb powder agglomerates had a sharp boundaries which weren't observed for Ti23Zr25Nb powder agglomerates. A microstructure

Table 1
Crystallographic data analysis of bulk Ti14Zr16Nb and Ti23Zr25Nb samples sintered at different conditions by a cold and hot pressing approach.

Sample	PP	PT [°C]	Ti(α) a [Å]	c [Å]	V [Å^3]	PA [%]	Ti(β) a [Å]	V [Å^3]	PA [%]	Additional phase Nb0.81Zr0.19 a [Å]	V [Å^3]	PA[%]	R_{wp} [%]	R_{exp} [%]	S
Ti14Zr16Nb	CP+S	600	2.9862(4)	4.7566(14)	36.73(2)	44.83	3.3218(3)	36.65(1)	55.17	—	—	—	4.86	3.35	1.45
		750	2.9853(4)	4.7761(15)	36.86(3)	26.54	3.3255(3)	36.78(1)	73.46	—	—	—	5.67	3.20	1.77
		800	2.9908(5)	4.7843(19)	37.06(3)	26.20	3.3313(3)	36.97(1)	73.80	—	—	—	6.28	3.65	1.72
		850	2.9903(11)	4.7817(41)	37.03(6)	9.94	3.3327(2)	37.02(1)	88.64	4.3477(25)	82.18(14)	1.42	7.35	3.39	2.17
		1000	2.9972(16)	4.7798(63)	37.18(9)	2.69	3.3357(2)	37.12(1)	96.02	4.3214(14)	80.70(8)	1.29	6.58	3.04	2.17
	HP	600	2.9844(4)	4.7688(12)	36.78(2)	31.32	3.3298(2)	36.92(1)	68.68	—	—	—	6.37	2.74	2.32
										Zr					
Ti23Zr25Nb	CP+S	600	—	—	—	—	3.3440(1)	37.39(1)	100	—	—	—	4.86	2.67	1.82
		750	—	—	—	—	3.3495(2)	37.58(1)	100	—	—	—	5.19	2.60	2.00
		800	—	—	—	—	3.3524(2)	37.68(1)	100	—	—	—	5.05	3.08	1.64
		850	—	—	—	—	3.3500(2)	37.60(1)	99.50	4.6035(30)	97.56(19)	0.50	5.46	2.97	1.84
		1000	—	—	—	—	3.3500(2)	37.60(1)	99.07	4.6077(25)	97.83(16)	0.93	6.76	2.74	2.46
	HP	600	—	—	—	—	3.3507(2)	37.62(1)	100	—	—	—	6.73	3.17	2.12

that forms during MA consists of layers of the starting materials mixture. A lamellar structure is increasingly refined during further mechanical alloying. A thickness of materials decreases with increase in mechanical alloying time resulting in the alloy formation. Obtained final particle morphology is in agreement with the plastic deformation mechanism of mechanically alloyed components and its reciprocal amount during tensile fracture.

3.2. Bulk stage

Both MA compositions according to processing scheme depictured on Fig. 1, were cold pressed and sintered at four temperatures of 600, 750, 800, 850 and 1000 °C for 0.5 h at argon atmosphere as also hot pressed in 600 °C in vacuum conditions. Fig. 5 shows XRD spectra of so produced bulk samples. The most intense peaks on all patterns are related to Ti(β) type phase. In the case of cold pressed and sintered Ti14Zr16Nb alloy, additionally to main Ti(β) phase, two minor phases are visible: Ti(α) (ref. code 01-071-4632) and $Nb_{0.81}Zr_{0.19}$ (ref. code 00-049-1455). On the other hand, in the case of a Ti23Zr25Nb alloy, additionally to main Ti(β) phase, a trace of Zr is visible after sintering at 850 or 1000 °C (ref. code 01-088-2329).

Single phase β-type Ti23Zr25Nb alloy was produced in the sintering temperature range 600–800 °C. At temperatures starting from 850 °C small content of pure Zr was observed. In the case of a Ti14Zr16Nb alloy, additionally to the main Ti(β) phase, the second phases such as Ti(α) and Nb0.81Zr0.19 were detected. The content of Ti(α) phase in the Ti14Zr16Nb alloy is decreasing with increasing sintering temperature as a Table 1 confirms. At 1000 °C the content of the main Ti(β) phase was about 96%. Except the value of the heat treatment temperature, the amount of Nb and Zr in the Ti-Zr-Nb system shows as the results confirm, high sensitivity on the final phases content of so produced alloys.

In the case of samples obtained after hot pressing in 600 °C in vacuum conditions, namely low-temperature sintering, the bulk materials are formed (Fig. 6). For the Ti23Zr25Nb starting composition, single phase β-type alloy was produced. In the case of Ti14Zr16Nb composition, additionally to the main Ti(β) phase alloy, the second Ti(α) phase is detected (Fig. 5) and it content determined by Rietveld analysis locate at 31.32%.

According to gathered in Table 1 data, the structural dimension relation and analyzed phases amount remain dependent on the processing treatment approach as also starting elements composition.

For the Ti14Zr16Nb sample obtained by traditional CP+S approach, the increase of the Ti(β) cubic phase structure amount by the reduction of Ti(α) hexagonal phase, related to processing temperature condition, shows also a deeper underlying structural relation. Analyzed for the obtained sinters titanium phase structures, expands as the calculation shows the average dimension of the cubic and hexagonal cells by the movement of the atoms, due to sintering temperature increase, until the $\alpha \rightarrow \beta$ transus become

Table 2
Obtained properties of the bulk Ti14Zr16Nb and Ti23Zr25Nb samples sintered at different conditions by a cold and hot pressing approach.

Sample	PP	PT [°C]	TD [g/cm³]	Porosity [%]	D[g/cm³]	HV0.3
Ti14Zr16Nb	CP+S	600	5.93(20)	18.2 ± 2.9	4.85(34)	446(11)
		750	5.93(20)	14.5 ± 2.8	5.07(34)	409(17)
		800	5.93(20)	14.9 ± 3.2	5.05(36)	407(5)
		850	5.93(20)	13.4 ± 2.9	5.14(35)	398(7)
		1000	5.93(20)	15.0 ± 3.6	5.04(39)	402(12)
	HP	600	5.93(20)	0.3 ± 1.2	5.91(27)	399(10)
Ti23Zr25Nb	CP+S	600	6.50(20)	27.5 ± 3.4	4.71(37)	392(18)
		750	6.50(20)	19.6 ± 3.4	5.22(38)	384(13)
		800	6.50(20)	21.6 ± 3.7	5.09(40)	375(33)
		850	6.50(20)	22.9 ± 3.2	5.01(36)	397(8)
		1000	6.50(20)	27.9 ± 3.1	4.68(35)	426(5)
	HP	600	6.50(20)	1.9 ± 1.7	6.37(31)	407(6)
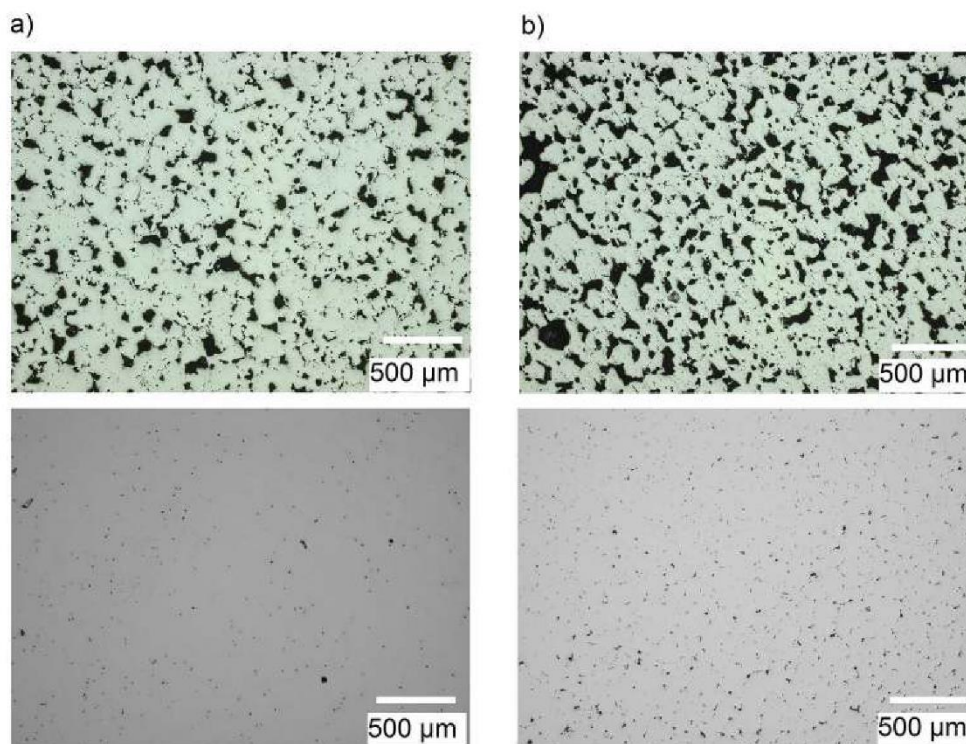
Fig. 6. OM microphotographs of bulk Ti14Zr16Nb (a) and Ti23Zr25Nb (b) samples produced by the application of HP method (600 °C/10 min). The microstructures of the same materials obtained after cold pressing with additional sintering at the same temperature (600 °C/0.5 h) were also presented.

reached. Above 850 °C the structure dimensions growth is sustained only for the cubic phase as for the hexagonal the diminishment is observed. In the case of the increase alloying elements content for Ti23Zr25Nb example, obtained in the sinters beta phase structure, expands the cell dimension with growing sintering temperature also until the $\alpha \rightarrow \beta$ transus become reached. Above 850 °C, the Ti (β) cell dimension become reduced similarly to the behaviour of the Ti(α) structure in the two-phase $\alpha+\beta$ system considered for the lower alloyed example. The observed relation may point out for the obtained phases it's stability, due to the analyzed influence of composition, processing path (PP) and temperature (PT) treatment conditions. Considered also structural data of HP samples, located them in examined compositions for traditional CP+S approach between 750 and 800 °C regime. Above results suggest that due to simultaneously force and temperature acting not only the economic benefits due to the lower processing treatment requirements could be obtained. For the bulk Ti14Zr16Nb and Ti23Zr25Nb alloys produced by HP at 600 °C for 10 min in vacuum conditions (Fig. 6), analyzed porosities summarized in Table 2 were 0.3 and 1.9% respectively.

The bulk samples of Ti14Zr16Nb and Ti23Zr25Nb alloys, produced by cold pressing and sintering at different temperatures for 0.5 h in an argon atmosphere, were composed of irregular particles and show porous morphology (Fig. 6). Porosity depends heavily on the type of material (size of agglomerates) and it's chemical composition what was confirmed and summarized in Table 2. The low-temperature sintering at 600 °C for 30 min, allows obtaining the bulk materials.

Obtained average microhardness results of all analyzed samples show close to 400 HV values without visible relation to phase amount calculations based on structural data. The smooth bulk Ti14Zr16Nb and Ti23Zr25Nb alloy surfaces were also presented in Fig. 7 with the EDS result analysis that confirmed the chemical composition for the HP samples.

The SEM analysis was conduct to confirm in obtained sinters ultrafine grain structure. Highly magnified in BSE mode, HP samples presented in Fig. 8, shows independently phase contrast relation and microstructure size range. Obtained microstructure shows uniform grain size distribution, however, in the case of a Ti23Zr25Nb alloy, the grains are more refined.

Indentation modulus estimation of the selected samples depictured on Fig. 9 by the load-depth curves shows the expected properties course relation. Confirmed structurally for the hot pressed as well as cold compacted and sintered at 600 °C - Ti14Zr16Nb and Ti23Zr25Nb samples phase composition relates to a higher average EIT values results obtained for a) and b) samples than c) and d) one. Crucial in above comparison stays, however, obtained not only sample phase composition, but also the porosity
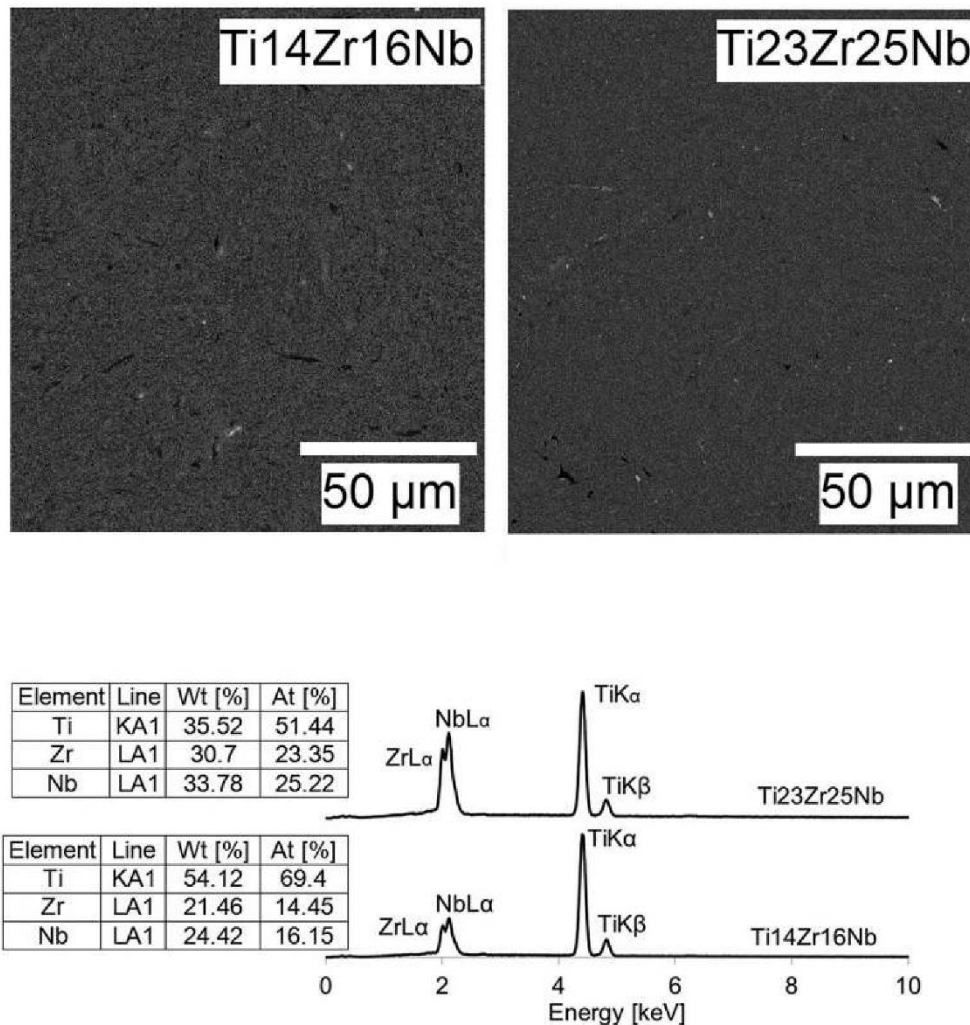

Fig. 7. SEM microphotographs and EDS spectra of Ti14Zr16Nb and Ti23Zr25Nb alloys, mechanically alloyed for 10 h and HP at 600 °C for 10 min.
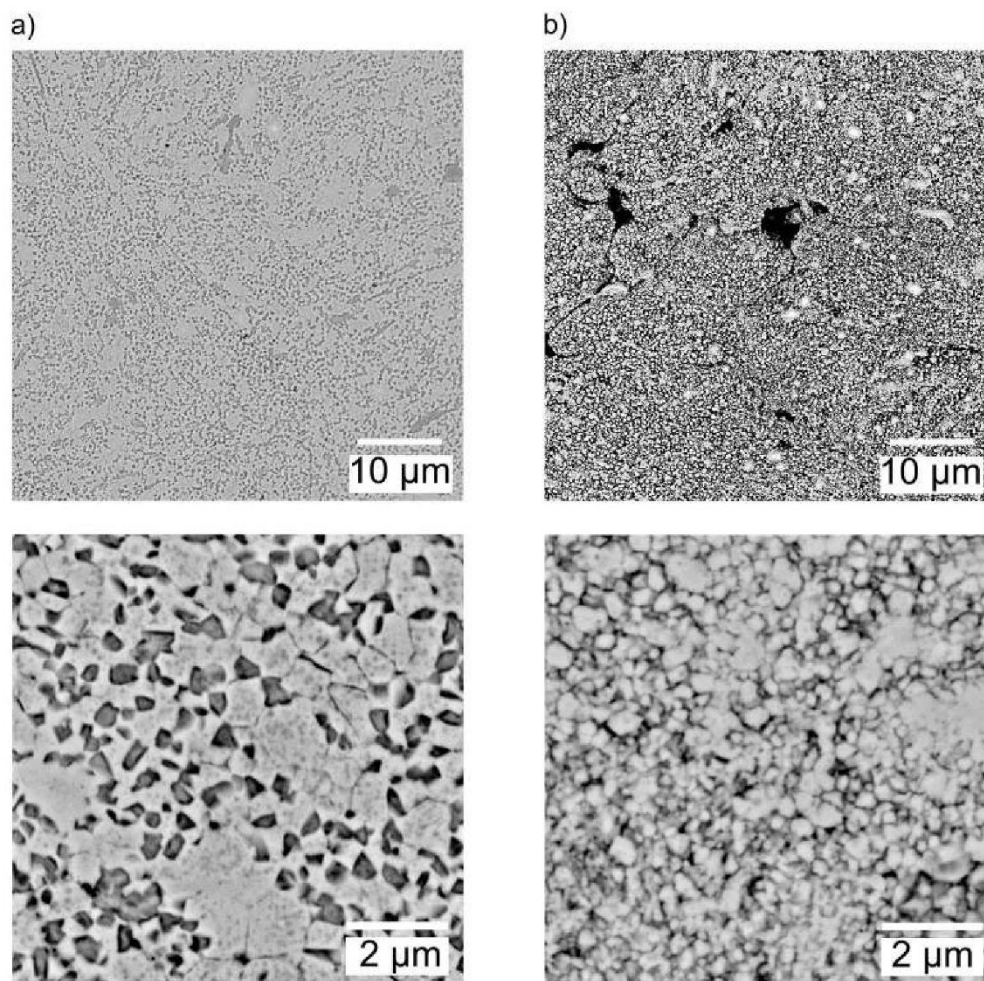
Fig. 8. SEM microphotographs of Ti14Zr16Nb (a) and Ti23Zr25Nb (b) alloys, mechanically alloyed for 10 h and HP at 600 °C for 10 min - BSE mode.

share. For above, less concise cold compacted and sintered samples b), d) characterize with the lower EIT values despite dual phase microstructure than the hot pressed a), c) one. Above results compared with Ti-G2 rod sample at the annealed state, points out evident EIT diminishment. Additionally, arrange results deserves also proper attention due to a high applied 300 mN measurement load.

Many different methods for producing nanocrystalline and/or fine-grained structures are available [27]. They are mainly based on the production of fine-grained powders and a subsequent powder metallurgy for consolidation [15]. Presented results clearly demonstrate that powder manufacturing route allows production of β Ti-based alloys for biomedical applications. It is well proven that refinement of the grain structure can significantly enhance the mechanical properties of Ti-based alloys. Grain refinement is a key principle in the strengthening of engineering alloys. Our results show that the crystal structure of solution treated alloys are not only sensitive to Zr and/or Nb contents but also on the value of sintering temperature. When Nb content increases, the β phase becomes the only dominant phase in Ti-Zr-Nb system. The Nb stabilizes the β-Ti structure and promotes the spontaneous passivation of the alloys [28]. Additionally, Zr is a neutral element that can help to suppress the ω-phase and in many compositions may have special properties such as a shape memory effect [29,30]. However, in ternary alloys, Zr increases the amount of β-Ti, being responsible for the single phase structure formation which couldn't

be achieved without this additive. Both these elements are very resistant in physiological liquids due to its natural oxide films. The control of the crystalline phases is of great importance in the design of new alloys for biomedical applications, and what was proven in this work stays reliant on the composition, processing temperature and applied manufacturing approach.

4. Conclusions

The aim of this research was a synthesis of new Ti14Zr16Nb and Ti23Zr25Nb alloys by mechanical alloying and powder metallurgy methods including cold and hot pressing. The influence of Nb and Zr contents as also processing conditions on phase transitions ($\alpha \rightarrow \beta$) and microstructure were studied. The following conclusions can be withdrawn:

— longer MA powder processing time for analyzed compositions increase the content of Ti(β) - phase in Ti-Zr-Nb system (Fig. 2),
— crystallization of the MA powder materials due to acting processing treatment temperature led to the formation of ultrafine grain structured Ti(β) type alloys (Fig. 8),
— with the increase of Nb and Zr contents in Ti-Zr-Nb system increase of Ti(β) phase is noticeable,
— with the increase of sintering temperature more Ti(β) - phase in the Ti14Zr16Nb system is noticeable,
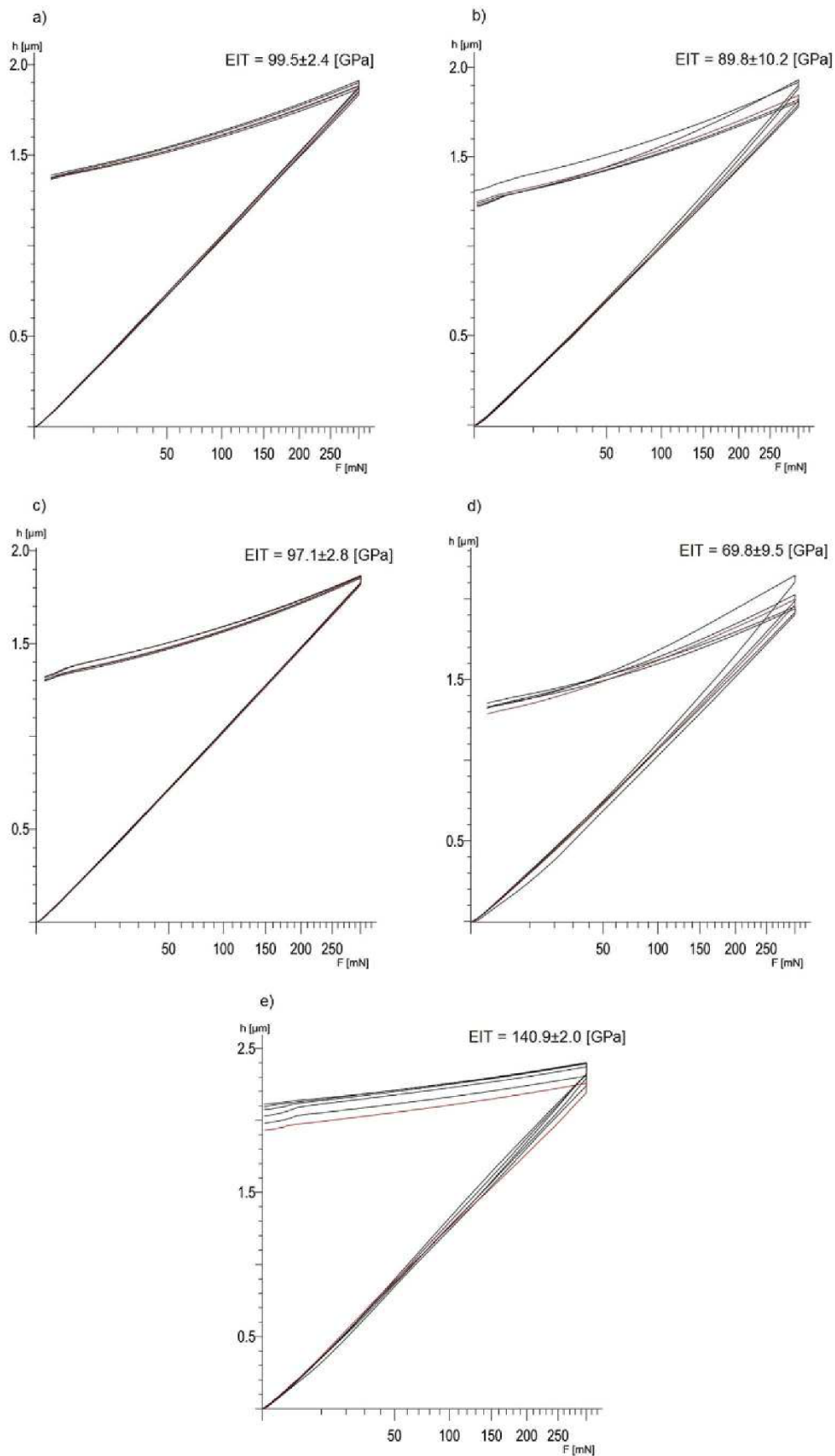
Fig. 9. Load-depth curves of bulk Ti14Zr16Nb (a) and Ti23Zr25Nb (c) samples prepared by the hot pressing and cold pressing with additional sintering Ti14Zr16Nb (b) and Ti23Zr25Nb (d) at the same processing temperature 600 °C. The curves of rod titanium (G2) sample in the annealed state (e) were also reviled.

- the hot pressing process at low temperature (600 °C) of Ti14Zr16Nb characterizes with increase content of Ti(β) phase in the alloy in comparison with the cold pressing process.
- proposed low-temperature sintering (bellow $\alpha \rightarrow \beta$ transus) results in bulk materials formation.
- Indentation modulus estimation of obtained in this work sinters, confirms lower values for β type titanium alloys with the ultrafine grain structure staying however related to the sample porosity shear.

Acknowledgements

References

[1] M. Geetha, A.K. Singh, R. Asokamani, A.K. Gogia, Ti based biomaterials, the ultimate choice for orthopaedic implants — a review, Prog. Mater. Sci. 54 (2009) 397—425.

[2] M.A. Hussein, C. Suryanarayana, N. Al-Aqeeli, Fabrication of nano-grained Ti—Nb—Zr biomaterials using spark plasma sintering, Mater. Des. 87 (2015) 693—700.

[3] M. Popa, E. Vasilescu, P. Drob, D. Raducanu, J.M. Calderon Moreno, S. Ivanescu, C. Vasilescu, S.I. Drob, Microstructure, mechanical, and anticorrosive properties of a new Ti-20Nb-10Zr-5Ta alloy based on nontoxic and nonallergenic elements, Met. Mater. Int. 18 (2012) 639—645.

[4] Y. He, Y. Zhang, Z. Meng, Y. Jiang, R. Zhou, Microstructure evolution, mechanical properties and enhanced bioactivity of Ti-Nb-Zr based biocomposite by bioactive calcium pyrophosphate, J. Alloys Compd. 720 (2017) 567—581.

[5] E. Kobayashi, H. Doi, M. Takahashi, T. Nakano, T. Yoneyama, H. Hamanaka, Castability and mechanical properties of Ti—6Al—7Nb alloy dental-cast, J. Jpn. Soc. Dent. Mater. Devices 14 (1995) 406—413.

[6] H. Doi, T. Yoneyama, E. Kobayashi, H. Hamanaka, Mechanical properties and corrosion resistance of Ti—5Al—13Ta alloy castings, J. Jpn. Soc. Dent. Mater. Devices 17 (1998) 247—252.

[7] T.M. Mohsin, A.K. Zahid, N.S. Arshad, Beta titanium alloys: the lowest elastic modulus for biomedical applications: a review, Int. J. Chem. Mol. Nucl. Mater. Metall. Eng. 8 (2014) 726—731.

[8] X. Wang, L. Zhang, Z. Guo, Y. Jiang, X. Tao, L. Liu, Study of low-modulus biomedical β Ti—Nb—Zr alloys based on single-crystal elastic constants modeling, J. Mech. Behav. Biomed. Mater. 62 (2016) 310—318.

[9] S.E. Kim, H.W. Jeong, Y.T. Hyun, Y.T. Lee, C.H. Jung, S.K. Kim, J.S. Song, J.H. Lee, Elastic modulus and in vitro biocompatibility of Ti-xNb and Ti-xTa alloys, Met. Mater. Int. 13 (2007) 145—149.

[10] R. Karre, M.K. Niranjan, S.R. Dey, First principles theoretical investigations of low Young's modulus beta Ti—Nb and Ti—Nb—Zr alloys compositions for biomedical applications, Mater. Sci. Eng. C 50 (2015) 52—58.

[11] L.A. Dragan-Raileanu, C.E. Cotrutz, C. Munteanu, S. Strugaru, P. Avram, B. Istrate, T. Petreus, In vitro study regarding the cytotoxicity of some TiNbZr alloys, Ann. Rom. Soc. Cell Biol. 18 (2013) 186—191.

[12] D.G. Lee, Y.T. Lee, X. Mi, W. Ye, S. Hui, Beta-based Titanium Alloy with Low Elastic Modulus, US20140112820A1, 2014.

[13] D.G. Lee, Y.T. Lee, X. Mi, W. Ye, S. Hui, Beta-based Titanium Alloy with Low Elastic Modulus, US20110070121A1, 2011.

[14] M.W.D. Mendes, C.G. Ágreda, A.H.A. Bressiani, J.C. Bressiani, A new titanium based alloy Ti—27Nb—13Zr produced by powder metallurgy with biomimetic coating for use as a biomaterial, Mater. Sci. Eng. C 63 (2016) 671—677.

[15] C. Suryanarayana, Mechanical alloying and milling, Prog. Mater. Sci. 46 (2001) 1—184.

[16] T.J. Webster, J.U. Ejiofor, Increased osteoblast adhesion on nanophase metals: Ti, Ti6Al4V, and CoCrMo, Biomater 25 (2004) 4731—4739.

[17] B.C. Ward, T.J. Webster, Increased functions of osteoblasts on nanophase metals, Mater. Sci. Eng. C 27 (2007) 575—578.

[18] M. Kaczmarek, M.U. Jurczyk, B. Rubis, A. Banaszak, A. Kolecka, A. Paszel, K. Jurczyk, M. Murias, J. Sikora, M. Jurczyk, In vitro biocompatibility of Ti-45S5 Bioglass nanocomposites and their scaffolds, J. Biomed. Mater. Res. Part A 102 (2014) 1316—1324.

[19] A. Miklaszewski, M.U. Jurczyk, M. Kaczmarek, A. Paszel-Jaworska, A. Romaniuk, N. Lipińska, J. Żurawski, P. Urbaniak, M. Jurczyk, Nanoscale size effect in in situ titanium based composites with cell viability and cyto-compatibility studies, Mater. Sci. Eng. C 73 (2017) 525—536.

[20] K. Jurczyk, M. Jurczyk, Applications of nanomaterials in dentistry, in: R. Bawa, G.F. Audette, I. Rubinstein (Eds.), Handbook of Clinical Nanomedicine: Nano-particles, Imaging, Therapy, and Clinical Applications, Pan Stanford Publishing Pte. Ltd., New York, 2015, pp. 1073—1108.

[21] K. Jurczyk, A. Miklaszewski, M.U. Jurczyk, M. Jurczyk, Development of β type Ti23Mo-45S5 Bioglass nanocomposites for dental applications, Mater 8 (2015) 8032—8046.

[22] R.Z. Valiev, I.P. Semenova, V.V. Latysh, A.V. Shcherbakov, E.B. Yakushina, Nanostructured titanium for biomedical applications: new developments and challenges for commercialization, Nanotechnol. Russ. 3 (2008) 593—601.

[23] A. Robin, O.A.S. Carvalho, Influence of pH and fluoride species on the corrosion behavior of TixNb-13Zr alloys in Ringer's solution, Adv. Mater. Sci. Eng. 2013 (2013) 434975.

[24] J.R. Woodard, A.J. Hilldore, S.K. Lan, C.J. Park, A.W. Morgan, J.A. Eurell, S.G. Clark, M.B. Wheeler, R.D. Jamison, A.J. Wagoner Johnson, The mechanical properties and osteoconductivity of hydroxyapatite bone scaffolds with multi-scale porosity, Biomaterials 28 1 (2007) 45—54.

[25] J. Cesarano, J.N. Stuecker, J.G. Dellinger, R.D. Jamison, Method for Making a Bio-compatible Scaffold, US6993406B1, 2006.

[26] G. Dercz, I. Matuła, M. Zubko, J. Dercz, Phase composition and microstructure of new Ti-Ta-Nb-Zr biomedical alloys prepared by mechanical alloying method, Powder Diffr. 32 (2017) 186—192.

[27] C.A. Charitidis, P. Georgiou, M.A. Koklioti, A.-F. Trompeta, V. Markakis, Manufacturing nanomaterials: from research to industry, Manuf. Rev. 1 (2014) 11.

[28] B. O'Brien, J. Stinson, W. Carroll, Development of a new niobium-based alloy for vascular stent applications, J. Mech. Behav. Biomed. Mater. 1 (2008) 303—312.

[29] S.Y. Yu, J.R. Scully, Corrosion and passivity of Ti-13% Nb-13% Zr in comparison to other biomedical implant alloys, Corrosion 53 (1997) 965—976.

[30] J.I. Kim, H.Y. Kim, T. Inamura, H. Hosoda, S. Miyazaki, Shape memory char-acteristics of Ti—22Nb—(2—8)Zr(at.%) biomedical alloys, Mater. Sci. Eng. A 403 (2005) 334—339.

Artykuł nr 2:

M. Marczewski, A. Miklaszewski, X. Maeder,

M. Jurczyk, **Crystal Structure Evolution,**

Microstructure Formation, and Properties of

Mechanically Alloyed Ultrafine-Grained Ti-Zr-Nb

Alloys at 36 ≤ Ti ≤ 70 (at. %)

Crystal Structure Evolution, Microstructure Formation, and Properties of Mechanically Alloyed Ultrafine-Grained Ti-Zr-Nb Alloys at 36 ≤ Ti ≤ 70 (at. %)

Mateusz Marczewski [1,*], **Andrzej Miklaszewski [1]**, **Xavier Maeder [2]** and **Mieczyslaw Jurczyk [1]**

[1]   Institute of Materials Science and Engineering, Poznan University of Technology, Jana Pawla II No 24, 61-138 Poznan, Poland; andrzej.miklaszewski@put.poznan.pl (A.M.); mieczyslaw.jurczyk@put.poznan.pl (M.J.)

[2]   Laboratory of Mechanics of Materials and Nanostructures, Empa, Swiss Federal Laboratories for Materials Science and Technology, Feuerwerkerstrasse 39, CH-3602 Thun, Switzerland; xavier.maeder@empa.ch

*   Correspondence: mateusz.p.marczewski@doctorate.put.poznan.pl; Tel.: +48-61-665-3508

Abstract: Titanium β-type alloys are preferred biomaterials for hard tissue replacements due to the low Young modulus and limitation of harmful aluminum and vanadium present in the commercially available Ti6Al4V alloy. The aim of this study was to develop a new ternary Ti-Zr-Nb system at 36 ≤ Ti ≤ 70 (at. %). The technical viability of preparing Ti-Zr-Nb alloys by high-energy ball-milling in a SPEX 8000 mill has been studied. These materials were prepared by the combination of mechanical alloying and powder metallurgy approach with cold powder compaction and sintering. Changes in the crystal structure as a function of the milling time were investigated using X-ray diffraction. Our study has shown that mechanical alloying supported by cold pressing and sintering at the temperature below α→β transus (600 °C) can be applied to synthesize single-phase, ultrafine-grained, bulk Ti(β)-type Ti30Zr17Nb, Ti23Zr25Nb, Ti30Zr26Nb, Ti22Zr34Nb, and Ti30Zr34Nb alloys. Alloys with lower content of Zr and Nb need higher sintering temperatures to have them fully recrystallized. The properties of developed materials are also engrossing in terms of their biomedical use with Young modulus significantly lower than that of pure titanium.

Keywords: metals and alloys; mechanical alloying; X-ray diffraction; phase transition; powder metallurgy

1. Introduction

Titanium appears in two different allotropic forms. At low temperatures, it has a closed packed hexagonal crystal structure (space group: P63/mmc–hcp), which is known as α, whereas above 882 ± 2 °C, it has a body-centered cubic structure (space group: Im-3m – bcc) termed β. The alloying elements, such as N, O, and Al, tend to stabilize the α phase, whereas elements V, Cr, Nb, and Mo stabilize the β phase [1–4]. Pure titanium and Ti-6Al-4V alloy are the main materials in the medical field. A component such as vanadium is described to be cytotoxic. The release of its ions to the human body system during implant wear can lead to neurodegenerative diseases such as Alzheimer's disease. Furthermore, some of the researches also revealed the severe danger of the DNA damage caused by the Ti-6Al-4V alloy [5–7]. Vanadium ions were also proven to be toxic to the fibroblasts causing the significant limitation of their viability [8]; therefore, preparation of Ti alloys without these additives should be the prior goal of most researches. One of the possibilities is to produce β-type titanium

alloys with low toxicity and high biocompatibility as Ti-Zr-Nb alloys. To stabilize Ti(β) it is necessary to form the alloys based on the following elements [9].

(a) Binary alloys: Ti-Nb, Ti-Mo, Ti-Ta, Ti-Zr, Ti-Mn, Ti–Cr.

(b) Ternary alloys: Ti-Nb-Mo, Ti-Nb-Pd, Ti-Nb-Zr, Ti-Nb-Sn, Ti-Nb-Ta, Ti-Nb-Fe, Ti-Mo-Zr, Ti-Mo-Nb, Ti-Cr-Al, Ti–Cr–Nb, Ti-Cr-Sn, Ti–Mn–Al, Ti-Ta-Nb, Ti-Ta-Sn, Ti-Ta-Zr, Ti–Mn–Fe, Ti–Sn–Cr.

(c) Quaternary alloys: Ti-Ta-Sn-Zr, Ti-Nb-Zr-Sn, Ti-Nb-Zr-Fe, Ti-Nb-Ta-Zr, Ti-Mo-Zr-Fe, Ti-Fe-Ta-Zr, Ti-Cr-Mn-Sn.

Two of the elements stabilizing Ti(β) are niobium and zirconium. Both have been proven to have higher biocompatibility than aluminum and vanadium. The biocompatibility of niobium was also concerned to be higher than titanium [10]. Ti-Zr [11–15] and Ti-Nb systems [16–21] were already examined in several articles. It was reported that Ti-Zr alloys can improve biocompatibility properties of pure titanium, their mechanical strength and grind ability [13,14]. Additionally, it can be observed that the content of Zr in the binary Ti-Zr alloys cannot provide Ti(β) formation at room temperature. Zr allows only to decrease the temperature of Ti(α)-Ti(β) phase transition to 806 °C [11,12]. On the other hand, Ti-Nb alloys allow improving the mechanical properties of titanium. Niobium increases the hardness of the alloy and decreases the compression modulus. Content of niobium influenced also compression strength and wear resistance [17]. Niobium forms also isomorphous phase with titanium providing good Ti(β) stabilizing effect and appearance of this phase at room temperature. Ti-Nb alloys can form double Ti(α) + Ti(β) phases and single Ti(β), Nb phases [21]. The matter of great importance is that crystal structure influences Young's modulus which is lower with the addition of β-stabilizers. It was observed that Ti(β) alloys and near Ti(β) alloys can be characterized by the lower elastic modulus, even multiple times lower than commercially pure titanium (especially for alloys with niobium and zirconium content) [3,22]. It limits the possibility of mechanical unfit and loosening of the implant (so-called stress shielding effect) [1,2].

The Ti-Nb-Zr alloys need to be well treated after alloying to provide the correct structure. The properties of the β-type alloys are susceptible to heat and mechanical treatment. Ti-39Nb after repeated several times cold rolling and heat treatment had the single β structure with low Young modulus equals to 39 GPa. This is mainly because of the high density of the defects as dislocations and grain boundaries [23]. The properties of casted Ti–15Zr–5Cr–2Al alloys were also drastically changed after water quenching [24]. Titanium alloys in Ti-Nb-Zr system could be used as the coating. It is provided that this type of modification will improve the surface properties of the alloy. Moreover, depending on the type and the parameters of the process it is possible to control the properties and the microstructure of the manufactured implant layer [25]. To develop biomaterials properties the use of mechanical alloying (MA) should be considered [26]. Phase equilibria in the Ti-Nb-Zr system with the powders produced by this technology has not been investigated so far. However, these tests are relevant to determine the influence of the process parameters on the crystal structure of these materials. Recently, other β-type materials were tested as Ti-Fe-Zr alloys [27] and the properties of the Ti-Nb-Zr alloys were introduced only in two different chemical compositions: Ti14Zr16Nb and Ti23Zr25Nb [28]. Many β-type titanium alloys are still under investigation as selective laser melted metastable Ti–37Nb–6Sn [29], laser powder bed fused Ti-18Zr-14Nb [30] with nano α-phase precipitates, vacuum arc melted Ti-32Nb-(2, 4) Sn with nano α-phase precipitates [31], mechanically alloyed Ti-Mo alloys [32]. Low Young modulus alloys are not mentioned to be only the titanium-based alloys. Mechanical properties of materials as Zr-12Nb-4Sn seems to be also interesting [33].

Nowadays, the majority of Ti-Nb-Zr alloys are produced by traditional methods as vacuum arc remelting (VAR) [34,35]. Mechanical alloying allows us to form the nonequilibrium structures (nanocrystalline, ultrafine grain structure, etc.) influencing the improvement of some properties. The process can be controlled by the following parameters: time of milling, the ball to powder mass ratio, type of the mill, milling speed, etc [26,36]. Ti-Nb-Zr alloys have been produced by mechanical alloying but the influence of Nb and Zr on the crystal structure has not been examined [27]. The hardness of Ti13Zr20Nb (at. %) has been estimated as 660 HV, which is higher than the hardness of traditional

alloys [37,38]. Recently Bai et al. investigated the diffusion behaviors of Zr and Nb in β-Ti alloys and developed an atomic mobility date base for the bcc phase in the Ti-Zr-Nb system using the LALPHAD method [39]. Additionally, the properties of ternary Ti-Nb-Zr alloys with porous structures synthesized by a magnetron sputtering method was studied [40]. It was shown that the porous structure was also dependent on the alloy composition. The Young's modulus of ternary thin films was in the range of 80 to 95 GPa.

The aim of the current study was the synthesis of ultrafine-grained Ti-Zr-Nb alloys at $36 \leq$ Ti ≤ 70 (at. %) by mechanical alloying and powder metallurgy methods. Proposed in this work broad stabilizing elements composition was chosen to include both dual-phase and single-phase Ti-Zr-Nb alloys structure evolution as also its microstructure formation and properties comparison studies. The influence of Zr and Nb contents with a heat treatment temperature on phase transitions of Ti(α) to Ti(β), with a microstructure examination, were studied. Yet to the authors' knowledge, there have been no papers regarding the addition of Zr and Nb to Ti-based alloys in very wide concentrations to have appeared until now.

2. Materials and Methods

2.1. Chemicals and materials

The following powders were used to produce the materials: the commercial Ti (Alfa Aesar, Haverhill, MA, USA, 99.9% purity, CAS:7440-32-6), Nb (Sigma Aldrich, St. Louis, MO, USA, 99.8% purity, CAS:7446-03-1) powders and Zr fillings from a sponge (Sigma Aldrich, $\geq$ 99%, CAS:7440-67-7). The experiments were carried out on 9 different Ti-Zr-Nb type alloys (Table 1). The experiments were arranged at three stages: (1) Ti-Zr-Nb (Nb: 16-34 at. %; Zr: 14-30 at. %) powders preparation by mechanical alloying for 10 h, (2) sample consolidation by cold pressing and sintering at the temperature range of 600 to 1000 °C, and (3) materials characterization (phase structure analysis with X-ray diffraction, wettability, and surface free energy, corrosion resistance, hardness, and nanoindentation, EDS and EBSD).

Table 1. Chemical compositions of output powders needed to get following Ti-Nb-Zr alloys after all stages of specimen preparation by the application of SPEX 8000 Mixer Mill (total weight of milling powders: 4.5 g; ball-to-powder mass ratio: 7.5:1; milling time: 10 h).

Alloy	Ti wt %	Zr wt %	Nb wt %
Ti14Zr16Nb (at. %)	66	17	17
Ti23Zr16Nb (at. %)	57	26	17
Ti30Zr17Nb (at. %)	50	33	17
Ti14Zr25Nb (at. %)	57	17	26
Ti23Zr25Nb (at. %)	48	26	26
Ti30Zr26Nb (at. %)	41	33	26
Ti13Zr33Nb (at. %)	50	17	33
Ti22Zr34Nb (at. %)	41	26	33
Ti30Zr34Nb (at. %)	34	33	33

2.2. Specimen Preparation

SPEX 8000 Mixer Mill (SPEX® Sample Prep, Metuchen, NJ, USA) and round-bottom stainless vials were used for the mechanical alloying process in an argon atmosphere. Glove box (LabMaster 130) filled with argon atmosphere ($O_2 <$ 2 ppm and H_2O < 1 ppm) was used to weigh, blend, and pour (into vials) the elemental powders (Ti, Nb, and Zr). MA process was lasted up to 10 h in all cases. All the powders turned into bulk specimens of 6 mm diameter and 4 mm height. The pressure of 600 MPa was used for cold compaction to consolidate the powders. The specimens were next sealed in a quartz tube filled with an argon atmosphere. Specimens were sintered in five temperatures: 600, 750, 800, 850, and 1000 °C

within a 30 min heating being sealed in a quartz tube filled with an argon atmosphere. Specimens were fast cooled in water.

2.3. Materials Characterization

Panalytical Empyrean XRD equipment with Cu Kα radiation (Almelo, Netherlands) was used to evaluate the structure of the specimens at room temperature during different processing stages. XRD measurements was done as follows; voltage 45 kV, anode current 40 mA, 2 theta range 30 – 80[°], time per step 60.325 [s/step], and step size 0.0334[°]. Background, profile coefficients, lattice parameters, linear absorption coefficients, and other variables were refined to obtain the spectra. Crystallite size and lattice strain of mechanically alloyed powders were estimated by the Williamson–Hall (W–H) analysis method [41] with the use of the uniform deformation model (UDM) [41] linearly fitting points assigned to the different diffraction lines. Rietveld analysis [42] was done to estimate the lattice parameters and phase quantity by Maud software. The following analyzed structural models were used in this approach: Ti(α) (ref. code 01-071-4632), Ti(β) ref. code 01-074-7075), Nb0.81Zr0.19 (ref. code 00-049-1455), Zr (ref. code 01-088-2329), and NbZr (ref. code 01-071-9970). The calculated pattern of the model structure was fitted by minimization of the sum of the squares and using Marquardt least-squares algorithm [43]. High goodness of fit ($\chi2<3$) was achieved. Pattern fitting parameters: Rwp—weighted pattern residual indicator; Rexp—expected the residual indicator: S—the goodness of fit were revealed.

The chemical composition was examined by the scanning electron microscope (SEM, VEGA 5135, Tescan, Brno, Czech Republic) with the energy dispersive spectrometer (EDS, PTG Prison Avalon, Princeton Gamma Tech., Princeton, NY, USA) calibrated by a typical Cu calibration procedure. The parameters of the measurement are as follows; accelerating voltage: 20 kV; working distance: 23 mm; spot size: 160 nm. The microstructure of the alloys was characterized by electron backscatter diffraction (EBSD), using a Tescan Mira microscope (Brno, Czech Republic) and Digiview V camera from EDAX (Mahwah, NJ, USA). The crystal orientation maps were acquired using electron beam conditions of 20 kV and 10 nA, with 100 nm step size. The minimum misorientation angle for the grain calculation was 5° and with a minimum of 8 pixels, discarding the grain smaller than 300 nm in diameter. No cleaning procedure was applied to the maps. The contact angle (CA) of the surfaces was recorded by the optical system with a digital camera (Kruss-DSA25, Krüss, Hamburg, Germany) and measured by dedicated software (Kruss-Advanced 1.5, Krüss, Hamburg, Germany). The specimens were polished with Al_2O_3 suspension, flushed with alcohol, and dried before the measurement. Determination of contact angles for diiodomethane and glycerol was done with the ellipse fitting method [44] and 2 μL drop. Surface free energies were calculated based on the results for both fluids. The experiments were repeated three times for each specimen to determine the uncertainty and standard deviation for each measurement and all at ambient conditions (23 °C). For the specimen corrosion resistance analysis in the Ringer's solution (NaCl: 9 g/L, KCl: 0.42 g/L, CaCl2: 0.48 g/L, NaHCO3: 0.2 g/L) at ambient conditions (23 °C). the potentiodynamic method was used. The experiments and analysis were conducted on Solartron 1285 potentiostat (Solartron Analytical, Farnborough, UK) with dedicated Corrware and Corrview software (Solartron Analytical, Farnborough, UK). Ag/AgCl electrode was used as a reference electrode in the measurements. The corrosion potential and current were calculated with Tafel curves. The specimens were polished with grinding paper 600 grit and clean with ethanol inside the ultrasonic bath before each measurement before starting. Potentiodynamic tests were preceded with open circuit potential measurement for 60 min. Every specimen was measured three times to estimate uncertainties and standard deviation.

Vickers microhardness (HV) of the sinters was measured using an Innovatest Nexus microhardness tester (Innovatest, Maastricht, Netherlands) with an applied load of 300 g and loading time 10 s. The modulus analysis of selected specimens based on the EIT (indentation modulus) estimation, was realized on Fischerscope HM2000 nanoindenter with Vickers tip located in Bern University of Applied Sciences (Biel, Switzerland). The measurement was carried out with nanoindenter using DIN

50 359/ISO 14577 standard, and load parameters of the test as: F (the max load with the loading time) = 300 mN/20s, C (creep time at the max load) = 5 s.

3. Results

Synthesis of ultrafine-grained Ti-Zr-Nb alloys by mechanical alloying and powder metallurgy method was the goal of this research, see Table 1. Crystal structure and its changes during milling were deeply examined. Diffractograms of the selected Ti-Zr-Nb alloy powders with the final single phase beta-structure (Ti23Zr25Nb) and dual-phase alpha + beta structure (Ti14Zr16Nb) milled for different times were presented in our previous article [28]. After 15 min of milling, the positions of the 2θ peaks of Ti-Zr-Nb mixtures are the same as that of the elemental powders, indicating that no significant reaction had occurred during milling. The hexagonal Zr (101) plane is barely visible after 3 h of milling. Moreover, 6 h of mechanical alloying leads to the formation of Ti(β) for all produced compositions. Zr content influences the angle position of the newly formed Ti(β) phase peaks moving them to the higher values. (Figures 1 and 2). It can be seen that after 10 h of MA of Ti14Zr16Nb and Ti23Zr16Nb there are peaks of Ti(α) and Ti(β). Additionally, in the case of Ti30Zr17Nb, Ti14Zr25Nb, Ti23Zr25Nb, Ti30Zr26Nb, Ti13Zr33Nb, Ti22Zr34Nb, and Ti30Zr34Nb mixtures all three peaks emerge. These peaks mark to coincide with the peaks of Ti(β) phase suggesting that these mixtures could be of a bcc structure induced by deformation during the mechanical alloying.
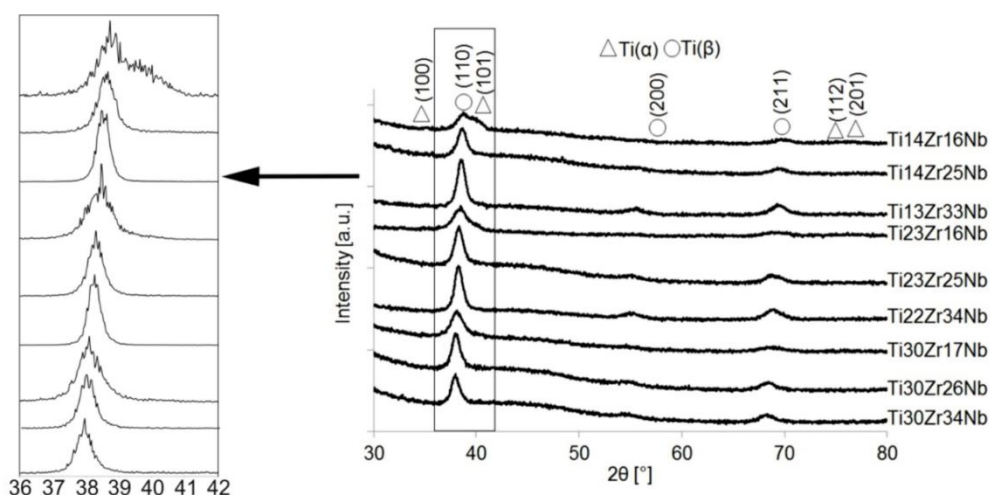

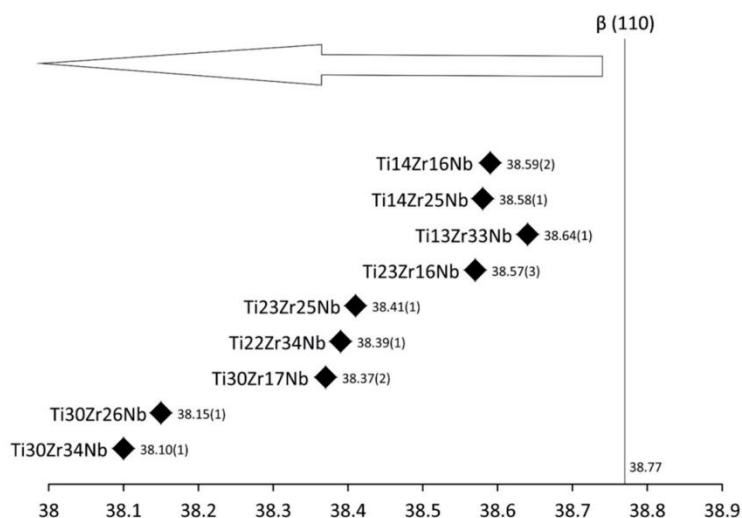**Figure 1.** X-ray diffraction (XRD) spectra of Ti-Zr-Nb powders mechanically alloyed for 10 h.
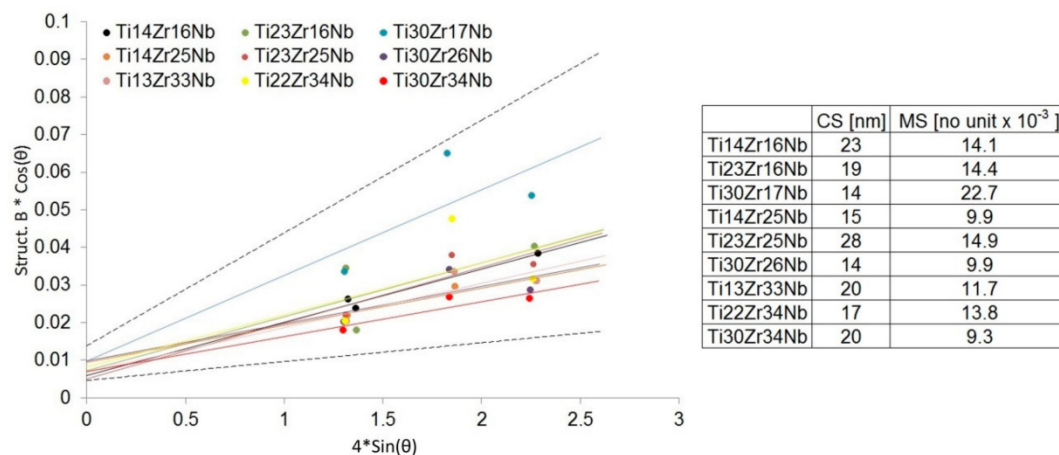

Figure 2. New phase Ti(β) 2 theta locations of studied alloys after 6 h of MA.

Mechanical alloying was described as a high energy milling process in which powder particles were subjected to repeated cold welding, fracturing, and rewilding [26]. The high plastic deformations of the powders result in a high density of dislocations and, subsequently, subgrains formation that may finally lead also to desired phase Ti(β) formation [45]. Our studies have shown that the mechanical alloying of mixtures of Ti, Zr, and Nb metal powders produces the crystal phases depending on the milling conditions and starting composition. No amorphous phases have also been observed in milled powder mixtures. Mechanical alloying allows inducing allotropic transformation of titanium (from hexagonal α to cubic β). Both the content of beta-stabilizers (Zr and Nb) and time help to control this transformation. Based on the Williamson–Hall model [41] after 10 h of milling crystallite size was estimated in the range of 14 to 28 nm. Moreover, the application of mechanical alloying increases the microstrains in the produced alloys (on average $9 - 23 \times 10^{-3}$) – Figure 3. Proper choice of the process parameters and alloy composition allows producing crystalline Ti(β) phase.

	CS [nm]	MS [no unit x 10^{-3}]
Ti14Zr16Nb	23	14.1
Ti23Zr16Nb	19	14.4
Ti30Zr17Nb	14	22.7
Ti14Zr25Nb	15	9.9
Ti23Zr25Nb	28	14.9
Ti30Zr26Nb	14	9.9
Ti13Zr33Nb	20	11.7
Ti22Zr34Nb	17	13.8
Ti30Zr34Nb	20	9.3

Figure 3. Linear Williamson–Hall plots with estimated crystallite size (CS) and microstrain (MS) factors based on the XRD spectra of Ti-Zr-Nb powder materials after 10 h of mechanical alloying.

To produce bulk specimens of mechanically alloyed powder: cold pressing and sintering were conducted. Heating was done for 0.5 h and at five different temperatures: 600, 750, 800, 850 and 1000 °C. The process was conducted at the argon atmosphere to prevent the materials from oxidation. The diffractograms of alloys sintered at the same temperature of 750 °C were presented in Figure 4. The diffractogram relations of two selected specimens with single-phase beta structure (Ti23Zr25Nb) and dual-phase alpha+beta structure (Ti14Zr16Nb) with the sintering temperature were presented in our previous article [28]. Additionally, lattice constants and phase amounts relations based on a composition and processing parameters of the materials were presented in Table 2. After consolidation, two groups of produced materials can be distinguished:

(a) Ti14Zr16Nb, Ti23Zr16Nb, Ti14Zr25Nb, and Ti13Zr33Nb alloys with visible traces of Ti(α) (ref. code 01-071-4632), and Nb0.81Zr0.19 (ref. code 00-049-1455),

(b) Ti30Zr17Nb, Ti23Zr25Nb, Ti30Zr26Nb, Ti22Zr34Nb, and Ti30Zr34Nb alloys with visible traces of Zr (ref. code 01-088-2329), NbZr (ref. code 01-071-9970), and Nb0.81Zr0.19.

Single beta alloys were produced at some specific sintering conditions which confirm the high influence of consolidation parameters on the crystal structure of the materials. Ti23Zr25Nb and Ti30Zr26Nb alloys needed the sintering temperature in the range of 600 to 800 °C, Ti22Zr34Nb and Ti30Zr34Nb in the range of 600 to 750 °C and Ti30Zr17Nb—600 °C. In higher temperatures, pure Zr was present in the structure of alloys. It was observed in almost all materials except these with the smallest concentration of Zr: Ti14Zr16Nb, Ti14Zr25Nb, and Ti13Zr33Nb. This phase appears mainly in the temperatures above 850 °C. The increasing concentration of Ti(β) phase could be easily connected with the increase of the sintering temperature. All alloys, except Ti14Zr16Nb with the lowest content of beta-stabilizers, have the pseudo-beta structure with Ti(β) phase content above 97%.

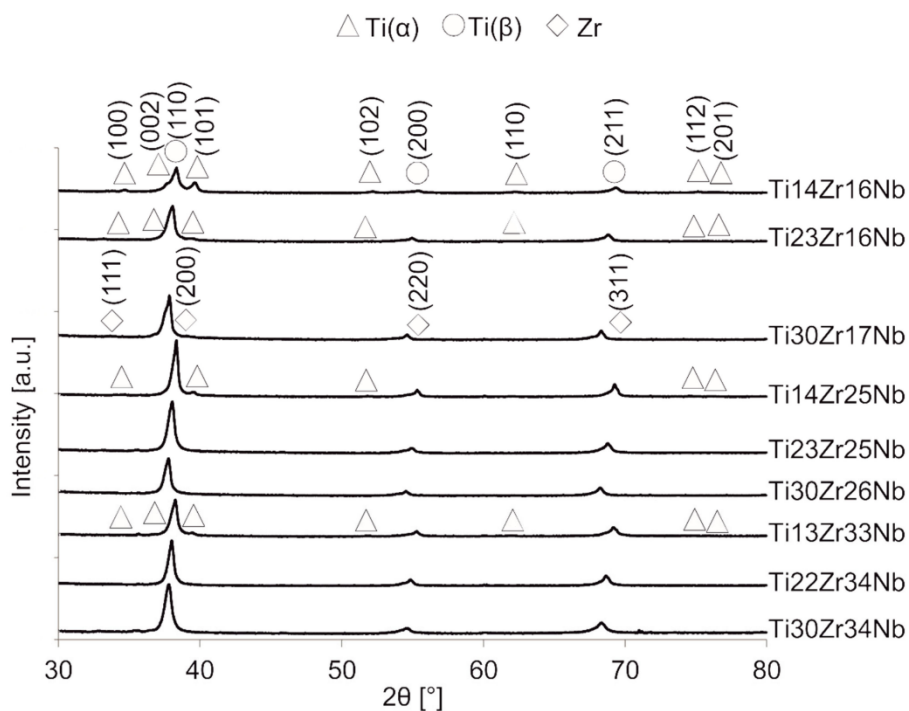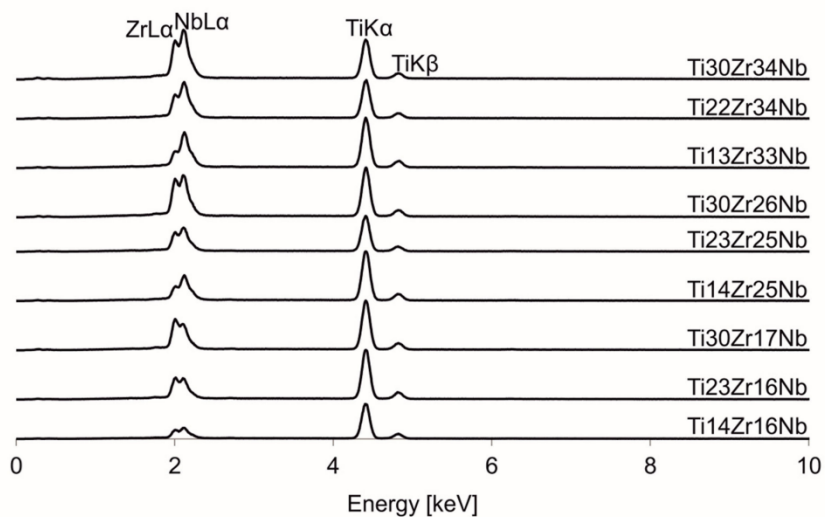The chemical compositions of alloys were confirmed with EDS. All the spectra and results were presented in Figure 5.

Figure 4. XRD spectra of bulk Ti-Zr-Nb specimens sintered at 750 °C.

Material	Ti		Zr		Nb	
	Wt [%]	At [%]	Wt [%]	At [%]	Wt [%]	At [%]
Ti14Zr16Nb	54.12±1.00	69.40±0.85	21.46±0.38	14.45±0.19	24.42±1.35	16.15±1.00
Ti23Zr16Nb	44.48±0.42	60.59±0.41	32.06±0.94	22.93±0.73	23.46±0.53	16.48±0.34
Ti30Zr17Nb	37.49±0.23	53.49±0.24	39.86±0.33	29.86±0.29	22.65±0.22	16.66±0.16
Ti14Zr25Nb	44.95±0.35	61.15±0.33	18.96±0.26	13.54±0.17	36.08±0.54	25.31±0.43
Ti23Zr25Nb	35.52±0.35	51.44±0.38	30.70±0.29	23.35±0.24	33.78±0.40	25.22±0.34
Ti30Zr26Nb	29.17±0.29	44.17±0.34	37.02±0.45	29.44±0.29	33.80±0.73	26.39±0.62
Ti13Zr33Nb	37.74±0.42	53.90±0.44	18.01±0.17	13.50±0.17	44.25±0.28	32.59±0.29
Ti22Zr34Nb	29.01±0.32	44.04±0.38	28.15±0.33	22.43±0.21	42.83±0.64	33.52±0.58
Ti30Zr34Nb	22.73±0.22	36.13±0.28	35.66±0.55	29.76±0.45	41.62±0.67	34.11±0.59

Figure 5. Energy-dispersive spectroscopy (EDS) spectra of Ti-Zr-Nb alloys.

Table 2. Crystallographic data analysis of bulk Ti-Zr-Nb specimens sintered at different conditions.

Specimen	PT [°C]	Ti(α) a [Å]	c [Å]	V [Å³]	PA [%]	Ti(β) a [Å]	V [Å³]	PA [%]	Additional Phase Nb0.81Zr0.19 a [Å]	V [Å³]	PA[%]	R$_{wp}$ [%]	R$_{exp}$ [%]	S
Ti14Zr16Nb	600	2.9862(4)	4.7566(14)	36.73(2)	44.83	3.3218(3)	36.65(1)	55.17	-	-	-	4.86	3.35	1.45
	750	2.9853(4)	4.7761(15)	36.86(3)	26.54	3.3255(3)	36.78(1)	73.46	-	-	-	5.67	3.20	1.77
	800	2.9908(5)	4.7843(19)	37.06(3)	26.20	3.3313(3)	36.97(1)	73.80	-	-	-	6.28	3.65	1.72
	850	2.9903(11)	4.7817(41)	37.03(6)	9.94	3.3327(2)	37.02(1)	88.64	4.3477(25)	82.18(14)	1.42	7.35	3.39	2.17
	1000	2.9972(16)	4.7798(63)	37.18(9)	2.69	3.3357(2)	37.12(1)	96.02	4.3214(14)	80.70(8)	1.29	6.58	3.04	2.17
								Zr						
Ti23Zr16Nb	600	2.9966(8)	4.7892(33)	37.24(5)	24.90	3.3494(2)	37.57(1)	75.10	-	-	-	5.47	2.99	1.83
	750	2.9982(34)	4.8054(156)	37.41(21)	7.87	3.3510(2)	37.63(1)	92.13	-	-	-	6.58	3.03	2.17
	800	3.0246(41)	4.7830(196)	37.89(26)	9.65	3.3527(2)	37.68(1)	90.35	-	-	-	6.42	2.91	2.21
	850	-	-	-	-	3.3509(2)	37.63(1)	99.19	4.6102(17)	97.98(11)	0.81	5.01	2.95	1.70
	1000	-	-	-	-	3.3532(2)	37.70(1)	98.98	4.6051(14)	97.66(9)	1.02	6.33	2.89	2.19
								Zr						
Ti30Zr17Nb	600	-	-	-	-	3.3610(2)	37.97(1)	100	-	-	-	6.74	2.72	2.48
	750	-	-	-	-	3.3699(2)	38.27(1)	99.66	4.6157(29)	98.33(18)	0.34	6.73	2.84	2.37
	800	-	-	-	-	3.3688(2)	38.23(1)	98.71	4.6050(23)	97.66(15)	1.29	6.89	2.89	2.39
	850	-	-	-	-	3.3628(2)	38.03(1)	99.53	4.6054(22)	97.68(14)	0.47	6.62	2.77	2.39
	1000	-	-	-	-	3.3671(2)	38.17(1)	99.27	4.6092(13)	97.92(9)	0.73	7.79	2.65	2.94
								Zr						
Ti14Zr25Nb	600	2.9826(7)	4.7679(27)	36.73(4)	14.05	3.3232(2)	36.70(1)	85.95	-	-	-	5.50	2.99	1.84
	750	2.9949(13)	4.7679(55)	37.04(8)	6.98	3.3261(2)	36.79(1)	93.02	-	-	-	6.55	2.82	2.32
	800	2.9993(15)	4.7671(65)	37.14(9)	7.24	3.3280(2)	36.86(1)	92.76	-	-	-	6.35	2.97	2.14
	850	2.9992(22)	4.7653(87)	37.12(12)	4.68	3.3278(2)	36.85(1)	95.32	-	-	-	7.35	2.95	2.49
	1000	3.0091(43)	4.7939(183)	37.59(25)	3.23	3.3359(2)	37.12(1)	96.77	-	-	-	6.21	3.05	2.03

Table 2. *Cont.*

Specimen	PT [°C]	Ti(α)				Ti(β)			Additional Phase Nb0.81Zr0.19			R$_{wp}$ [%]	R$_{exp}$ [%]	S
		a [Å]	c [Å]	V [Å³]	PA [%]	a [Å]	V [Å³]	PA [%]	a [Å]	V [Å³]	PA[%]			
									Zr					
Ti23Zr25Nb	600	-	-	-	-	3.3440(1)	37.39(1)	100	-	-	-	4.86	2.67	1.82
	750	-	-	-	-	3.3495(2)	37.58(1)	100	-	-	-	5.19	2.60	2.00
	800	-	-	-	-	3.3524(2)	37.68(1)	100	-	-	-	5.05	3.08	1.64
	850	-	-	-	-	3.3500(2)	37.60(1)	99.50	4.6035(30)	97.56(19)	0.50	5.46	2.97	1.84
	1000	-	-	-	-	3.3500(2)	37.60(1)	99.07	4.6077(25)	97.83(16)	0.93	6.76	2.74	2.46
									Zr					
Ti30Zr26Nb	600	-	-	-	-	3.3694(2)	38.25(1)	100	-	-	-	5.61	3.23	1.74
	750	-	-	-	-	3.3720(2)	38.34(1)	100	-	-	-	5.36	3.02	1.77
	800	-	-	-	-	3.3753(2)	38.45(1)	100	-	-	-	6.20	2.62	2.37
	850	-	-	-	-	3.3720(2)	38.34(1)	99.35	4.6199(16)	98.60(10)	0.65	5.82	2.93	1.99
	1000	-	-	-	-	3.3770(2)	38.51(1)	98.66	4.6188(12)	98.53(8)	1.34	6.53	2.64	2.48
									Nb0.81Zr0.19					
Ti13Zr33Nb	600	2.9880(15)	4.7643(68)	36.84(9)	6.88	3.3242(2)	36.73(1)	93.12	-	-	-	5.09	3.04	1.67
	750	3.0022(14)	4.7679(56)	37.22(8)	5.60	3.3314(2)	36.97(1)	94.40	-	-	-	5.38	2.95	1.82
	800	3.0033(22)	4.7591(98)	37.18(13)	4.82	3.3271(2)	36.83(1)	95.18	-	-	-	5.82	2.76	2.11
	850	3.0103(16)	4.7667(73)	37.41(10)	6.94	3.3318(2)	36.99(1)	93.06	-	-	-	6.18	2.79	2.22
	1000	-	-	-	-	3.3327(2)	37.02(1)	99.44	4.3283(48)	81.09(27)	0.56	7.18	2.97	2.41
									NbZr					
Ti22Zr34Nb	600	-	-	-	-	3.3490(2)	37.56(1)	97.14	3.4573(18)	41.33(7)	2.86	4.66	2.73	1.71
									Zr					
	750	-	-	-	-	3.3512(1)	37.63(1)	100	-	-	-	4.93	2.98	1.65
	800	-	-	-	-	3.3515(1)	37.65(1)	100	-	-	-	6.13	2.64	2.32
	850	-	-	-	-	3.3527(2)	37.69(1)	99.78	4.5920(31)	96.83(20)	0.22	6.33	2.68	2.36
	1000	-	-	-	-	3.3537(2)	37.72(1)	99.63	4.5992(23)	97.29(15)	0.37	6.99	3.07	2.28

Table 2. *Cont.*

Specimen	PT [°C]	Ti(α)				Ti(β)			Additional Phase Nb0.81Zr0.19			R$_{wp}$ [%]	R$_{exp}$ [%]	S
		a [Å]	c [Å]	V [Å³]	PA [%]	a [Å]	V [Å³]	PA [%]	a [Å]	V [Å³]	PA[%]			
									Zr					
Ti30Zr34Nb	600	-	-	-	-	3.3528(2)	37.69(1)	100	-	-	-	5.03	2.44	2.06
	750	-	-	-	-	3.3677(2)	38.20(1)	100	-	-	-	4.6	2.56	1.80
	800	-	-	-	-	3.3698(1)	38.27(1)	99.15	4.6383(29)	99.79(19)	0.85	4.46	2.94	1.52
	850	-	-	-	-	3.3706(1)	38.29(1)	99.04	4.6236(14)	98.84(9)	0.96	4.33	2.71	1.60
	1000	-	-	-	-	3.3742(2)	38.42(1)	98.86	4.6288(8)	99.18(6)	1.14	4.37	3.21	1.36

The microstructure of the sintered specimen was determined by EBSD (Figure 6). Both alloys show similar mean grain sizes in the order of 1.2 to 1.7 μm. The black areas in the maps are miss-indexed points due to too small grains which cannot be measured by classic EBSD. The grain smaller than 300 nm has been discarded from the grain size distribution shown in Figure 7. The dual-phase Ti14Zr16Nb alloy shows an alpha fraction of ~39%. The beta phase in this alloy contains a lot of low angle boundaries, as seen in the misorientation angle distribution in Figure 7. The alpha phase shows a misorientation angle distribution similar to the random one. The single beta phase Ti23Zr25Nb alloy shows some low angle boundaries in the larger grains, but to a less extent than the beta phase of the Ti14Zr16Nb alloy.

Hardness and surface free energy by diiodomethane and glycerol contact angles of the Ti-Zr-Nb alloys were determined and the results listed in Table 3. Hardness for alloys was approximate 400 HV0.3. Contact angles for all alloys were much lower than 90° pointing their good wettability. Ti30Zr34Nb alloy was characterized by the highest value of surface free energy among all materials. The corrosion resistance of this alloy in the Ringer solution is also the highest which is indicated by the highest value of corrosion potential and the lowest value of corrosion current. All produced materials passivate in the higher potentials making their potentiodynamic curves not so different than that of pure titanium (Figure 8). This phenomenon is identified with no corrosion current increase in the anodic range of potentiodynamic curves and corresponds with the formation of the particular compounds on the material's surface, preventing them from further corrosive wear.
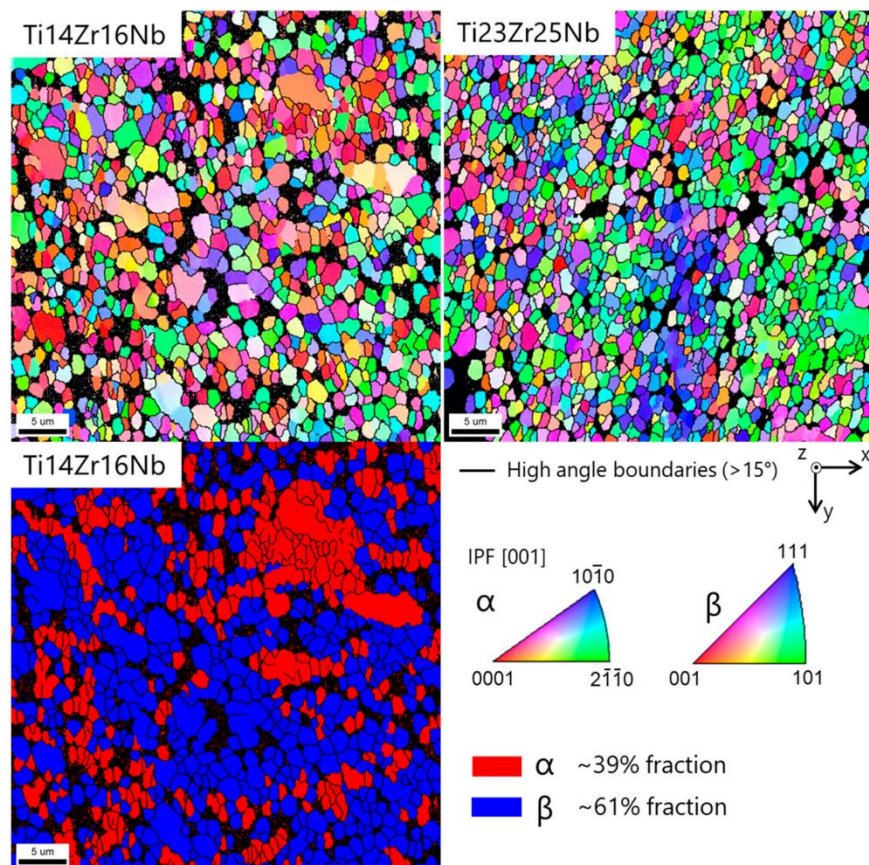
Figure 6. Top: Electron backscatter diffraction (EBSD) crystal orientation maps of α and β phases in Ti14Zr16Nb and Ti23Zr25Nb (only β phase) cold pressed and sintered at 750 °C for 30 min. The IPF color is displayed for the z-direction (cold pressing axis). Bottom: α and β phase distribution map in Ti14Zr16Nb.
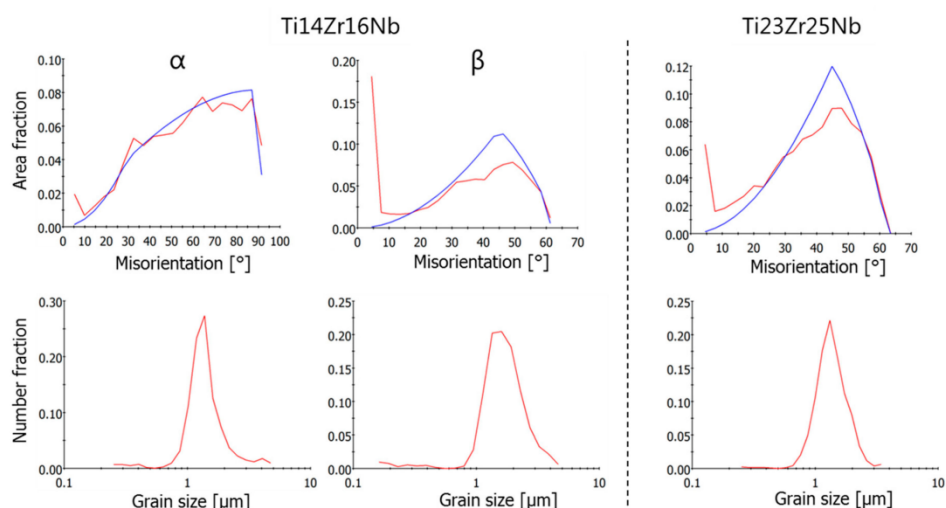
Figure 7. Misorientation angle and grain size distributions from EBSD measurements of α and β phases in Ti14Zr16Nb and Ti23Zr25Nb (only β phase) cold pressed and sintered at 750 °C for 30 min.

Table 3. Vickers hardness (HV0.3), surface free energy, diiodomethane, and glycerol contact angles for β and pseudo-β alloys Ti30Zr17Nb, Ti23Zr25Nb, Ti30Zr26Nb, and Ti30Zr34Nb, cold pressed and sintered at 750 °C for 30 min in comparison with dual-phase Ti14Zr16Nb processed in the same conditions. The results were obtained from the group of three replicated measurements.

Specimen	HV0.3	CA[M] Diiodomethane [°]	CA[M] Glycerol [°]	SFE [mN/m]
Ti14Zr16Nb	409 ± 17	53.4 ± 2.0	69.2 ± 2.2	35.0 ± 2.0
Ti30Zr17Nb	387 ± 14	59.8 ± 1.6	93.3 ± 3.3	29.1 ± 1.2
Ti23Zr25Nb	384 ± 13	54.0 ± 7.8	74.2 ± 6.8	34.4 ± 6.6
Ti30Zr26Nb	386 ± 15	65.1 ± 3.7	70.6 ± 2.5	30.8 ± 4.1
Ti30Zr34Nb	412 ± 17	48.0 ± 1.8	61.5 ± 6.2	40.0 ± 3.6
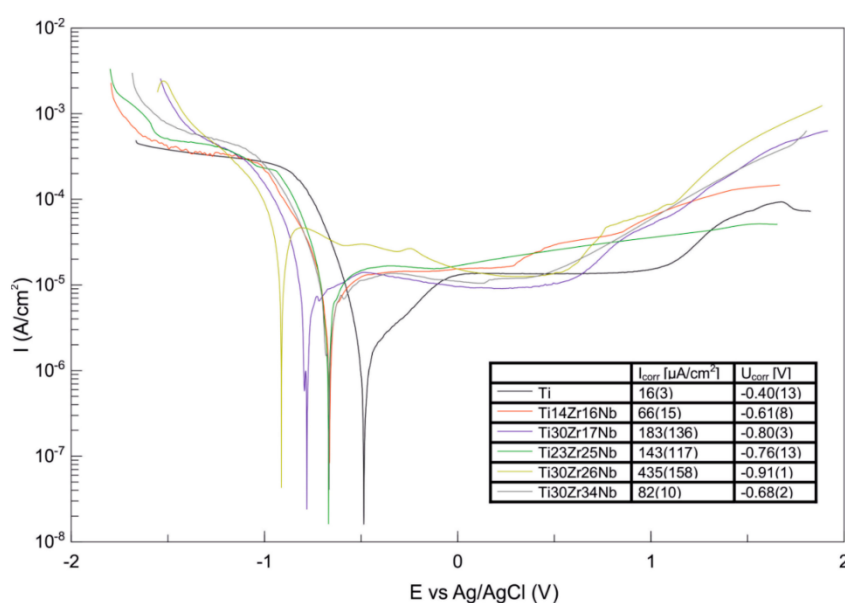
Figure 8. Potentiodynamic curves of bulk β and pseudo-β alloys Ti30Zr17Nb, Ti23Zr25Nb, Ti30Zr26Nb, Ti30Zr34Nb cold pressed and sintered at 750 °C for 30 min in comparison with dual-phase Ti14Zr16Nb processed in the same conditions. The results were obtained from the group of three replicated measurements.

Young modulus of all the β and pseudo-β Ti30Zr17Nb, Ti23Zr25Nb, Ti30Zr26Nb, and Ti30Zr34Nb is lower than 80 GPa and significantly lower than for dual-phase Ti14Zr16Nb alloy (Figure 9). There are no meaningful differences between the mechanically alloyed Ti-Nb-Zr alloys in terms of that property. Moreover, all the E modulus are nearly twice lower than pure titanium: 141 GPa [28].
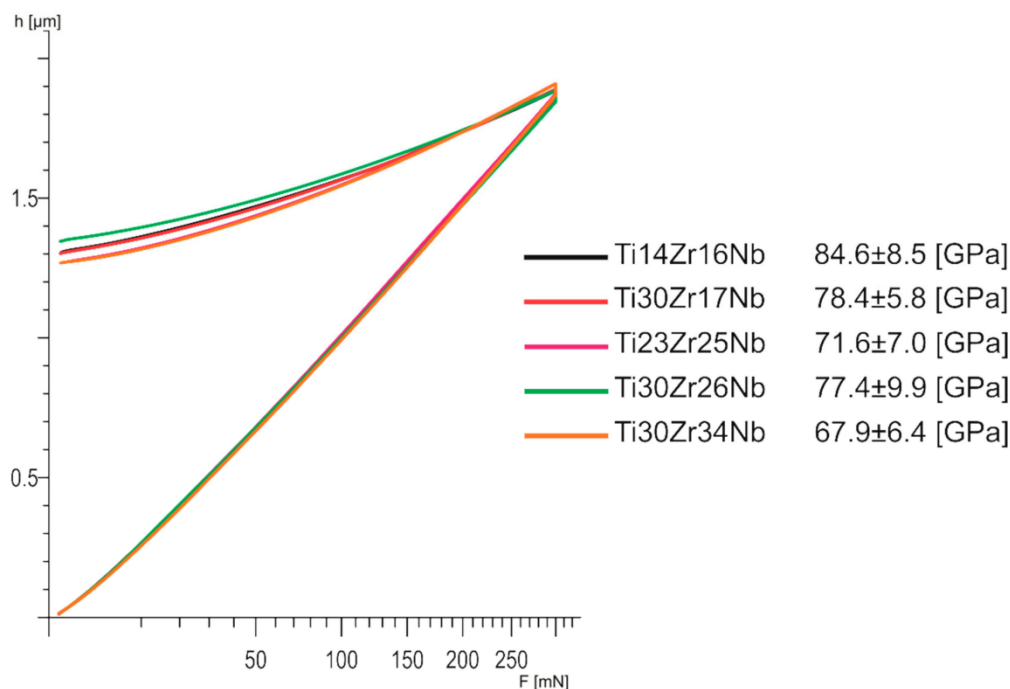
Figure 9. Load–depth curves of bulk β and pseudo-β alloys Ti30Zr17Nb, Ti23Zr25Nb, Ti30Zr26Nb, and Ti30Zr34Nb cold pressed and sintered at 750 °C for 30 min, in comparison with dual-phase Ti14Zr16Nb processed in the same conditions.

4. Discussion

Presented results clearly demonstrate that the powder manufacturing route supported by the mechanical alloying process allows the production of β-Ti-based alloys. Moreover, it was possible with the formation of ultrafine-grained structure. It could lead to better mechanical properties of produced alloys cause of the strengthening of the material with the use of the grain refinement mechanism.

In one of the latest papers of our group [28], the MA technique was used to manufacture Ti14Zr16Nb and Ti23Zr25Nb (at. %) alloys. A positive impact of using MA process on properties was due to the reduction of particle size, creation of new clean surfaces, and creation of various types of defects. These materials were prepared by the combination of mechanical alloying and powder metallurgy approach with cold powder compaction and sintering or interchangeably hot pressing. The mechanical alloying of Ti, Zr, and Nb for 10 h with additional hot pressing (71 MPa) and sintering for 10 min at 600 °C results in ultrafine-grained structure formation. It has been observed in the cited paper that the mechanically alloyed Ti23Zr25Nb material upon sintering at 600 °C for 10 min led to the formation of a single β-type phase alloy. Note that to control the crystal structure of Ti(β) alloys, processing parameters are a significant factor. These alloys are not only sensitive to the beta-stabilizers content but also to the sintering temperatures. However, Nb has much higher beta-stabilizing properties than Zr, which mainly leads to the spontaneous passivation of its alloys and does not form Ti(β) structure in the Ti-Zr binary alloys as a neutral element [46]. Henriques et al. synthesized the Ti–13Nb–13Zr alloy by conventional sintering [47]. The densification between 93 and 97% was achieved at a high sintering temperature of 1400 °C. Recently, nanostructured near-β Ti–20Nb–13Zr at. % alloy with nontoxic elements and enhanced mechanical properties have been synthesized by spark plasma sintering (SPS) of nanocrystalline powders obtained by mechanical alloying [37]. A nearly full density structure was

obtained after SPS at 1200 °C. The microstructure of the obtained alloy is a duplex structure with the α-Ti (hcp) region having an average size of 70–140 nm, surrounding the β-Ti (bcc) matrix. The obtained alloy was chemically homogenized with a microhardness value (HV) of 660. Compared to these results, it is clear that we were able to obtain by the powder metallurgy approach nearly full density in the Ti–Zr–Nb alloys, at a much lower temperature (600 °C) [28]. The synthesized Ti23Zr25Nb alloy was chemically homogenized with a hardness value, HV0.3 of 407. The Ti, Zr and Nb are nontoxic elements [10]. Additionally, Nb in Ti–Zr–Nb system act as β-stabilizer and Zr acts as a neutral element for forming a homogeneous solid solution in the α- and β-phases [48]. On the other hand, Nb is found to reduce the elastic modulus when alloyed with titanium [49]. Studies on Ti–Zr–Nb systems for medical applications have shown that α↔β phase transformations are sensitive not only by chemical composition but also by heat treatment parameters and cooling rates.

The Zr content in the Ti-Nb-Zr alloys not only allows the formation of the single-phase β-type alloys, but also influences the lattice constant of both Ti(α) and Ti(β)-phase. The increase of the Zr clearly expands the volume of the cell (Table 2). Nb in Ti-Nb-Zr does not have any impact on the Ti(β) lattice constants but increases the amount of the Ti(β) phase and volume of Ti(α) phase (in smaller range than Zr). The Ti-Zr alloys allow only to form a single-phase α-type alloys without β-phase presence because of no stabilization effect of Zr without the present of Nb in the alloy composition could not be observed. The volume of Ti(β) phase cell in the produced alloys varies from 36.65(1) Å^3 to 38.51(1) Å^3 and volume of Ti(α) phase vary from 36.73(2) Å^3 to 37.89(26) Å^3. The structure of produced alloys depends also on the temperature of sintering. It was observed that in the produced single β-phase alloys beneath 25 at. % Nb content (Ti23Zr16Nb, Ti30Zr17Nb, Ti23Zr25Nb Ti30Zr25Nb) in the temperatures above 750–800 °C lattice constant of Ti(β) phase decreases. In the dual-phase alloys (Ti14Zr16Nb, Ti14Zr25Nb) in the temperatures beneath 1000 °C the same situations always happen with the Ti(α) phase volume. The volume of Ti(β) phase grows in these two alloys continuously with the sintering temperature increase. In the alloys with Nb content from 23 at. % to 34 at. % Zr-phase appears in the higher temperatures. Moreover, in Ti22Zr34Nb alloy in the temperature of 600 °C the NbZr-phase diffraction peaks are visible and show the same group symmetry as Ti(β) phase but with a higher volume cell equals to 41.33(7) Å^3. It is the transitional phase that appears because of limited solubility in the lower temperature of Zr and Nb in Ti solid solution. It disappears in higher temperatures forming a single β-phase structure in the temperature of 750 °C and 800 °C.

The EBSD results show significant differences in microstructures between dual-phase Ti14Zr16Nb and a single β-phase Ti23Zr25Nb alloys. The misorientation distribution histograms can be easily contrasted (Figure 7). The recrystallization of Ti-Zr-Nb powders is driven by the energy stored in the mechanically alloyed materials coming from multiple crystal defects in the dominant form of the dislocations coming from the plastic deformation of powders during milling. These types of defects are considered to be the main part of the stored energy [50]. These alloys should be considered as high stacking fault energy materials with dynamic recovery and continuous dynamic recrystallization (CDRX) [50,51]. CDRX is the mechanism of low angle grain boundaries (LAGB) migration to the high angle grain boundaries (HAGB). It is clearly visible that CDRX in Ti14Zr16Nb alloy has not been completed cause a high amount of HAGB in comparison to the random distribution histograms. However, it was finished in Ti23Zr25Nb alloy with higher β-stabilizing Nb and Zr content. This type of histogram for this alloy matches the random one. The above result confirms that Ti14Zr16Nb alloys were not fully recrystallized in the provide sintering temperature of 750 °C because LAGB was not fully annihilated by HAGB. The thermal energy provided during sintering was not enough. However, the same temperature was enough to recrystallized and annihilate the HAGB in the Ti23Zr25Nb alloy. The Rietveld refinement results for Ti14Zr16Nb alloy (Table 2) shows the trend of the clear increase of Ti(β) phase fraction with sintering temperature. It is in parallel to the further recrystallization of this material. Nb and Zr limit the thermal energy provided to that materials during the sintering process and needed to fully recrystallize highly-defected Ti-Zr-Nb alloys after the mechanical alloying process which can be easily proven by the limitation of α→β phase transformation temperature in the

binary phase Ti-Nb and Ti-Zr diagrams. That is highly dependent on their β-stabilizing properties. EBSD results prove also an obtained ultrafine grain structure of prepared by mechanical alloying, cold compaction and sintering approach materials, with grain size significantly lower than one micron (Figure 7).

Moreover, the produced β and pseudo-β alloy—Ti30Zr17Nb, Ti23Zr25Nb, Ti30Zr26Nb, and Ti30Zr34Nb—have interesting properties in terms of their biomedical applications. Their corrosion properties are nearly similar to that of the pure titanium which means that they are not going to behave much differently inside the human body. However, the most important remains a significant reduction in their Young modulus comparing to pure titanium. These properties limit the stress shielding effect and increase the osteointegration which should be also stimulated by the porosities in these materials [52]. The obtained results are between 67.9 (Ti30Zr34Nb) and 84.6 (Ti14Zr16Nb) which makes their modulus near about twice lower than that of commercially pure titanium. The modulus of β and pseudo-β alloys are also lower than that of dual-phase α+β Ti14Zr16Nb alloy, which proves clearly the influence of the crystal structure of these materials on their mechanical properties.

In this work, the mechanical alloying process followed by the pressing and sintering was applied for the preparation of the bulk Ti-Zr-Nb near-β type alloys. The developed ultrafine-grained Ti-based alloys can be used as the implant materials in dental and orthopedics applications. The special interest should be focused on modifying these alloys by the formation of biocomposite materials. Biocomposite formed by adding 45S5 Bioglass to these alloys during milling can lead to interesting results as higher biocompatibility, hardness, and lower Young modulus. The structure, microstructure, porosity, surface morphology, corrosion resistance, wettability, and in vitro cytocompatibility will be investigated and the results will be published independently.

5. Conclusions

The Ti-Zr-Nb near-β type alloy $36 \leq Ti \leq 70$ (at. %) was synthesized by mechanical alloying and powder metallurgy method. The influence of Nb and Zr contents as also heat treatment on phase transitions (α→β) were studied. The main conclusions can be withdrawn: For the analyzed compositions, the Ti(β) –phase content can be increased with the longest processing time of mechanical alloyin; the formation of Ti(β) type alloys is possible after recrystallization of MA powders during its sintering in the wide range of process temperatures; with the increase of Zr and Nb amount in the Ti-Zr-Nb system, the Ti(β) phase content is higher and Zr has the main impact on the Ti(β) lattice constant and Nb on the beta-stabilizing effect; single-phase Ti(β) type Ti30Zr17Nb, Ti23Zr25Nb, Ti30Zr26Nb, Ti22Zr34Nb, and Ti30Zr34Nb alloys are synthesized after sintering at a low temperature (600 °C) for 30 min; the mechanical alloying and powder metallurgy approach remains beneficial in grain growth control and synthesis of ultrafine-grained Ti-Zr-Nb alloys for implant applications, the recrystallization process during sintering and final microstructure of Ti-Zr-Nb alloys clearly depends on the β-stabilizers content; and the developed ultrafine-grained Ti-Zr-Nb alloys could be used as the implant materials in dental and orthopedics applications because of their good properties as significantly reduced Young modulus in contrast to the commercially pure titanium and limitation of toxic elements as β-stabilizers.

References

1. Kuroda, D.; Niinomi, M.; Morinaga, M.; Kato, Y.; Yashiro, T. Design and mechanical properties of new β type titanium alloys for implant materials. *Mater. Sci. Eng. A* **1998**, *243*, 244–249. [CrossRef]
2. Rack, H.J.; Qazi, J.I. Titanium alloys for biomedical applications. *Mater. Sci. Eng. C* **2006**, *26*, 1269–1277. [CrossRef]
3. Geetha, M.; Singh, A.K.; Asokamani, R.; Gogia, A.K. Ti based biomaterials, the ultimate choice for orthopaedic implants—A review. *Prog. Mater. Sci.* **2009**, *54*, 397–425. [CrossRef]
4. Sidambe, A.T. Biocompatibility of advanced manufactured titanium implants—A review. *Materials* **2014**, *7*, 8168–8188. [CrossRef]
5. Rhoads, L.S.; Silkworth, W.T.; Roppolo, M.L.; Whittingham, M.S. Cytotoxicity of nanostructured vanadium oxide on human cells in vitro. *Toxicol. Vitr.* **2010**, *24*, 292–296. [CrossRef] [PubMed]
6. Dragan-Raileanu, L.A.; Cotrutz, C.E.; Munteanu, C.; Strugaru, S.; Avram, P.; Istrate, B.; Petreus, T. In vitro study regarding the cytotoxicity of some TiNbZr alloys. *Ann. Rom. Soc. Cell Biol.* **2013**, *18*, 186–191.
7. Gomes, C.C.; Moreira, L.M.; Santos, V.J.S.V.; Ramos, A.S.; Lyon, J.P.; Soares, C.P.; Santos, F.V. Assessment of the genetic risks of a metallic alloy used in medical implants. *Genet. Mol. Biol.* **2011**, *34*, 116–121. [CrossRef] [PubMed]
8. Costa, B.C.; Tokuhara, C.K.; Rocha, L.A.; Oliveira, R.C.; Lisboa-Filho, P.N.; Costa Pessoa, J. Vanadium ionic species from degradation of Ti-6Al-4V metallic implants: In vitro cytotoxicity and speciation evaluation. *Mater. Sci. Eng. C* **2019**, *96*, 730–739. [CrossRef] [PubMed]
9. Mohammed, M.T.; Khan, Z.A.; Siddiquee, A.N. Beta Titanium Alloys: The Lowest Elastic Modulus for Biomedical Applications: A Review Surface Modifications through FSP View project MACHINING View project. *Int. J. Chem. Nucl. Metall. Mater. Eng.* **2014**, *8*, 726–731.
10. Eisenbarth, E.; Velten, D.; Müller, M.; Thull, R.; Breme, J. Biocompatibility of β-stabilizing elements of titanium alloys. *Biomaterials* **2004**, *25*, 5705–5713. [CrossRef]
11. Thibon, I.; Ansel, D.; Gloriant, T. Interdiffusion in β-Ti-Zr binary alloys. *J. Alloys Compd.* **2009**, *470*, 127–133. [CrossRef]
12. Predel, B. Ti-Zr (Titanium-Zirconium). In *Pu-Re – Zn-Zr. Landolt-Börnstein—Group IV Physical Chemistry 5J*; Madelung, O., Ed.; SpringerMaterials: Berlin/Heidelberg, Germany, 1998.
13. Takahashi, M.; Kikuchi, M.; Okuno, O. Grindability of dental cast Ti-Zr alloys. *Mater. Trans.* **2009**, *50*, 859–863. [CrossRef]
14. Ikarashi, Y.; Toyoda, K.; Kobayashi, E.; Doi, H.; Yoneyama, T.; Hamanaka, H.; Tsuchiya, T. Improved biocompatibility of titanium-zirconium (Ti-Zr) alloy: Tissue reaction and sensitization to Ti-Zr alloy compared with pure Ti and Zr in rat implantation study. *Nippon Kinzoku Gakkaishi/J. Japan Inst. Met.* **2007**, *71*, 395–401. [CrossRef]
15. Nagase, T.; Kinoshita, K.; Nakano, T.; Umakoshi, Y. Fabrication of Ti-Zr binary metallic wire by arc-melt-type melt-extraction method. *Mater. Trans.* **2009**, *50*, 872–878. [CrossRef]
16. Moffat, D.L.; Kattner, U.R. Stable and metastable Ti-Nb phase diagrams. *Metall. Trans. A, Phys. Metall. Mater. Sci.* **1988**, *19 A*, 2389–2397. [CrossRef]
17. Xu, L.J.; Xiao, S.L.; Tian, J.; Chen, Y.Y.; Huang, Y.D. Microstructure and dry wear properties of Ti-Nb alloys for dental prostheses. *Trans. Nonferrous Met. Soc. China (English Ed.)* **2009**, *19*, 639–644. [CrossRef]
18. Karre, R.; Niranjan, M.K.; Dey, S.R. First principles theoretical investigations of low Young's modulus beta Ti-Nb and Ti-Nb-Zr alloys compositions for biomedical applications. *Mater. Sci. Eng. C* **2015**, *50*, 52–58. [CrossRef]
19. Chang, L.L.; Wang, Y.D.; Ren, Y. In-situ investigation of stress-induced martensitic transformation in Ti-Nb binary alloys with low Young's modulus. *Mater. Sci. Eng. A* **2016**, *651*, 442–448. [CrossRef]
20. Elmay, W.; Patoor, E.; Bolle, B.; Gloriant, T.; Prima, F.; Eberhardt, A.; Laheurte, P. Optimisation of mechanical properties of Ti-Nb binary alloys for biomedical applications. *Comput. Methods Biomech. Biomed. Engin.* **2011**, *14*, 119–120. [CrossRef]
21. Predel, B. Nb-Ti (Niobium-Titanium). In *Li-Mg – Nd-Zr. Landolt-Börnstein—Group IV Physical Chemistry 5H*; Madelung, O., Ed.; SpringerMaterials: Berlin/Heidelberg, Germany, 1997.
22. Kim, S.E.; Jeong, H.W.; Hyun, Y.T.; Lee, Y.T.; Jung, C.H.; Kim, S.K.; Song, J.S.; Lee, J.H. Elastic modulus and in vitro biocompatibility of Ti-xNb and Ti-xTa alloys. *Met. Mater. Int.* **2007**, *13*, 145–149. [CrossRef]

23. Meng, Q.; Zhang, J.; Huo, Y.; Sui, Y.; Zhang, J.; Guo, S.; Zhao, X. Design of low modulus β-type titanium alloys by tuning shear modulus C44. *J. Alloys Compd.* **2018**, *745*, 579–585. [CrossRef]

24. Wang, P.; Wu, L.; Feng, Y.; Bai, J.; Zhang, B.; Song, J.; Guan, S. Microstructure and mechanical properties of a newly developed low Young's modulus Ti–15Zr–5Cr–2Al biomedical alloy. *Mater. Sci. Eng. C* **2017**, *72*, 536–542. [CrossRef] [PubMed]

25. Frutos, E.; Karlík, M.; Jiménez, J.A.; Langhansová, H.; Lieskovská, J.; Polcar, T. Development of new β/α"-Ti-Nb-Zr biocompatible coating with low Young's modulus and high toughness for medical applications. *Mater. Des.* **2018**, *142*, 44–55. [CrossRef]

26. Suryanarayana, C. Mechanical alloying and milling. *Prog. Mater. Sci.* **2001**, *46*, 1–184. [CrossRef]

27. Zeng, L.; Xu, G.; Liu, L.; Bai, W.; Zhang, L. Experimental investigation of phase equilibria in the Ti-Fe-Zr system. *Calphad Comput. Coupling Phase Diagrams Thermochem.* **2018**, *61*, 20–32. [CrossRef]

28. Marczewski, M.; Miklaszewski, A.; Jurczyk, M. Structure evolution analysis in ultrafine-grained Zr and Nb-based beta titanium alloys. *J. Alloys Compd.* **2018**, *765*, 459–469. [CrossRef]

29. Chen, W.; Chen, C.; Zi, X.; Cheng, X.; Zhang, X.; Lin, Y.C.; Zhou, K. Controlling the microstructure and mechanical properties of a metastable β titanium alloy by selective laser melting. *Mater. Sci. Eng. A* **2018**, *726*, 240–250. [CrossRef]

30. Kreitcberg, A.; Brailovski, V.; Prokoshkin, S. New biocompatible near-beta Ti-Zr-Nb alloy processed by laser powder bed fusion: Process optimization. *J. Mater. Process. Technol.* **2018**, *252*, 821–829. [CrossRef]

31. Bahl, S.; Das, S.; Suwas, S.; Chatterjee, K. Engineering the next-generation tin containing β titanium alloys with high strength and low modulus for orthopedic applications. *J. Mech. Behav. Biomed. Mater.* **2018**, *78*, 124–133. [CrossRef]

32. Sochacka, P.; Miklaszewski, A.; Jurczyk, M. The influence of mo content on phase transformation in Ti-Mo alloys. *Arch. Metall. Mater.* **2017**, *62*, 2051–2056. [CrossRef]

33. Guo, S.; Zhang, J.; Shang, Y.; Zhang, J.; Meng, Q.; Cheng, X.; Zhao, X. A novel metastable β-type Zr-12Nb-4Sn alloy with low Young's modulus and low magnetic susceptibility. *J. Alloys Compd.* **2018**, *745*, 234–239. [CrossRef]

34. Lee, D.G.; Lee, Y.T.; Mi, X.; Ye, W.; Hui, S. Beta-Based Titanium Alloy with Low Elastic Modulus. U.S. Patent 20110070121A1, 24 March 2011.

35. Lee, D.G.; Lee, Y.T.; Mi, X.; Ye, W.; Hui, S. Beta-Based Titanium Alloy with Low Elastic Modulus. U.S. Patent 20140112820A1, 24 April 2014.

36. Tulinski, M.; Jurczyk, M. Nanomaterials Synthesis Methods. In *Metrology and Standardization of Nanotechnology*; Mansfield, E., Kaiser, D., Fujita, D., Eds.; Wiley-VCH: Weinheim, Germany, 2017; pp. 75–98.

37. Hussein, M.A.; Suryanarayana, C.; Al-Aqeeli, N. Fabrication of nano-grained Ti-Nb-Zr biomaterials using spark plasma sintering. *Mater. Des.* **2015**, *87*, 693–700. [CrossRef]

38. He, Y.; Zhang, Y.; Meng, Z.; Jiang, Y.; Zhou, R. Microstructure evolution, mechanical properties and enhanced bioactivity of Ti-Nb-Zr based biocomposite by bioactive calcium pyrophosphate. *J. Alloys Compd.* **2017**, *720*, 567–581. [CrossRef]

39. Bai, W.; Tian, Y.; Xu, G.; Yang, Z.; Liu, L.; Masset, P.J.; Zhang, L. Diffusivities and atomic mobilities in bcc Ti-Zr-Nb alloys. *Calphad Comput. Coupling Phase Diagrams Thermochem.* **2019**, *64*, 160–174. [CrossRef]

40. Yang, J.; Baatarsukh, M.; Bae, J.; Huh, S.; Jeong, H.; Choi, B.; Nam, T.; Noh, J. Phase stability and properties of Ti-Nb-Zr thin films and their dependence on Zr addition. *Materials* **2018**, *11*, 1361. [CrossRef]

41. Mote, V.; Purushotham, Y.; Dole, B. Williamson-Hall analysis in estimation of lattice strain in nanometer-sized ZnO particles. *J. Theor. Appl. Phys.* **2012**, *6*. [CrossRef]

42. Mccusker, L.B.; Von Dreele, R.B.; Cox, D.E.; Louër, D.; Scardi, P. Rietveld refinement guidelines. *J. Appl. Crystallogr.* **1999**, *32*, 36–50. [CrossRef]

43. Marquardt, D.W. An Algorithm for Least-Squares Estimation of Nonlinear Parameters. *J. Soc. Ind. Appl. Math.* **1963**, *11*, 431–441. [CrossRef]

44. Fitzgibbon, A.; Pilu, M.; Fisher, R.B. Direct least square fitting of ellipses. *IEEE Trans. Pattern Anal. Mach. Intell.* **1999**, *21*, 476–480. [CrossRef]

45. Adamek, G.; Jakubowicz, J. Microstructure of the mechanically alloyed and electrochemically etched Ti-6Al-4V and Ti-15Zr-4Nb nanocrystalline alloys. *Mater. Chem. Phys.* **2010**, *124*, 1198–1204. [CrossRef]

46. O'Brien, B.; Stinson, J.; Carroll, W. Development of a new niobium-based alloy for vascular stent applications. *J. Mech. Behav. Biomed. Mater.* **2008**, *1*, 303–312. [CrossRef] [PubMed]

47. Henriques, V.A.R.; Galvani, E.T.; Petroni, S.L.G.; Paula, M.S.M.; Lemos, T.G. Production of Ti-13Nb-13Zr alloy for surgical implants by powder metallurgy. *J. Mater. Sci.* **2010**, *45*, 5844–5850. [CrossRef]

48. Elias, L.M.; Schneider, S.G.; Schneider, S.; Silva, H.M.; Malvisi, F. Microstructural and mechanical characterization of biomedical Ti-Nb-Zr(-Ta) alloys. *Mater. Sci. Eng. A* **2006**, *432*, 108–112. [CrossRef]

49. Wang, L.; Yang, G.; Yang, H.; Cao, J.; Lü, W.; Zhang, D. Characterization of microstructure and mechanical properties of TiNbZr alloy during heat treatment. *Xiyou Jinshu Cailiao Yu Gongcheng/Rare Met. Mater. Eng.* **2009**, *38*, 1136–1140.

50. Alaneme, K.K.; Okotete, E.A. Recrystallization mechanisms and microstructure development in emerging metallic materials: A review. *J. Sci. Adv. Mater. Devices* **2019**, *4*, 19–33. [CrossRef]

51. Bobbili, R.; Madhu, V. Dynamic recrystallization behavior of a biomedical Ti-13Nb-13Zr alloy. *J. Mech. Behav. Biomed. Mater.* **2016**, *59*, 146–155. [CrossRef]

52. Apostu, D.; Lucaciu, O.; Berce, C.; Lucaciu, D.; Cosma, D. Current methods of preventing aseptic loosening and improving osseointegration of titanium implants in cementless total hip arthroplasty: A review. *J. Int. Med. Res.* **2018**, *46*, 2104–2119. [CrossRef]

Artykuł nr 3:

M. Marczewski, M.U. Jurczyk, K. Kowalski,

A. Miklaszewski, P.K. Wirstlein, M. Jurczyk,

Composite and surface functionalization of
ultrafine-grained Ti23Zr25Nb alloy for medical
applications

Composite and Surface Functionalization of Ultrafine-Grained Ti23Zr25Nb Alloy for Medical Applications

Mateusz Marczewski [1,*], **Mieczysława U. Jurczyk** [2], **Kamil Kowalski** [1],
Andrzej Miklaszewski [1], **Przemysław K. Wirstlein** [3] **and Mieczysław Jurczyk** [1]

1. Institute of Materials Science and Engineering, Poznan University of Technology, Jana Pawła II 24, 61-138 Poznan, Poland; kamil.kowalski@put.poznan.pl (K.K.); andrzej.miklaszewski@put.poznan.pl (A.M.); mieczyslaw.jurczyk@put.poznan.pl (M.J.)
2. Division of Mother's and Child's Health, Poznan University of Medical Sciences, Polna 33, 60-535 Poznan, Poland; mjur@poczta.onet.pl
3. Department of Gynaecology and Obstetrics, Division of Reproduction, Poznan University of Medical Sciences, Polna 33, 60-535 Poznan, Poland; abys@wp.pl
* Correspondence: mateusz.p.marczewski@doctorate.put.poznan.pl; Tel.: +48-61-665-3508

check for updates

Abstract: In this study, the ultrafine-grained Ti23Zr25Nb-based composites with 45S5 Bioglass and Ag, Cu, or Zn additions were produced by application of the mechanical alloying technique. Additionally, the base Ti23Zr25Nb alloy was electrochemically modified in the two stages of processing: electrochemical etching in the solution of H_3PO_4 and HF followed by electrochemical deposition in $Ca(NO_3)_2$, $(NH_4)_2HPO_4$, and HCl. The in vitro cytocompatibility studies were also done with comparison to the commercially pure titanium. The established cell lines of Normal Human Osteoblasts (NHost, CC-2538) and Human Periodontal Ligament Fibroblasts (HPdLF, CC-7049) were used. The culture was conducted among the tested materials. Ultrafine-grained titanium-based composites modified with 45S5 Bioglass and Ag, Cu, or Zn metals have higher biocompatibility than the reference material in the form of a microcrystalline Ti. Proliferation activity was at a stable level with contact with studied materials. In vitro evaluation research showed that the ultrafine-grained Ti23Zr25Nb-based composites with 45S5 Bioglass and Ag, Cu, or Zn additions, with a Young modulus below 50 GPa, can be further used in the biomedical field.

Keywords: Ti alloys; 45S5 Bioglass; metal matrix composites; electrochemical deposition; cell proliferation

1. Introduction

β-type titanium alloys are promising materials based on the current research studies in terms of their biological properties. Currently published results of TiNb, TiZrNb, TiNbTa, TiNbSn, TiNbHf, TiMoNb, TiMoTa, TiNbTaZr, TiNbZrAl, TiNbZrSi, and TiNbZrTaSiFe confirm their high biocompatibility and makes them interesting for further research studies and development in the biomedical field [1–11]. Zr, Nb, and Mo (with titanium-based alloys containing these elements) are biocompatible, and their cytotoxicity is lower than that for pure titanium [12].

The modification of titanium with calcium phosphate (CP) is a widely used method to modify the properties of titanium biomaterials. There are numerous methods of doing so and diverse research studies proving the utility of this type of modification (especially considering the enhancements of biological properties as excellent biocompatibility). CP could be used in the form of coatings. It has revealed the possibility of increasing the biological properties of the material. Various deposition

methods can be applied to obtain CP layers on the titanium substrate, including plasma spraying, electrophoretic deposition, and electrochemical deposition (ED). The electrodeposition methods offer many advantages compared to other methods. During the ED process, it is possible to control the chemical composition of layers and their thickness. ED also allows covering irregular shapes and porous structures of implants. The formation of multilayer and two-layer composites of hydroxyapatites (HA) with titanium oxide leads to increased cell proliferation [13]. The nano titanium oxides as a monolayer also can form the surface with interesting properties such as high osteointegration properties [14]. Hydrothermal treatment leading to calcium titanate formation increases apatites' formation on the titanium surface in the body fluids, enhancing its biocompatibility [15]. Recently, a high point of interest was also focused on the doping of this type of coatings. Calcium phosphates modification with silver, silicon, strontium, magnesium, zinc, cobalt, and multiwalled carbon nanotubes leads to the formation of the coating with no toxicity against fibroblast and high potential because of the improved osteointegration [16–19]. The production of titanium-based composites containing calcium phosphates also provides a faster growth of apatites on the material and high biocompatibility with excellent mechanical properties [20,21].

There is also high interest in biomaterials engineering for the use of bioglasses such as 45S5 Bioglass [22]. The bioglass can also be additionally modified with the incorporation of many different elements. The addition of niobium in 45S5 Bioglass could stimulate the regeneration of the bone tissue [23,24]. The bioglass properties could also be further improved with the addition of selenium, magnesium, zinc, and hydroxyapatite [25,26]. The addition of graphene oxides can lead to both enhancing the biocompatibility and antibacterial properties [27].

45S5 Bioglass can be used as a coating to improve titanium and titanium-based alloys further, mainly their biocompatibility [28]. 45S5 Bioglass is added as a ceramic component of metal-matrix titanium-based composites. This type of composites could be easily produced with a mechanical alloying technique leading to the further improvement of composite properties and high cytocompatibility compared to commercially available pure titanium [29]. The properties of biomedical materials could also be enhanced with a different grade of bioglass as S53P4 Bioglass [30]. This type of modification was proved to be efficient in terms of β-type titanium alloys. Both hydroxyapatite and 45S5 Bioglass have proved to enhance many different alloys' biocompatibility as Mg-based alloys [31,32]. The formation of calcium hydroxide on the titanium surface is also beneficial because of their antibacterial and osseointegration properties [33,34]. The same increase in the biocompatibility could have also been achieved with the production of other calcium-decorated coatings [35].

One of the most popular methods of modifying β-type titanium to increase their osteointegration properties is foams' formation. This method was successfully used in the alloy containing niobium and zirconium using different foaming agents [36–38]. The foam production could also be applied in the titanium-based composites such as TiNb-HA composites [39]. It is also possible to produce porous coatings to increase bone tissue ingrowth into the modified implant [40].

The synthesis of bulk ultrafine-grained Ti-based materials is possible using a mechanical alloying approach allowing the refinement of powders to even the nanometer scale with its further consolidation [29,31,32,41,42]. The synthesis of ultrafine-grained β-type titanium alloys might enhance the properties of materials used in medicine. One of these alloys is Ti-Zr-Nb alloys with Nb and Zr used as the β-stabilizers [41,42]. These elements' biocompatibility is higher than that of commercially used aluminum and vanadium in the commercially available Ti6Al4V alloys [12,43]. The production of alloys with a single-phase Ti(β) structure is possible with the alloys as Ti30Zr17Nb, Ti23Zr25Nb, Ti30Zr26Nb, Ti22Zr34Nb, and Ti30Zr34Nb even after consolidation in the temperature as low as 600 °C [42].

Ultrafine-grained Ti-based materials, due to exceptional physicochemical, mechanical, and biological properties, are considered as the next-generation biomaterials [44,45]. The main research task is to adjust the microstructure and chemical composition, leading to increased cell proliferation among the osseointegration of potentially produced implants. Proliferation can be

improved by the chemical composition of materials and its surface properties with roughness included. However, the roughness of the medical product can lead to undesirable pathogens colonization [46]. That leads to other goals in enhancing the material as the limitation of these types of phenomena. As one possible way of doing so, silver particles were already studied in these applications [47]. The proposed production method with mechanical alloying led to the formation of the β-type titanium alloys with Nb and Zr with the mean average grain size of 1.2 to 1.7 μm, which proved it to be the ultrafine-grained material [42].

The structure and corrosion resistance as well as the wettability properties of surface-modified material were also examined in this work. The mechanical properties of Ti23Zr25Nb-based materials were summarized with commercially available titanium (rod Grade 2), arc-melted microcrystalline Ti18Zr24Nb, and Ti23Zr25Nb-based foam used as the reference samples to present and analyze their relations. Biocomposites formation was considered a much more effective way of Young modulus limitation than the foam formation. The significant reduction in elastic modulus is a way of reducing the risk of the stress shielding effect. Moreover, increased osseointegration is possible because of the porosities in these materials [48]. The influence of chemical composition on the biological properties was investigated. Additionally, the possibilities of electrochemical surface modification for a further improvement of osteointegration and the cytocompatibility properties of ultrafine-grained Ti23Zr25Nb alloy were introduced, and the biological properties of the so modified materials were revealed. The synthesized β alloy, Ti23Zr25Nb, has interesting properties for biomedical application.

In vitro, a cytocompatibility test was done to assess the toxicity and the interaction process with the proliferation activity in all the tested materials, including those functionalized with surface modification and composite formation. The established cell line of Normal Human Osteoblasts (NHost) and Human Periodontal Ligament Fibroblasts (HPdLF) was cultured among all tested materials.

2. Materials and Methods

The present work covers the research results for the surface and composite functionalized Ti23Zr25Nb (at.%) alloys.

In this study, synthesized materials are denoted as follows:

A0	annealed titanium rod (Grade 2)
B0	Ti23Zr25Nb—cold pressed and sintered at 800 °C for 30 min
B1*	Ti23Zr25Nb—electrochemically etched
B1	Ti23Zr25Nb—electrochemically deposited calcium and phosphorus-riched coating
B2	Ti23Zr25Nb—9 wt.% 45S5 Bioglass
B3	Ti23Zr25Nb—9 wt.% 45S5 BG–1 wt.% Ag
B4	Ti23Zr25Nb—9 wt.% 45S5 BG–1 wt.% Cu
B5	Ti23Zr25Nb—9 wt.% 45S5 BG–1 wt.% Zn
B7	microcrystalline arc-melted Ti18Zr24Nb (at.%)
B8	hot-pressed at 600 °C for 10 min
B9	Ti23Zr25Nb-based foam.

2.1. Sample Preparation

The production of all materials was conducted from the following powdered precursors: Ti (CAS:7440-32-6, 99.9% purity, Alfa Aesar, Haverhill, MA, USA), Nb (CAS:7446-03-1, 99.8% purity, Sigma Aldrich, St. Louis, MO, USA), 45S5 Bioglass (45% SiO_2, 24.5% Na_2O, 24.5 CaO, 6% P_2O_5, Mo-Sci GL0160P, Mo-Sci, Rolla, MO, USA), Ag (CAS:7440-22-4, 99.9% purity, Alfa Aesar) powders, Cu (CAS:7440-66-6, 99% purity, Sigma Aldrich) turnings, Zn (CAS:7440-66-6, 99% purity, Sigma Aldrich) granules, and Zr fillings from a sponge (CAS:7440-50-8, purity ≥99%, Sigma Aldrich). The commercial pure (CP-Ti) microcrystalline titanium (Ti) with purity >99.6% (Grade 2) cut from the rod delivered at the annealed state from Goodfellow (Huntingdon, UK) was used as a control sample for the in vitro cytocompatibility test and the nanoindentation measurements. The mechanical alloying process and

the powder consolidation (cold compaction and sintering) were provided as in the previous article of our scientific group [41]. The pellets have d = 6 mm in diameter and h = 3 mm in height.

The Ti23Zr25Nb alloy was electrochemically modified. Before the modification, the sample was polished with the grinding paper of 600 grit and cleaned with an ultrasonic bath and ethanol. Additionally, to conduct the electrochemical process only on the one sample's surface, other surfaces were protected by covering with the heat-resistant silicone gasket. The process was divided into two stages. The first stage of electrochemical etching was conducted in the bath containing 1 M H_3PO_4 + 2% HF with the use of Solartron 1285 potentiostat (Solartron Analytical, Farnborough, UK) and platinum electrode in the voltage of 10 V vs. OCP for 60 min. The second stage was conducted in the bath containing 0.042 M $Ca(NO_3)_2$ + 0.025 M $(NH_4)_2HPO_4$ + 0.1 M HCl using the same equipment. Process parameters were −10 V vs. OCP voltage and 60 min.

In contrast to nanoindentation load–depth curves of the Ti23Zr25Nb-9BG composite, the results of Ti23Zr25Nb-based foam and microcrystalline arc-melted Ti18Zr24Nb alloy were additionally presented. The foam was made with the addition of 40% ammonium bicarbonate (Alfa Aesar, 98% purity) (to Ti23Zr25Nb powder ratio). Sintering was conducted in two stages. The first stage was carried out at 175 °C for 2 h in the vacuum. In the second stage, the temperature was set at 1150 °C for 10 h in the protective high-purity argon atmosphere.

2.2. Materials Characterization

The electrochemically modified sample's crystal structure was characterized by the Panalytical Empyrean XRD equipment (Almelo, Netherlands) with the copper (CuKα) radiation source. The following measurement parameters were used: voltage 45 kV, anode current 40 mA, 2 theta range 30–80°, time per step 60.325 s/step, and step size 0.0334°.

The microstructure of the modified materials was revealed with the scanning electron microscope technique. A Mira-3 Tescan microscope (Tescan, Brno, Czech Republic) was used for this purpose. The corrosion properties of the materials were determined with the potentiodynamic tests. A Ringer's solution and Ag/AgCl reference electrode were used for that purpose with the following testing parameters: −1 V to 2.5 V vs. OCP range and 1 mV/s scan speed. The samples' surface morphology was investigated using a profiler T8000 (Hommel-Etamic, Villingen-Schwenningen, Germany). EVOVIS software (Hommel-Etamic, Villingen-Schwenningen, Germany) was used to analyze the measured profiles, which allows us to calculate roughness parameters (ISO 25178-2) [49]: arithmetic mean roughness (μm)—R_a, the maximum height of the profile (μm)—R_t, ten-point mean roughness (μm)—R_z. Contact angles (CA) for diiodomethane and glycerol testing fluids and surface free energy (SFE) were calculated using the Kruss-DSA25 instrument and Kruss-Advanced 1.5 software (Krüss, Hamburg, Germany). An ellipse fitting method was applied to calculate the contact angles of materials [50]. The surface free energy was calculated using the Owens, Wendt, Rabel, and Kaelble (OWRK) method [51,52]. Tests were carried out at ambient conditions (23 °C). Multiple measurements of the single 2 μL drop, dosed with the speed of 0.2 mL/min, were handled for 2 s with the probing frequency of 50 fps. Corrosion and wettability results were based on the three repeated measurements for the data analysis and uncertainties calculations. Nanoindentation measurements were conducted with Picodentor HM500 (Fischer Technology Inc., Windsor, CT, USA). The parameters were as follows: 300 mN load applied for 5 s. A Vickers' tip was used as the indenter for these measurements. The elastic modulus of materials based on the load–depth curves was calculated with the Oliver–Pharr method [53]. Details of the run tests are the same as in the previous research studies [41,42].

2.3. In Vitro Biocompatibility Studies

Cultures in a conditioned medium were carried out to investigate the potential cytotoxic effects of the insert's components that entered the solution (breeding medium). To sterilize the inserts, they were immersed in a 70% solution of the ethanol, diluted with distilled water, and dried in a laminar flow hood with the UV sterilization of each side of the sample for 12 h.

2.3.1. Cell Lines Preparation

Primary cell lines, Normal Human Osteoblasts (NHost, CC-2538), and Human Periodontal Ligament Fibroblasts (HPdLF, CC-7049) were purchased together with a dedicated set of breeding media, respectively: CC-3207 OGM Osteoblast Growth BulletKit (CC-3208 + CC-4193) and CC-3205 SCGM Stromal Bullet CellKit (CC-3204 + CC-4181) at LONZA Group Ltd. (Morristown, NJ, USA). After thawing, the cells were sown into 25 cm^2 cultured bottles. Cell multiplication was carried out until 80% of the cultured vessels' surface coverage was obtained by cells, and the cells were transferred to new vessels. Cells were cultured under standard conditions in plastic plates in the Haereus BB16 incubator (Haereus, Hanau, Germany) at 37 °C temperature in an atmosphere of 5% CO_2, and increased humidity level of 95%.

2.3.2. Conditioning of Breeding Media

Half of each type of prepared and sterilized inserts was placed (the test surface down) in an unsupplemented medium (1.25 mL of substrate per 1 cm^2 insert) OBM dedicated to breeding the original line of human osteoblasts (Osteoblasts Basal Medium, #CC-3208; LONZA Group Ltd., Morristown, NJ, USA), the second half in an unsupplemented, dedicated medium for the breeding of human fibroblasts, SCBM (Stromal Cell Basal Medium, #CC-3204; LONZA Group Ltd., Morristown, NJ, USA) Inserts were incubated for 24 h in closed culture bottles, on zirconium balls (ϕ2 mm) at 37 °C, on an orbital shaker (100 rpm). After the incubation, the protected medium was centrifuged 1300× *g* for 10 min and then filtered through a 0.22 mm microfilter (Millipore, Burlington, MA, USA). Then, the substrates were protected in a refrigerator (4 °C) until the growth of cells conditioned in the medium was performed. Directly before the experiment, conditioned substrates were supplemented with dedicated sets of supplements: #CC-4193—fetal bovine serum (FBS), vitamin C. 50 mg/mL, and antibiotic mixture (LONZA Group Ltd.; Morristown, NJ, USA) for OBM medium. Medium SCBM was added with a set of #CC-4181—FBS, rhFGF (Recombinant Human Fibroblast Growth Factor), insulin, and antibiotic mix.

2.3.3. The Cytotoxicity Evaluation of Inserts and Cell Survival by MTS Assay

The inserts tested's possible cytotoxic effect was evaluated using the CellTiter 96$^\circledR$ AQueous Non-Radioactive Cell Proliferation Assay (MTS) (Promega, WI, USA). The lifespan assessment was used to measure the ability of live cells to convert MTS into a colored product—a formazan whose concentration is proportional to the number and metabolic activity of cells. Up to 96-well culture plates were sown with 2.5×10^3 cells of each type. The cells were grown for 24, 72, and 120 h in each cell type and test materials, conditioned, fermented, and medium diluted with the fresh added medium in a ratio of 1:1, at a volume of 300 μL per well. Cell culture in a conditioned medium was carried out in parallel with the culture of cells of a given type, growing in a completely fresh, insulating medium.

At the end of each time interval, an MTS test was performed for both cell types following the manufacturer's instructions. In short, before the test, the culture medium was listed on the test plate by adding 100 mL of a new portion of the conditioned medium mixture in a ratio of 1:1 with a fresh culture medium and 20 mL of MTS working solution. The cells were incubated with culture conditions 37 °C/95% H_2O/5% CO_2 for 1.5 h until the product's color solution was obtained.

The product's concentration was measured spectrophotometrically at λ = 490 nm in the ELISA plate reader, MRX Dynex (Chantilly, VA, USA). The measurement was made against a negative control, which was a reaction in wells without cells sown. All farms were conducted in triplicate. For each cell type and conditioned medium, the MTS test results were averaged.

The relative viability of the cells (RVC) was calculated based on the value of absorbance from the equation:

$$\text{RVC (\%)} = [(a - b)/(c - b)] \times 100 \text{ (\%)}, \tag{1}$$

where a—mean absorbance of the tested sample (corrected to specific background), b—mean absorbance of blank control (reaction without the cells), and c—mean absorbance of medium conditioned with a reference sample (microcrystalline Ti, with the correction to specific background).

2.3.4. Cell Culture for Photographic Documentation

In parallel, on 24-hole breeding plates, on glass inserts (ϕ13 mm), osteoblasts and fibroblasts were established in conditioned culture media and prepared for the MTS test. Farms were farmed at 37 °C/95% H_2O/5% CO_2 for 24, 72, and 120 h. After this time, the cells were fixed in a 2% solution of glutaraldehyde in PBS. The cells fixed on the inserts were colored with methyl blue solution and rinsed in ddH_2O. After drying, microscopic preparations were made based on which photographic documentation was made in the 150× magnification using a Nikon microscopic kit and a digital camera (Nikon, Tokyo, Japan).

3. Results and Discussion

3.1. Structure Properties

The electrochemically etched sample, followed with the electrochemical deposition, leads to the calcium and phosphorus-riched coating formation. This coating's crystal structure was mainly the calcium hydroxide—Ca(OH)$_2$ (Figure 1). The other phases that were identified with the X-ray diffraction include hydroxyapatite—Ca$_5$(PO4)$_3$(OH) (with peaks of much lower intensity) and Ti(β) (the crystal structure of the base Ti23Zr25Nb material).
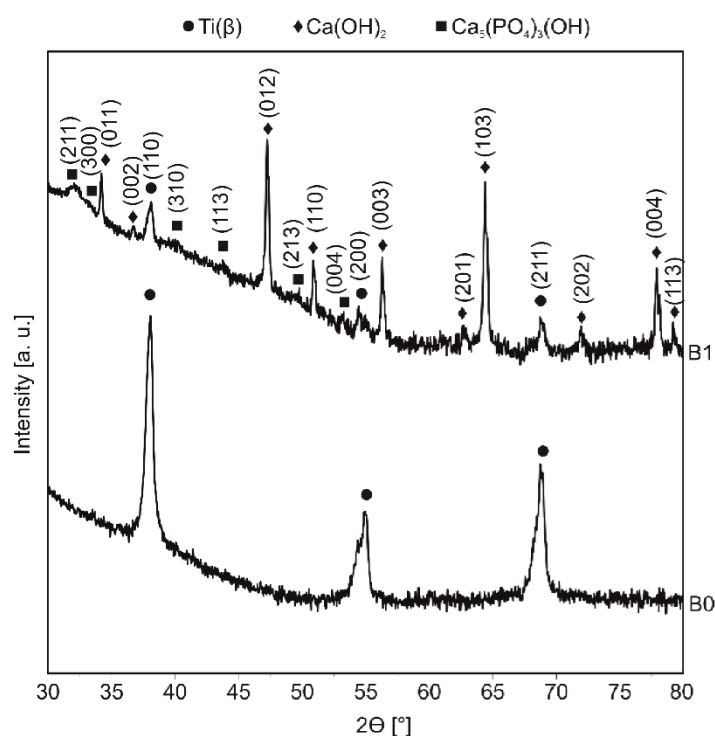
Figure 1. XRD spectra of Ti23Zr25Nb alloy electrochemically modified in 0.042M Ca(NO$_3$)$_2$ + 0.025M (NH$_4$)$_2$HPO$_4$ + 0.1M HCl bath with the voltage of −10 V and the time of 60 min (B1). The base Ti23Zr25Nb (B0) alloy was used as a reference material.

Moreover, the previously studied phase composition of biocomposites differs from the single-phase Ti23Zr25Nb alloy. Ti(α), Ti$_2$ZrO, and Nb$_5$Si$_3$P are other phases determining these materials' improved biological properties. The Ti(β) content is decreased to 65% with 9% 45S5 Bioglass content. Additionally,

its lattice constant is expanded to the 3.36–3.37 Å phase with 45S5 Bioglass and the content of Ag, Cu, and Zn [41].

Surface SEM images of Ti23Zr25Nb alloys after electrochemical etching at different magnifications are presented in Figure 2. The electrochemical etching allows the development of the Ti23Zr25Nb alloy surface, further improving the Ca and P ions' deposition to the material's surface during the next processing stage. Both pits and pores are visible in the presented micrograph.
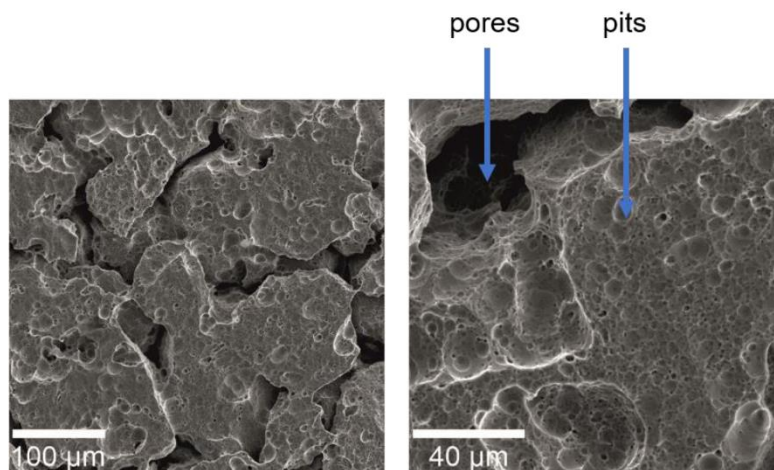

Figure 2. SEM micrographs of Ti23Zr25Nb alloy electrochemically etched in 1 M H_3PO_4 + 2% HF in the voltage of 10 V vs. OCP for 60 min (B1*) with different magnifications.

The morphology of coating obtained after deposition in 0.042M $Ca(NO_3)_2$ + 0.025M $(NH_4)_2HPO_4$ + 0.1 M HCl at −10 V vs. OCP voltage and 60 min, with EDS mapping, confirms the higher content of both calcium and phosphorous on the surface, forming the mixture of $Ca(OH)_2$ and $Ca_5(PO_4)_3(OH)$ complex presented in Figure 3. Additionally, the tilted-views with the estimated coating thickness close to 50 μm are provided in Figure 4.
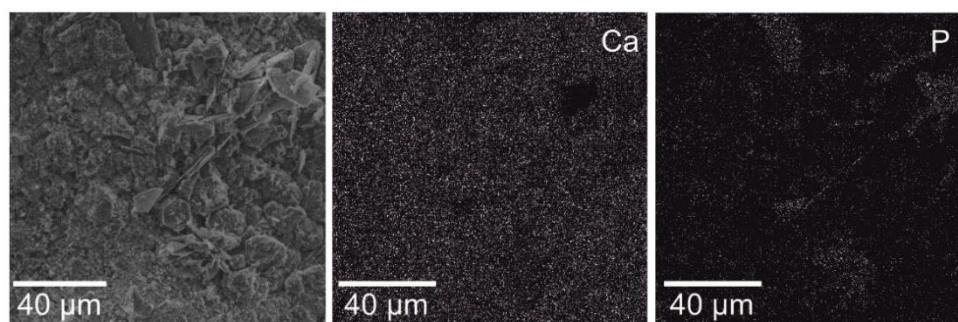
Figure 3. SEM micrographs, EDS mapping of the Ca and P distribution in the electrochemically modified Ti23Zr25Nb alloy in 0.042 M $Ca(NO_3)_2$ + 0.025 M $(NH_4)_2HPO_4$ + 0.1M HCl bath with the voltage of −10 V and the time of 60 min (B1).
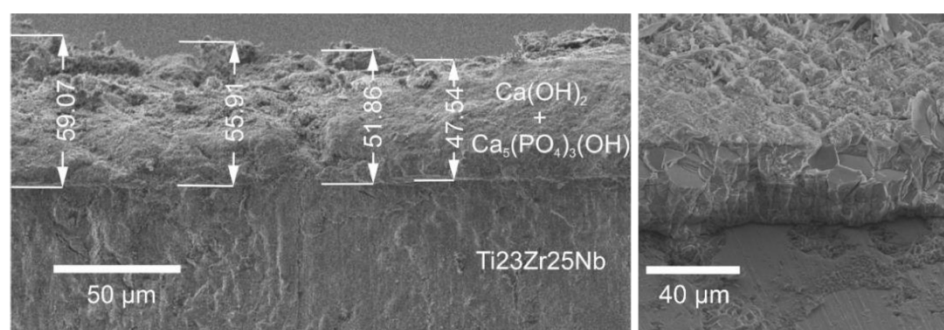
Figure 4. Tilted-views of Ti23Zr25Nb modified in 0.042M Ca(NO$_3$)$_2$ + 0.025M (NH$_4$)$_2$HPO$_4$ + 0.1 M HCl bath with the voltage of −10 V vs. OCP and the time of 60 min (B1) at 90 (on the left) and 51 (on the right) tilt angle.

3.2. Mechanical Properties

The mechanical properties of Ti23Zr25Nb alloys (as well as other TiZrNb alloys) and Ti23Zr25Nb-based composites were already studied in our previous work [41,42,54]. In Figure 5, the Young modulus was referenced to arc-melted Ti18Zr24Nb alloy and Ti23Zr25Nb foam. Ti23Zr25Nb alloys produced with hot pressing has a similar modulus [54] as a similar alloy made with conventional arc melting technology as the reference sample. The conventional method of samples consolidation in two stages, cold pressing and sintering, leads to a further limitation caused by the higher porosity of the produced sample [54]. Ti23Zr25Nb-9BG has been proven to have interesting mechanical properties with an elastic modulus equals to approximately 43 GPa [41], which is also lower than the elastic modulus of the Ti23Zr25 sample with 70% porosities produced with the use of ammonium bicarbonate (approximately 56 GPa). The limitation of the Young's modulus of TiZrNb and 45S5 Bioglass was done despite lower porosities of the so-produced materials. Both of these materials, Ti23Zr25Nb foam and the Ti23Zr25Nb-45S5 composite, seem to be in the same way interesting in terms of their mechanical properties. Their use in biomedical applications in terms of stress shielding effect limitation [55] is much more suitable than using the non-modified Ti23Zr25Nb alloy with the elastic modulus of approximately 70 GPa and 100 GPa for the cold-pressed and hot-pressed samples, respectively [54]. In both cases, the osseointegration process would be stimulated with the pores' presence in the produced materials. However, other technologies allow limiting these materials' modulus even further, such as the gel casting technique, which should be the object of further studies [56].
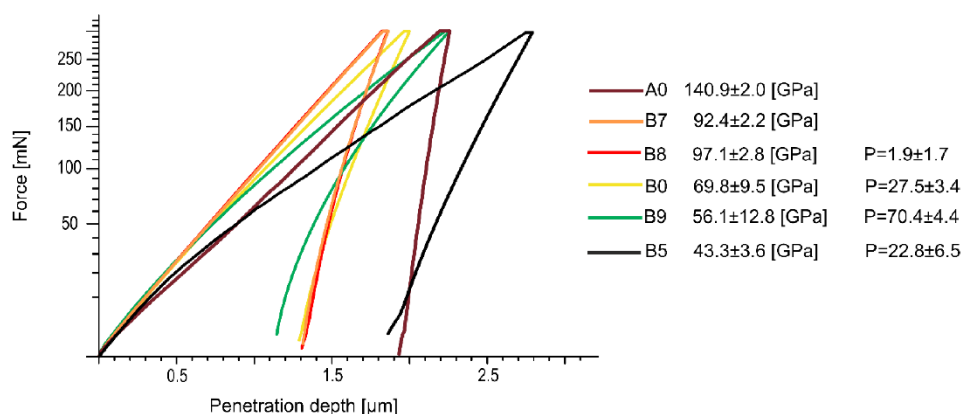
Figure 5. Nanoindentation load–depth curves of Ti23Zr25 alloys produced with hot pressing (B8), cold pressing with sintering (B0), as foams with ammonium bicarbonate (B9), and modified with 9% of 45S5 Bioglass addition (B5). Curves were contrasted with commercially pure Ti (A0) and microcrystalline arc-melted Ti18Zr24Nb (B7). The porosity results based on planimetric analysis (P) of each material were also provided.

3.3. Surface Properties

The surface roughness of the implant significantly influences cell attachments. Additionally, micro- and nanotopography has played a crucial role in cell proliferation [44,57]. The bulk Ti23Zr25Nb alloy's roughness before and after electrochemical modification are presented in Figure 6.
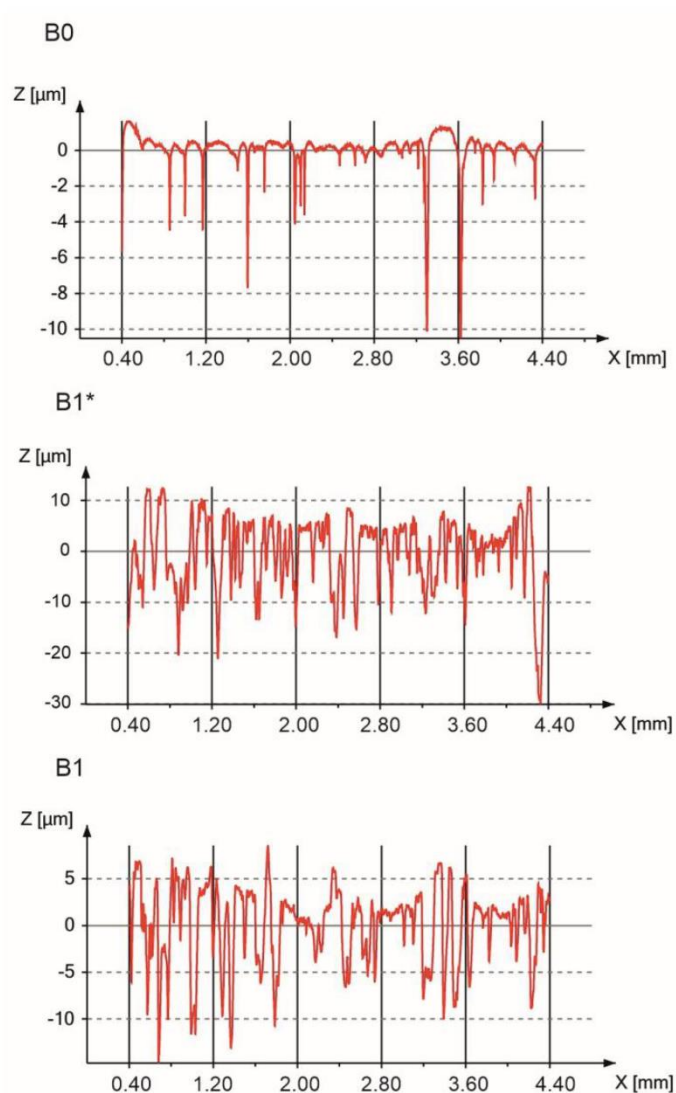
Figure 6. Roughness profiles of the bulk Ti23Zr25Nb alloy before etching (B0), after etching (B1*), and after etching with $Ca(OH)_2$ + $Ca_5(PO4)_3(OH)$ deposition (B1).

Ra, Rt, and Rz are equal to 0.56, 12.72, and 8.06 μm for the bulk non-modified sample, respectively (Table 1). Etching leads to the formation of the pores and numerous pits on the sample's surface, leading to the enhanced proliferation and growth of cells. During the etching process, large pores are formed on the surface of the sample.

Table 1. Two-dimensional (2D) (R_a, R_t, R_z) parameters for the Ti23Zr25Nb (at.%) on different processing routes.

Processing Route	R_a (μm)	R_t (μm)	R_z (μm)
B0—polished	0.56 ± 0.11	12.72 ± 1.33	8.06 ± 0.83
B1*	5.58 ± 0.14	39.08 ± 7.02	30.33 ± 4.38
B1	3.42 ± 1.04	27.36 ± 7.67	19.14 ± 4.98

3.4. Corrosion and Surface Wetting Properties

Several reports have shown that surface treatment methods can decrease Ti's corrosion rate in simulated body fluids [58,59]. The methods, including titanium plasma-spraying, grit-blasting, acid-etching, and anodization, or calcium phosphate deposition, can lead to coating with increased osteoconduction. The morphology and the properties of the so modified materials are reviewed by Guehennec et al. [58].

The corrosion resistance after electrochemical modification of the Ti23Zr25Nb alloy is improved (Figure 7). Electrochemical etching leads only to a slight decrease of the corrosion current, which is caused by the formation of some anodic oxides among the etching process previously observed after the same treatment of Ti foil [60] and mechanical alloyed Ti6Al4V alloy [61]. Further improvement is possible after the electrochemical deposition of calcium and phosphate-containing coatings consistent with other studies [62]. All of the potentiodynamic curves (Figure 7) reveal a clear passivation in the anodic part in the whole measurement range. However, better corrosion properties are possible with biocomposites containing 45S5 Bioglass formation, especially doped with silver. These composites were proven to improve the corrosion properties significantly (lower corrosion currents and corrosion potential). The corrosion currents of Ti23Zr25Nb-9BG and Ti23Zr25Nb-9BG-Ag are equal to about $10 \times 10^{-8} A/cm^2$ in contrast to $10 \times 10^{-7} A/cm^2$ for the $Ca(OH)_2 + Ca_5(PO4)_3(OH)$ coating [41].
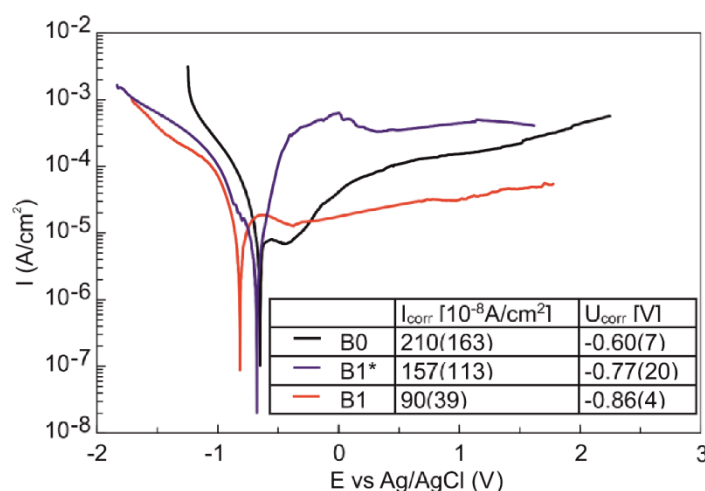
Figure 7. Potentiodynamic curves of Ti23Zr25Nb alloy after electrochemical etching (B1*) and electrochemical deposition (B1) in contrast to non-modified Ti23Zr25Nb alloy.

The surface free energy and contact angles for an electrochemically etched and deposited sample were significantly improved compared to the non-modified sample (Table 2). Surface free energy was increased to about 57–58 mN/m after both stages of surface modification. Contact angles were decreased to about 28–33° (for both modification stages) in the case of glycerol and about 48° (for electrochemical etching) and 12° (for electrochemical deposition) in the case of diiodomethane. It makes these materials more hydrophilic than before the modification, which is essential for bone tissue growth [63]. The composites' contact angles are equal to about 45–62° and 58–78° for diiodomethane and glycerol, respectively. The surface energy is equal to about 35–42 mN/m. These values are similar to that of non-modified Ti23Zr25Nb without vital improvement [41].

3.5. MTS Assay

NHost and HPdLF cultivated in the conditioned medium revealed various growth patterns, depending on the sample chemical composition and its microstructure modifications. Additionally, the time of culture influence the increase of the living cells. On the other hand, the growth rate was

differentiated between the different cultures (Figures 8 and 9). It is important to note that NHost comparing to HPdLF cells overgrow faster and more regularly on the tested materials.

Table 2. Surface free energy (SFE), dispersive and polar parts of SFE, diiodomethane, and glycerol contact angles for Ti23Zr25Nb alloy after electrochemical etching (B1*) and electrochemical deposition (B1) in contrast to non-modified Ti23Zr25Nb alloy (B0).

|	CA (M) Diiodomethane (°)	CA (M) Glycerol (°)	SFE (mN/m)	Disperse (mN/m)	Polar (mN/m)
B0	62.2 ± 9.0	64.6 ± 4.9	35.1 ± 10.0	27.4 ± 5.6	7.7 ± 4.4
B1*	47.6 ± 5.0	27.8 ± 5.9	56.5 ± 8.0	35.6 ± 2.9	20.9 ± 5.1
B1	11.6 ± 8.0	33.4 ± 10.2	58.4 ± 4.3	49.6 ± 1.2	8.8 ± 3.1
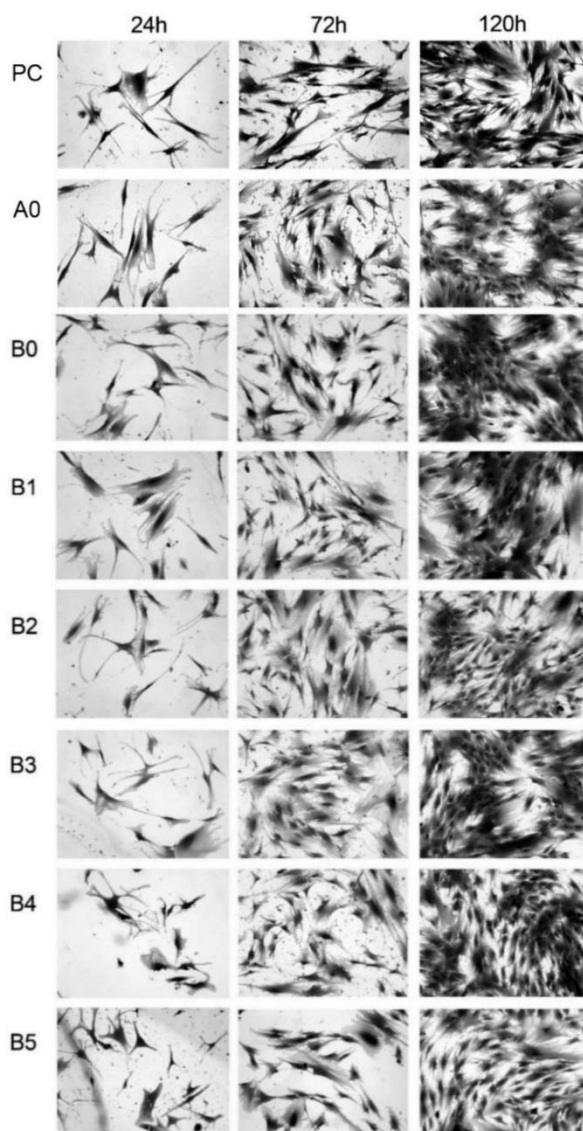
Figure 8. Morphology of the NHost cells cultured in different conditioned media for different times: 24, 72, and 120 h: positive control (PC), microcrystalline Ti (A0), ultrafine grained Ti23Zr25Nb alloy (B0), ultrafine grained Ti23Zr25Nb alloy electrochemically modified (B1) and Ti23Zr25Nb—9 wt.% 45S5 Bioglass (B2), Ti23Zr25Nb—9 wt.% 45S5 Bioglass—1 wt.% Ag (B3), Ti23Zr25Nb—9 wt.% 45S5 Bioglass—1 wt.% Cu (B4), Ti23Zr25Nb—9 wt.% 45S5 Bioglass—1 wt.% Zn (B5) composites.
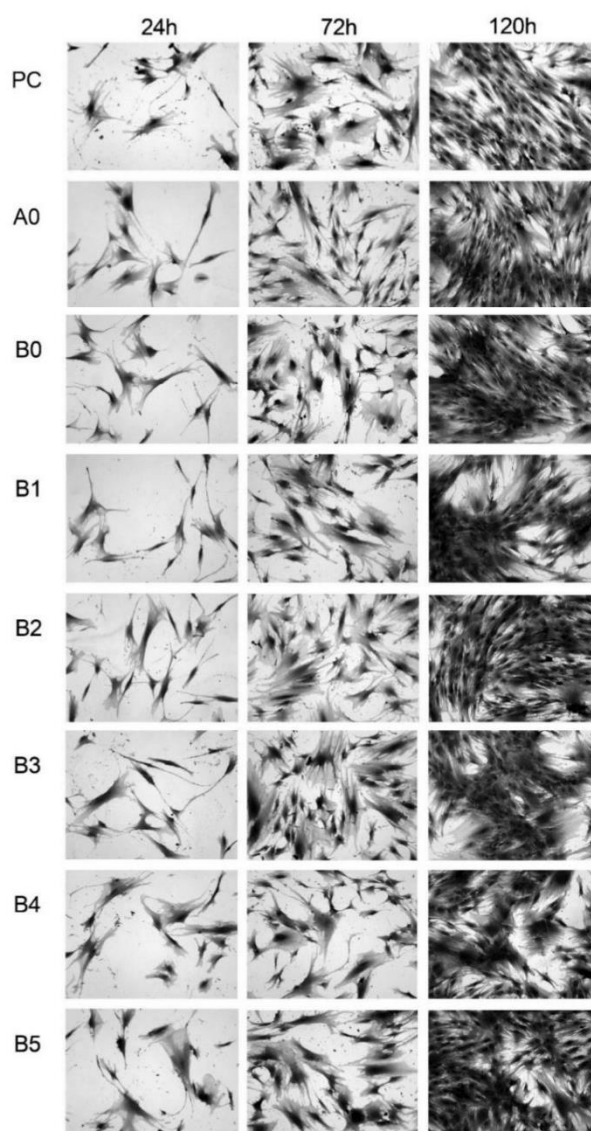
Figure 9. Morphology of the Human Periodontal Ligament Fibroblasts (HPdLF) cells cultured in different conditioned media for different times: 24, 72, and 120 h: positive control (PC), microcrystalline Ti (A0), ultrafine-grained Ti23Zr25Nb alloy (B0), ultrafine-grained Ti23Zr25Nb alloy electrochemically modified (B1), and Ti23Zr25Nb—9 wt.% 45S5 Bioglass (B2), Ti23Zr25Nb—9 wt.% 45S5 Bioglass—1 wt.% Ag (B3), Ti23Zr25Nb—9 wt.% 45S5 Bioglass—1 wt.% Cu (B4), Ti23Zr25Nb—9 wt.% 45S5 Bioglass—1 wt.% Zn (B5) composites.

The MTS assay is used to evaluate the cell proliferation, cell viability, and cytotoxicity of biomaterials. The reduction of the MTS tetrazolium compound by viable cells to generate a soluble in cell culture media colored formazan dye is the MTS assay base. MTS is more efficient than MTT and produces water-soluble formazan that does not require other additives such as DMSO. The quantity of dye product is measured by absorbance at 490 nm wavelength and is directly related to the number of metabolically active cells in culture. A commercial titanium rod was used as the growth control of the cells on the surface of the composite Ti23Zr25Nb—9 wt.% 45S5 Bioglass—type samples. In each culture, cells were grown three times directly on samples of the test materials for 24, 72, and 120 h. To control the natural spread of cells, they were grown directly on culture dishes in the plates without the tested material samples.

The rate of the viability of cells cultured directly on the surfaces of the studied materials is the measurement of the cytotoxicity of TZN-based materials. MTS results showed (Figures 10 and 11) a varying influence of the tested materials on the NHost and HPdLF cells' viability. Both types of cells showed reduced viability in comparison to the blank cultures. No cytotoxic effect of the samples had been perceived both on the commercial Ti rod and tested Ti23Zr25Nb alloy and composites. However, the intensity of the cell growth of fibroblasts and osteoblasts is heavily reliant on the composites' chemical composition and surface morphology. The experimental results show that the untreated as well as the electrochemically etched and $Ca(OH)_2 + Ca_5(PO4)_3(OH)$ deposited samples on the 5th day of cell proliferation exceeded the rate of the cell proliferation in the medium conditioned with microcrystalline Ti.
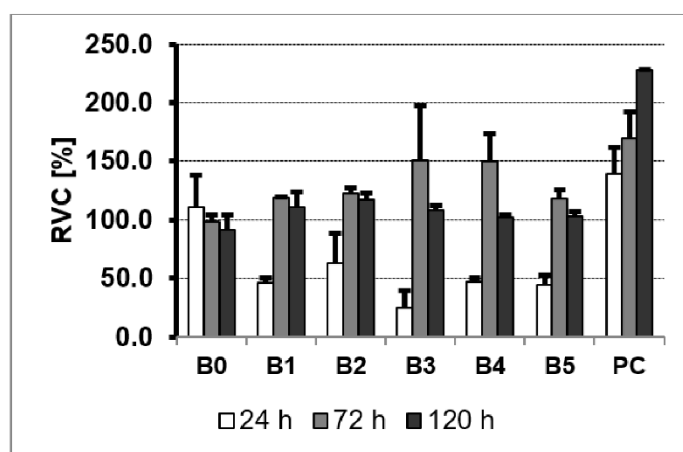
Figure 10. The results of the MTS assays performed at 24, 72, and 120 h on the viability of the NHost: ultrafine-grained Ti23Zr25Nb alloy (B0), ultrafine-grained Ti23Zr25Nb alloy electrochemically modified (B1) and Ti23Zr25Nb—9 wt.% 45S5 Bioglass (B2), Ti23Zr25Nb—9 wt.% 45S5 Bioglass—1 wt.% Ag (B3), Ti23Zr25Nb—9 wt.% 45S5 Bioglass—1 wt.% Cu (B4), Ti23Zr25Nb—9 wt.% 45S5 Bioglass—1 wt.% Zn (B5) composites; PC—positive control.
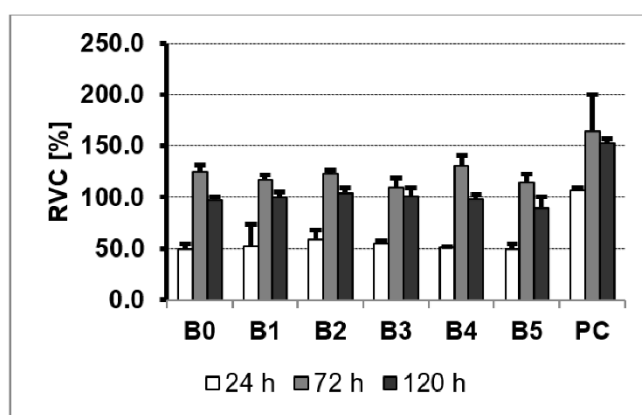
Figure 11. The results of the MTS assays performed at 24, 72, and 120 h on the viability of the HPdLF: ultrafine-grained Ti23Zr25Nb alloy (B0), ultrafine-grained Ti23Zr25Nb alloy electrochemically modified (B1), and Ti23Zr25Nb—9 wt.% 45S5 Bioglass (B2), Ti23Zr25Nb—9 wt.% 45S5 Bioglass—1 wt.% Ag (B3), Ti23Zr25Nb—9 wt.% 45S5 Bioglass—1 wt.% Cu (B4), Ti23Zr25Nb—9 wt.% 45S5 Bioglass—1 wt.% Zn (B5) composites; PC—positive control.

The proliferation of the fibroblasts and osteoblasts cells in conditioned mediums is expressed as a percent of the relative viability potential (RVC) value of the reference medium, conditioned with a CP-pure Ti sample. After 72 h, the proliferation of both cells in the media conditioned with

all tested samples exceeded the cell proliferation rate compared to the reference pure Ti specimen. Despite the natural diversities between the NHost and HPdLF cell lines, the tested cells showed similar RVC in contact with tested samples compared to the control. While the vitality rate of the cells cultured directly on the surface of the modified materials exceeded the vitality of the cells growing on Grade 2 Ti, particularly good results were observed for the B2 (Ti23Zr25Nb—9 wt.% 45S5 Bioglass), B3 (Ti23Zr25Nb—9 wt.% 45S5 Bioglass—1 wt.% Ag), B4 (Ti23Zr25Nb—9 wt.% 45S5 Bioglass—1 wt.% Cu) and B5 (Ti23Zr25Nb—9 wt.% 45S5 Bioglass—1 wt.% Zn) samples.

In our earlier study, the biocompatibility of the samples of anodized Ti modified with deposited Ag nanodendrites was investigated [64]. The assessment of fibroblasts and osteoblasts growth served as a model of the soft and hard tissue cells' performance in contact with the titanium-based materials. The results clearly show that the modification of titanium with silver improves the biocompatibility rate compared to untreated samples. A higher cell RVC was obtained for the cells cultured modified materials than for cells in contact with the control samples' surface. Modification of the titanium conducted with the anodic oxidation process at high voltages followed by the deposition of silver nanodendrites significantly changed the material's properties, leading to improved biocompatibility [64].

Silver possesses numerous benefits from the viewpoint of biomedical applications, such as good antibacterial properties, exceptional biocompatibility, and acceptable stability [65]. The addition of Ag into bioactive glasses composition has been studied by incorporating Ag ions into BG particles, which does not influence the biocompatibility of BG, but it improves the antibacterial properties of materials [66,67]. The addition of silver can also considerably decrease the bacterial *S. mutans* and *S. aureus* on the bulk Ti-10 wt.% 45S5 Bioglass-1.5 wt.% Ag surface compared to that on the pure Ti rod surface [68]. The antibacterial activity of TiMo–HA composite modified with silver, tantalum (V) oxide, or cerium (IV) oxide against *Staphylococcus aureus* was investigated. The composites modified with Ag and CeO_2 possess significantly lower adhesion levels of *S. aureus* ($p < 0.05$). In general, the Ag ions provide both bacteriostatic and bactericidal effects for the *E. coli* and Gram (+) and Gram (−) bacteria without harmful effects to the human cells [69].

The antibacterial effect of mechanically alloyed Ti23Zr25Nb-based composites was also evaluated. Produced materials doped with Ag, Cu, and Zn have promising high antibacterial activity against *S. mutans* [41]. Those properties among high biocompatibility make these materials attractive in use in the medical field of applications as dental implants.

4. Conclusions

In this work, novel ultrafine-grained Ti23Zr25Nb-based materials with 45S5 Bioglass and Ag, Cu, or Zn additions were produced through the combination of mechanical alloying and powder metallurgy. Additionally, Ti23Zr25Nb alloy was electrochemically modified in the two stages of processing: electrochemical etching in the solution of H_3PO_4 and HF followed by electrochemical deposition in $Ca(NO_3)_2$, $(NH_4)_2HPO_4$, and HCl. That studied possesses a Young modulus considerably lower than that of Grade 2 Ti. Furthermore, surface modification significantly improves the corrosion resistance and wettability properties. The biocompatibility MTS assays indicates that the bulk composites based on Ti23Zr25Nb and 45S5 Bioglass, with the addition of Ag, Cu, or Zn are suitable candidates for future dental and orthopedics implants.

Author Contributions: Conceptualization, M.J. and M.M.; Formal analysis, M.J., M.U.J. and M.M.; Funding acquisition, M.J.; Investigation, M.M., M.U.J., K.K., A.M., and P.K.W.; Supervision, M.J.; Writing—original draft, M.M.; Writing—review and editing, M.M., M.U.J., K.K., A.M., P.K.W. and M.J. All authors have read and agreed to the published version of the manuscript.

References

1. Bai, Y.; Deng, Y.; Zheng, Y.; Li, Y.; Zhang, R.; Lv, Y.; Zhao, Q.; Wei, S. Characterization, corrosion behavior, cellular response and in vivo bone tissue compatibility of titanium–niobium alloy with low Young's modulus. *Mater. Sci. Eng. C* **2016**, *59*, 565–576. [CrossRef]
2. Karre, R.; Kodli, B.K.; Rajendran, A.; Pattanayak, D.K.; Ameyama, K.; Dey, S.R.; Rajamallu, K.; Nivedhitha, J. Comparative study on Ti-Nb binary alloys fabricated through spark plasma sintering and conventional P/M routes for biomedical application. *Mater. Sci. Eng. C* **2018**, *94*, 619–627. [CrossRef]
3. Wang, B.L.; Li, L.; Zheng, Y.F. In vitro cytotoxicity and hemocompatibility studies of Ti-Nb, Ti-Nb-Zr and Ti-Nb-Hf biomedical shape memory alloys. *Biomed. Mater.* **2010**, *5*, 044102. [CrossRef]
4. Majumdar, P.; Singh, S.; Dhara, S.; Chakraborty, M. Influence of boron addition to Ti–13Zr–13Nb alloy on MG63 osteoblast cell viability and protein adsorption. *Mater. Sci. Eng. C* **2015**, *46*, 62–68. [CrossRef]
5. Cremasco, A.; Messias, A.D.; Esposito, A.R.; Duek, E.A.D.R.; Caram, R. Effects of alloying elements on the cytotoxic response of titanium alloys. *Mater. Sci. Eng. C* **2011**, *31*, 833–839. [CrossRef]
6. Neacsu, P.; Gordin, D.-M.; Mitran, V.; Gloriant, T.; Costache, M.; Cimpean, A. In vitro performance assessment of new beta Ti–Mo–Nb alloy compositions. *Mater. Sci. Eng. C* **2015**, *47*, 105–113. [CrossRef]
7. Guillemot, F.; Prima, F.; Bareille, R.; Gordin, D.-M.; Gloriant, T.; Durrieu, M.; Ansel, D.; Baquey, C. Design of new titanium alloys for orthopaedic applications. *Med Biol. Eng. Comput.* **2004**, *42*, 137–141. [CrossRef]
8. Haftlang, F.; Zarei-Hanzaki, A.; Abedi, H. The effect of nano-size second precipitates on the structure, apatite-inducing ability and in-vitro biocompatibility of Ti-29Nb-14Ta-4.5Zr alloy. *Mater. Sci. Eng. C* **2020**, *109*, 110561. [CrossRef] [PubMed]
9. Bărbînţă, A.C.; Earar, K.; Crimu, C.I.; DrĂgan, L.A.; Munteanu, C. In Vitro Evaluation of the Cytotoxicity of Some New Titanium Alloys. *Key Eng. Mater.* **2013**, *587*, 303–308. [CrossRef]
10. Rajan, S.T.; Bendavid, A.; Subramanian, B. Cytocompatibility assessment of Ti-Nb-Zr-Si thin film metallic glasses with enhanced osteoblast differentiation for biomedical applications. *Colloids Surf. B Biointerfaces* **2019**, *173*, 109–120. [CrossRef]
11. Kopova, I.; Stráský, J.; Harcuba, P.; Landa, M.; Janeček, M.; Bačáková, L. Newly developed Ti–Nb–Zr–Ta–Si–Fe biomedical beta titanium alloys with increased strength and enhanced biocompatibility. *Mater. Sci. Eng. C* **2016**, *60*, 230–238. [CrossRef] [PubMed]
12. Park, Y.-J.; Song, Y.-H.; An, J.-H.; Song, H.-J.; Anusavice, K.J. Cytocompatibility of pure metals and experimental binary titanium alloys for implant materials. *J. Dent.* **2013**, *41*, 1251–1258. [CrossRef] [PubMed]
13. Abbasi, S.P.; Bilesan, M.R.; Golestani-Fard, F. In vitro evaluation of the biocompatibility and bioactivity of plasma electrolyte oxidized titania/calcium phosphate nanocoatings on Ti. *J. Mater. Sci.* **2018**, *54*, 4277–4286. [CrossRef]
14. Liu, X.; Wu, L.; Ai, H.; Han, Y.; Hu, Y. Cytocompatibility and early osseointegration of nanoTiO2-modified Ti-24 Nb-4 Zr-7.9 Sn surfaces. *Mater. Sci. Eng. C* **2015**, *48*, 256–262. [CrossRef] [PubMed]
15. Ansar, E.; Ravikumar, K.; Babu, S.S.; Fernandez, F.; Komath, M.; Basu, B.; Varma, H. Inducing apatite pre-layer on titanium surface through hydrothermal processing for osseointegration. *Mater. Sci. Eng. C* **2019**, *105*, 110019. [CrossRef]
16. Sedelnikova, M.B.; Komarova, E.G.; Sharkeev, Y.P.; Ugodchikova, A.V.; Tolkacheva, T.V.; Rau, J.V.; Buyko, E.E.; Ivanov, V.V.; Sheikin, V.V. Modification of titanium surface via Ag-, Sr- and Si-containing micro-arc calcium phosphate coating. *Bioact. Mater.* **2019**, *4*, 224–235. [CrossRef]
17. Furko, M.; Della Bella, E.; Fini, M.; Balázsi, K. Corrosion and biocompatibility examination of multi-element modified calcium phosphate bioceramic layers. *Mater. Sci. Eng. C* **2019**, *95*, 381–388. [CrossRef]
18. Türk, S.; Altınsoy, I.; Efe Çelebi, G.; Ipek, M.; Özacar, M.; Bindal, C. Biomimetic synthesis of Ag, Zn or Co doped HA and coating of Ag, Zn or Co doped HA/fMWCNT composite on functionalized Ti. *Mater. Sci. Eng. C* **2019**, *99*, 986–998. [CrossRef]
19. Lenis, J.; Toro, L.; Bolívar, F. Multi-layer bactericidal silver-calcium phosphate coatings obtained by RF magnetron sputtering. *Surf. Coat. Technol.* **2019**, *367*, 203–211. [CrossRef]
20. He, Y.; Zhang, Y.; Meng, Z.; Jiang, Y.; Zhou, R. Microstructure evolution, mechanical properties and enhanced bioactivity of Ti-Nb-Zr based biocomposite by bioactive calcium pyrophosphate. *J. Alloys Compd.* **2017**, *720*, 567–581. [CrossRef]

21. Wang, X.; Chen, Y.; Xu, L.; Liu, Z.; Woo, K.-D. Effects of Sn content on the microstructure, mechanical properties and biocompatibility of Ti–Nb–Sn/hydroxyapatite biocomposites synthesized by powder metallurgy. *Mater. Des.* **2013**, *49*, 511–519. [CrossRef]

22. Rodrigues, C.; Naasani, L.I.S.; Zanatelli, C.; Paim, T.C.; Azevedo, J.G.; De Lima, J.C.; Fernandes, M.D.C.; Buchner, S.; Wink, M. Bioglass 45S5: Structural characterization of short range order and analysis of biocompatibility with adipose-derived mesenchymal stromal cells in vitro and in vivo. *Mater. Sci. Eng. C* **2019**, *103*, 109781. [CrossRef] [PubMed]

23. De Souza, L.P.L.; Lopes, J.H.; Ferreira, F.; Martin, R.A.; Bertran, C.A.; Camilli, J.A. Evaluation of effectiveness of 45S5 bioglass doped with niobium for repairing critical-sized bone defect in in vitro and in vivo models. *J. Biomed. Mater. Res. Part A* **2019**, *108*, 446–457. [CrossRef] [PubMed]

24. Lopes, J.H.; Souza, L.; Domingues, J.A.; Ferreira, F.; Hausen, M.D.A.; Camilli, J.A.; Martin, R.A.; Duek, E.A.D.R.; Mazali, I.O.; Bertran, C.A. In vitro and in vivo osteogenic potential of niobium-doped 45S5 bioactive glass: A comparative study. *J. Biomed. Mater. Res. Part B Appl. Biomater.* **2020**, *108*, 1372–1387. [CrossRef]

25. Karakuzu-Ikizler, B.; Terzioğlu, P.; Oduncu-Tekerek, B.S.; Yucel, S. Effect of selenium incorporation on the structure and in vitro bioactivity of 45S5 bioglass. *J. Aust. Ceram. Soc.* **2019**, *56*, 697–709. [CrossRef]

26. Dittler, M.L.; Unalan, I.; Grünewald, A.; Beltrán, A.M.; Grillo, C.A.; Destch, R.; Gonzalez, M.C.; Boccaccini, A.R. Bioactive glass (45S5)-based 3D scaffolds coated with magnesium and zinc-loaded hydroxyapatite nanoparticles for tissue engineering applications. *Colloids Surf. B Biointerfaces* **2019**, *182*, 110346. [CrossRef]

27. Eshghinejad, P.; Farnoush, H.; Bahrami, M.S.; Bakhsheshi-Rad, H.R.; Karamian, E.; Chen, X. Electrophoretic deposition of bioglass/graphene oxide composite on Ti-alloy implants for improved antibacterial and cytocompatible properties. *Mater. Technol.* **2019**, *35*, 69–74. [CrossRef]

28. Shaikh, S.; Kedia, S.; Majumdar, A.G.; Subramanian, M.; Sinha, S. 45S5 bioactive glass coating on Ti6Al4V alloy using pulsed laser deposition technique. *Mater. Res. Express* **2020**, *6*, 125428. [CrossRef]

29. Kaczmarek, M.; Jurczyk, M.; Rubis, B.; Banaszak, A.; Kolecka, A.; Paszel, A.; Jurczyk, K.; Murias, M.; Sikora, J. In vitrobiocompatibility of Ti-45S5 bioglass nanocomposites and their scaffolds. *J. Biomed. Mater. Res. Part A* **2013**, *102*, 1316–1324. [CrossRef]

30. Saxena, V.; Kumar, V.; Singh, A.; Singh, V.K.; Singh, A. Effect of reinforcing S53P4 bioactive glass on physio-mechanical and biological properties of Ti –8Nb–2Fe alloy. *Ceram. Int.* **2019**, *45*, 21810–21818. [CrossRef]

31. Kowalski, K.; Jurczyk, M.; Wirstlein, P.; Jakubowicz, J. Influence of 45S5 Bioglass addition on microstructure and properties of ultrafine grained (Mg-4Y-5.5Dy-0.5Zr) alloy. *Mater. Sci. Eng. B* **2017**, *219*, 28–36. [CrossRef]

32. Kowalski, K.; Jurczyk, M.U.; Wirstlein, P.K.; Jakubowicz, J.; Jurczyk, M. Properties of ultrafine-grained Mg-based composites modified by addition of silver and hydroxyapatite. *Mater. Sci. Technol.* **2018**, *34*, 1096–1103. [CrossRef]

33. Moseke, C.; Braun, W.; Ewald, A. Electrochemically Deposited Ca(OH)$_2$Coatings as a Bactericidal and Osteointegrative Modification of Ti Implants. *Adv. Eng. Mater.* **2009**, *11*, B1–B6. [CrossRef]

34. Han, G.Y.; Park, S.H.; Yoon, T.C. Antimicrobial Activity of Ca(OH)$_2$ Containing Pastes with Enterococcus faecalis In Vitro. *J. Endod.* **2001**, *27*, 328–332. [CrossRef]

35. Liu, K.; Zhang, H.; Lu, M.; Liu, L.; Yan, Y.; Chu, Z.; Ge, Y.; Wang, T.; Tang, C. Enhanced bioactive and osteogenic activities of titanium by modification with phytic acid and calcium hydroxide. *Appl. Surf. Sci.* **2019**, *478*, 162–175. [CrossRef]

36. Kim, D.G.; Woo, K.D.; Kang, D.S.; Lee, T.; Lee, M.H. Fabrication and biocompatibility evaluation of porous Ti-Nb-based biomaterials with space holder by rapid sintering. *Mater. Res. Innov.* **2015**, *19*, S1-301. [CrossRef]

37. Xu, J.; Weng, X.-J.; Wang, X.; Huang, J.-Z.; Zhang, C.; Muhammad, H.; Ma, X.; Liao, Q.-D. Potential Use of Porous Titanium–Niobium Alloy in Orthopedic Implants: Preparation and Experimental Study of Its Biocompatibility In Vitro. *PLoS ONE* **2013**, *8*, e79289. [CrossRef]

38. Ruan, J.; Yang, H.; Weng, X.; Miao, J.; Zhou, K. Preparation and characterization of biomedical highly porous Ti–Nb alloy. *J. Mater. Sci. Mater. Med.* **2016**, *27*, 1–8. [CrossRef]

39. Prakash, C.; Singh, S.; Ramakrishna, S.; Królczyk, G.; Le, C.H. Microwave sintering of porous Ti–Nb-HA composite with high strength and enhanced bioactivity for implant applications. *J. Alloys Compd.* **2020**, *824*, 153774. [CrossRef]

40. Tao, X.; Li, S.; Zheng, C.; Fu, J.; Guo, Z.; Hao, Y.; Yang, R.; Guo, Z. Synthesis of a porous oxide layer on a multifunctional biomedical titanium by micro-arc oxidation. *Mater. Sci. Eng. C* **2009**, *29*, 1923–1934. [CrossRef]

41. Marczewski, M.; Jurczyk, M.; Pecyna, P.; Ratajczak, M.; Gajecka, M.; Jurczyk, M. The Effect of 45S5 Bioglass and Ag, Cu, or Zn Addition on the Crystal Structure, Properties, and Antibacterial Effect of Bulk Ti23Zr25Nb Biocomposites. *Metals* **2020**, *10*, 1115. [CrossRef]

42. Marczewski, M.; Miklaszewski, A.; Maeder, X.; Jurczyk, M. Crystal Structure Evolution, Microstructure Formation, and Properties of Mechanically Alloyed Ultrafine-Grained Ti-Zr-Nb Alloys at 36 ≤ Ti ≤ 70 (at.%). *Materials* **2020**, *13*, 587. [CrossRef] [PubMed]

43. Eisenbarth, E.; Velten, D.; Müller, M.; Thull, R.; Breme, J. Biocompatibility of β-stabilizing elements of titanium alloys. *Biomaterials* **2004**, *25*, 5705–5713. [CrossRef] [PubMed]

44. Webster, T.J.; Ejiofor, J.U. Increased osteoblast adhesion on nanophase metals: Ti, Ti6Al4V, and CoCrMo. *Biomaterials* **2004**, *25*, 4731–4739. [CrossRef] [PubMed]

45. Allaker, R.; Ren, G.G. Potential impact of nanotechnology on the control of infectious diseases. *Trans. R. Soc. Trop. Med. Hyg.* **2008**, *102*, 1–2. [CrossRef]

46. Bürgers, R.; Hahnel, S.; Reichert, T.E.; Rosentritt, M.; Behr, M.; Gerlach, T.; Handel, G.; Gosau, M. Adhesion of Candida albicans to various dental implant surfaces and the influence of salivary pellicle proteins. *Acta Biomater.* **2010**, *6*, 2307–2313. [CrossRef]

47. García-Contreras, R.; Argueta-Figueroa, L.; Mejía-Rubalcava, C.; Jiménez-Martínez, R.; Cuevas-Guajardo, S.; Sánchez-Reyna, P.A.; Mendieta-Zeron, H. Perspectives for the use of silver nanoparticles in dental practice. *Int. Dent. J.* **2011**, *61*, 297–301. [CrossRef]

48. Apostu, D.; Lucaciu, P.; Berce, C.; Lucaciu, D.; Cosma, D. Current methods of preventing aseptic loosening and improving osseointegration of titanium implants in cementless total hip arthroplasty: A review. *J. Int. Med. Res.* **2017**, *46*, 2104–2119. [CrossRef]

49. *ISO 25178-2:2012. Geometrical Product Specifications (GPS)—Surface Texture: Areal—Part 2: Terms, Definitions and Surface Texture Parameters*; International Organization for Standardization: Geneva, Switzerland, 2012.

50. Fitzgibbon, A.; Pilu, M.; Fisher, R.B. Direct least square fitting of ellipses. *IEEE Trans. Pattern Anal. Mach. Intell.* **1999**, *21*, 476–480. [CrossRef]

51. Kaelble, D.H. Dispersion-Polar Surface Tension Properties of Organic Solids. *J. Adhes.* **1970**, *2*, 66–81. [CrossRef]

52. Owens, D.K.; Wendt, R.C. Estimation of the surface free energy of polymers. *J. Appl. Polym. Sci.* **1969**, *13*, 1741–1747. [CrossRef]

53. Oliver, W.; Pharr, G. An improved technique for determining hardness and elastic modulus using load and displacement sensing indentation experiments. *J. Mater. Res.* **1992**, *7*, 1564–1583. [CrossRef]

54. Marczewski, M.; Miklaszewski, A.; Jurczyk, M. Structure evolution analysis in ultrafine-grained Zr and Nb-based beta titanium alloys. *J. Alloys Compd.* **2018**, *765*, 459–469. [CrossRef]

55. Nagels, J.; Stokdijk, M.; Rozing, P.M. Stress shielding and bone resorption in shoulder arthroplasty. *J. Shoulder Elb. Surg.* **2003**, *12*, 35–39. [CrossRef] [PubMed]

56. Yang, D.; Guo, Z.; Shao, H.; Liu, X.; Ji, Y. Mechanical Properties of Porous Ti-Mo and Ti-Nb Alloys for Biomedical Application by Gelcasting. *Procedia Eng.* **2012**, *36*, 160–167. [CrossRef]

57. Ward, B.C.; Webster, T.J. Increased functions of osteoblasts on nanophase metals. *Mater. Sci. Eng. C* **2007**, *27*, 575–578. [CrossRef]

58. Le Guéhennec, L.; Soueidan, A.; Layrolle, P.; Amouriq, Y. Surface treatments of titanium dental implants for rapid osseointegration. *Dent. Mater.* **2007**, *23*, 844–854. [CrossRef]

59. Kaluđerović, M.R.; Schreckenbach, J.P.; Graf, H.-L. Titanium dental implant surfaces obtained by anodic spark deposition—From the past to the future. *Mater. Sci. Eng. C* **2016**, *69*, 1429–1441. [CrossRef]

60. Jakubowicz, J. Formation of porous TiOx biomaterials in H3PO4 electrolytes. *Electrochem. Commun.* **2008**, *10*, 735–739. [CrossRef]

61. Jakubowicz, J.; Adamek, G. Preparation and properties of mechanically alloyed and electrochemically etched porous Ti–6Al–4V. *Electrochem. Commun.* **2009**, *11*, 1772–1775. [CrossRef]

62. Jakubowicz, J. Deposition and properties of hydroxyapatite on flat and porous Ti. *Eur. Cells Mater.* **2010**, *19*, 2.

63. Thevenot, P.; Hu, W. Surface Chemistry Influences Implant Biocompatibility. *Curr. Top. Med. Chem.* **2008**, *8*, 270–280. [CrossRef] [PubMed]

64. Kaczmarek, M.; Jurczyk, K.; Koper, J.K.; Paszel-Jaworska, A.; Romaniuk, A.; Lipińska, N.; Żurawski, J.; Urbaniak, P.; Jakubowicz, J.; Jurczyk, M.U. In vitro biocompatibility of anodized titanium with deposited silver nanodendrites. *J. Mater. Sci.* **2016**, *51*, 5259–5270. [CrossRef]

65. Yin, I.X.; Zhang, J.; Zhao, I.S.; Mei, M.L.; Li, Q.; Chu, C.H. The Antibacterial Mechanism of Silver Nanoparticles and Its Application in Dentistry. *Int. J. Nanomed.* **2020**, *15*, 2555–2562. [CrossRef] [PubMed]

66. Zhu, H.; Hu, C.; Zhang, F.; Feng, X.; Li, J.; Liu, T.; Chen, J.; Zhang, J. Preparation and antibacterial property of silver-containing mesoporous 58S bioactive glass. *Mater. Sci. Eng. C* **2014**, *42*, 22–30. [CrossRef] [PubMed]

67. Kozon, D.; Zheng, K.; Boccardi, E.; Liu, Y.; Liverani, L.; Boccaccini, A.R. Synthesis of Monodispersed Ag-Doped Bioactive Glass Nanoparticles via Surface Modification. *Materials* **2016**, *9*, 225. [CrossRef] [PubMed]

68. Jurczyk, K.; Kubicka, M.; Ratajczak, M.; Jurczyk, M.; Niespodziana, K.; Nowak, D.; Gajecka, M. Antibacterial activity of nanostructured Ti–45S5 bioglass–Ag composite against Streptococcus mutans and Staphylococcus aureus. *Trans. Nonferrous Met. Soc. China* **2016**, *26*, 118–125. [CrossRef]

69. Sochacka, P.; Miklaszewski, A.; Jurczyk, M.; Pecyna, P.; Ratajczak, M.; Gajecka, M. Effect of hydroxyapatite and Ag, Ta_2O_5 or CeO_2 addition on the properties of ultrafine-grained Ti31Mo alloy. *J. Alloys Compd.* **2020**, *823*, 153749. [CrossRef]

Artykuł nr 4:

M. Marczewski, M. Jurczyk, P. Pecyna,

M. Ratajczak, M. Gajecka, M.U. Jurczyk,

The Effect of 45S5 Bioglass and Ag, Cu, or Zn

Addition on the Crystal Structure, Properties, and

Antibacterial Effect of Bulk Ti23Zr25Nb

Biocomposites

The Effect of 45S5 Bioglass and Ag, Cu, or Zn Addition on the Crystal Structure, Properties, and Antibacterial Effect of Bulk Ti23Zr25Nb Biocomposites

**M. Marczewski** [1] [iD], **M. Jurczyk** [1,*] [iD], **P. Pecyna** [2] [iD], **M. Ratajczak** [2] [iD], **M. Gajecka** [2,3] [iD] and **M. U. Jurczyk** [4] [iD]

1   Institute of Materials Science and Engineering, Poznan University of Technology, Jana Pawla II 24, 61-138 Poznan, Poland; mateusz.p.marczewski@doctorate.put.poznan.pl
2   Faculty of Pharmacy, Department of Genetics and Pharmaceutical Microbiology, Poznan University of Medical Sciences, Swiecickiego 4, 60-781 Poznan, Poland; pa.pecyna@gmail.com (P.P.); ratajczak.magdalena@wp.pl (M.R.); gamar@man.poznan.pl (M.G.)
3   Institute of Human Genetics, Polish Academy of Sciences, Strzeszynska 32, 60-479 Poznan, Poland
4   Division of Mother's and Child's Health, Poznan University of Medical Sciences, Polna 33, 60-535 Poznan, Poland; mjur@poczta.onet.pl
*   Correspondence: mieczyslaw.jurczyk@put.poznan.pl; Tel.: +48-61-665-3508

Abstract: In the present study, the crystal structure, microstructure, mechanical, corrosion properties, and wettability of bulk Ti23Zr25Nb-x45S5 Bioglass (x = 0, 3, 6, 9 wt.%) and Ti23Zr25Nb—9 wt.% 45S5 Bioglass composites with the addition of 1 wt.% Ag, Cu, or Zn were synthesized and their properties studied. The hardness of these biomaterials is at least two times higher and the elastic modulus lower in comparison to commercial purity (CP) microcrystalline α-Ti. The mechanically alloyed Ti23Zr25Nb—9 wt.% 45S5 Bioglass composite was more corrosion resistant in Ringer's solution than the bulk Ti23Zr25Nb alloy. Surface wettability measurements revealed the higher surface hydrophilicity of the bulk synthesized composites. The antibacterial activity of Ti23Zr25Nb-based composites containing silver, copper, or zinc against reference strain *Streptococcus mutans* ATCC 25175 was studied. In vitro bacterial adhesion indicated a significantly reduced number of *S. mutans* on the bulk Ti23Zr25Nb-BG-Ag (or Cu, Zn) plate surfaces in comparison to the microcrystalline Ti plate surface. Ultrafine-grained Ti23Zr25Nb-BG-Ag (or Cu, Zn) biomaterials can be considered to be the next generation of dental implants.

Keywords: Ti-Zr-Nb alloy; 45S5 Bioglass; mechanical alloying; structural properties; antibacterial activity; *S. mutans*

1. Introduction

Beta-type titanium alloys are an interesting group of biomaterials. Mechanical alloying is the technology of producing them with much smaller grain sizes than conventional methods such as arc melting. The structure evolution of titanium-based alloys with different beta-stabilizers (Nb, Zr, and Mo) produced with mechanical alloying has been already examined [1,2]. These alloys were described as really interesting in terms of their properties such as the Young modulus. Moreover, further modification leads to their improvement, including better corrosion resistance [3].

Particular interest should be focused on modifying these alloys by the formation of biocomposite materials. That allows us to decrease their Young modulus, increase the corrosion resistance, and antibacterial properties. Biocomposites formed by adding 45S5 Bioglass to these alloys during milling can lead to interesting results such as higher biocompatibility, hardness, and a lower Young modulus.

Moreover, Ag content increases the antibacterial behavior of alloys and the formation of foams improves the osteointegration process [4,5].

Modification of titanium alloys with bioglass and bioglass-reinforced composites was also done with surface engineering methods as electrophoretic deposition (EPD) [6–13], magnetron sputtering [14,15], pulsed electron deposition [16] and plasma spraying [17]. Hydroxyapatite and bioglass co-coatings produced with laser engineering net shaping (LENS) should also be a matter of scientific interest because of their promising corrosion resistance, wear-resistance, and interaction with bone cells [18]. A potential medical application has also been documented with an anodic bonding method of titanium with 52S4.6 and 45S5 Bioglasses [19]. Electrophoretically deposited films also showed good properties on a non-titanium alloy like stainless steel and Nitinols [20]. The nanobioglass composited with silver [21], metal oxides such as TiO_2 [22], and graphene oxides [23,24] was done with the use of the sol–gel technique. Depending on the modification technique, the properties of bioglass can be significantly improved in terms of their bioactivity, hemocompatibility, antibacterial activity, and cell proliferation properties.

The Zn addition was proved to have antibacterial properties in the coatings, either as an implanted ion with plasma immersion technology [25] or as a doping element for the calcium phosphates films [26–28]. Zn is also successfully added to the coatings with other antibacterial elements such as Ag [29].

Ti-Cu alloys with high antibacterial properties were also produced. In these alloys, the crucial factor is not only the Cu content but also precipitation of the Ti_2Cu phase with the best effect achieved with the homogenous fine precipitate. The Cu addition also leads to the hardening effect of these alloys. According to most of the research, at least 5 wt% of Cu is needed to have the right antibacterial effect against some of the well-known bacteria: *Escherichia coli*, *Staphylococcus aureus*, *Streptococcus mutans* and *Porphyromonas gingivalis* [30–39]. Copper can also be successfully added to non-titanium alloys such as steels, magnesium alloys, cobalt alloys, and zinc alloys. Its addition not only allows the use of the antibacterial properties of that element but also improves its corrosion resistance and mechanical properties [40].

Ti-Ag alloys are also a matter of great importance for the development of materials with antibacterial ability. As in Ti-Cu alloys, the intermetallic Ti_2Ag phase is crucial and its homogenous and nano-scale precipitation could improve their antibacterial properties [41,42]. Silver containing bioglass nanoparticles (AgBGs) produced with the sol–gel method were also created. This type of particle could also be interesting in terms of bioactivity and the antibacterial improvement in the biomedical field of applications [43]. Producing of antibacterial alloys containing silver is a deeply examined topic in biomedical science. Titanium alloys are not the only modified materials with this additive. One of the newest examples of using silver in material engineering is the antibacterial, biodegradable Fe-Mn-Ag alloy [44].

Surface engineering of implants is relevant for safeguarding them against the formation of bacterial biofilms. The use of Zn, Cu, Ag (ion-implanted, etc.), is the selected way of doing that [45,46].

In this work, the ultrafine-grained Ti23Zr25Nb alloy and its composites with 45S5 Bioglass as well as with Ag, Cu, or Zn were synthesized by the application of mechanical alloying and powder metallurgy. As was mentioned in the previous articles considering the production of beta-type Ti-based alloys this method is seen as the most useful in contrast to the conventional ones. It allows the production of ultra-fine grained beta-type titanium alloys in a wide range of the concentrations and with the use of the elements with significantly different melting points [1,2,47]. Grain refinement can lead to further improvement of properties and increased hardness. Mechanically alloyed materials were also proven to have better biological properties [48,49].

The reason for the modification with 45S5 Bioglass was to improve the properties which would lower the Young modulus and improve the corrosion resistance of the non-modified Ti23Zr25Nb alloy. Its corrosion resistance has been revealed as worse than that of microcrystalline titanium in our previous work [47]. This type of bioglass provides good cell growth and differentiation of

osteoblasts due to the low phosphate content and the widest clinical application among all other bioglasses [50,51]. The addition of well-known elements with antibacterial properties such as Ag, Cu, and Zn was to enhance the antibacterial response of the material, which should make the produced material interesting for use in the biomedical field. The influence of the microstructure and chemical composition of Ti23Zr25Nb and Ti23Zr25Nb-BG-Ag (or Cu, Zn) composites on the crystal structure, microstructure, mechanical properties, corrosion behavior, surface wettability, and antibacterial activity against a reference strain of *Streptococcus mutans* were investigated in detail.

2. Materials and Methods

2.1. Sample Preparation

Mechanical alloying was done with a SPEX 8000 Mixer Mill (SPEX® Sample Prep, Metuchen, NJ, USA) and round bottom stainless vials. To produce the alloy, the composites vials was filled in the Ar atmosphere inside a glove box Labmaster 130 (MBraun, Garching, Germany) with following precursors: Ti (Alfa Aesar, 99.9% purity, <45 μm average particle size, CAS: 7440-32-6), Nb (Sigma Aldrich, 99.8% purity, <45 μm average particle size, CAS: 7440-03-1), 45S5 Bioglass (Mo-Sci GL0160P; 53 μm average particle size, 45% SiO_2, 24.5% Na_2O, 24.5 CaO, 6% P_2O_5), Ag (Alfa Aesar, 99.9% purity, 4–7 μm particle size, CAS: 7440-22-4) powders, Zn (Sigma Aldrich, 99% purity, 30–100 mesh, CAS: 7440-66-6) granules, Cu (Sigma Aldrich, 99% purity, CAS: 7440-50-8) turnings, and Zr fillings from a sponge (Sigma Aldrich, ≥99%, CAS: 7440-50-8). The experiments were carried out on 6 different Ti23Zr25Nb (at.%)-based composites. 45S5 Bioglass composition was varied from 3 to 9 wt.% (to alloy powder ratio). The composite with 9 wt.% content of 45S5 Bioglass was additionally doped with 1 wt.% (to 45S5 Bioglass composite powder ratio) of 3 antibacterial elements (Ag, Zn, Cu). The content of antimicrobial elements was chosen to be as low as possible to introduce the antibacterial properties with as small an impact possible on the other properties such as its biocompatibility and limitation of the additional ions release. Mechanical alloying for all composites was carried out for 16 h. Mechanically alloyed powders were consolidated with conventional cold compaction and sintering. All of the samples were consolidated with the same process parameters. Cold compaction pressure was equal to 600 MPa. Sintering was conducted in an 800 °C temperature for 30 min (allowing the consolidation of the powders with not too much grain growth) and followed with fast water cooling in a quartz tube filled with Ar. The temperature choice was based on previous research of the Ti-Zr-Nb alloys and also Ti-Mo alloys, which proves the increase in β-phase content in most of these types of materials with increase in temperature. Moreover, the highest possible temperature at which it was possible to achieve a fully single β-phase structure in Ti23Zr25Nb (at.%) alloy was 800 °C, which was chosen as the most suitable [2,47]. Bulk sample dimensions were 6 mm diameter and 4 mm in height. The schematic representation of the mechanism behind the mechanical alloying of biocomposites is presented in Figure 1. Additionally, the summarization of mass ratios of precursors and optimization parameters is presented in Table 1.

Table 1. The mass ratios of output precursors and optimization parameters for preparation of the studied Ti23Zr25Nb–based biocomposites (TNZ—Ti23Zr25Nb (at.%) alloy [1,47]; BG—45S5 Bioglass; AB—antibacterial additive; T—milling time; CP—compaction pressure; S—sintering temperature).

Material	BG/TNZ [%]	AB/TNZ-BG [%]	T [h]	CP [MPa]	S [°C]
Ti23Zr25Nb-3BG	3	-			
Ti23Zr25Nb-6BG	6	-			
Ti23Zr25Nb-9BG	9	-	16	600	800
T23Zr25Nb-9B-Ag	9	1			
T23Zr25Nb-9B-Cu	9	1			
T23Zr25Nb-9B-Zn	9	1			
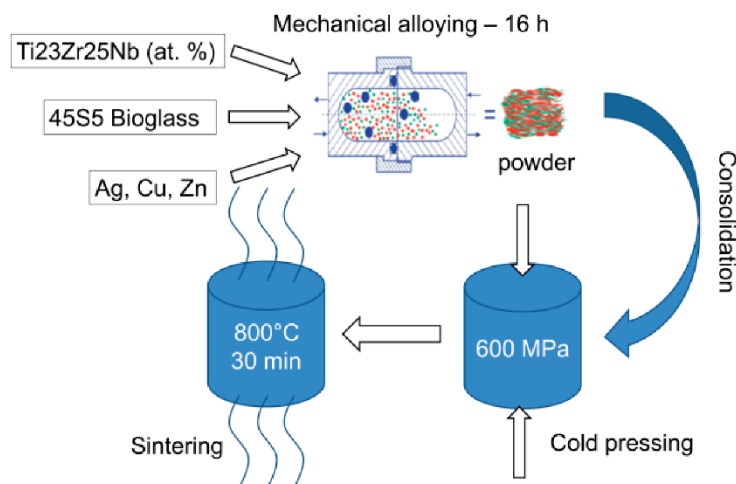
Figure 1. Schematics representation of the mechanism behind the mechanical alloying of biocomposites.

2.2. Materials Characterization

The crystal structure of produced samples in the powder and bulk stage was evaluated with the Panalytical Empyrean XRD equipment with CuKα radiation (Malvern Panalytical B.V., Almelo, The Netherlands). The microstrain and crystallite size of the powders after 16 h of mechanical alloying was calculated with the uniform deformation model (UDM) of the Williamson–Hall analysis method [52]. Rietveld refinement with Maud software was carried out to estimate the phase amount and lattice parameters of the following phases:

-   Ti (α) (ref. code 01-071-4632) hexagonal P63/mmc
-   Ti (β) (ref. code 01-074-7075) cubic Im-3m
-   Ti_2ZrO (ref. code 01-072-1881) hexagonal P6/mmm
-   Nb_5Si_3P (ref. code 00-051-0788) hexagonal P63/mcm

The refinement was done with the use of the Marquardt least-squares algorithm. The following pattering fitting parameters were calculated: R_{wp}—weighted pattern residual indicator; R_{exp}—expected residual indicator; S—the quality of the fit (lower than 2 for all refinements).

The one selected Ti23Zr25Nb-based (at.%) composite with 9 wt.% 45S5 Bioglass content was examined with a scanning electron microscope (SEM, VEGA 5135 Tescan, Brno, Czech Republic) with an energy dispersive spectrometer (EDS, PTG Prison Avalon, Princeton Gamma Tech., Princeton, NY, USA) calibrated by the typical Cu calibration procedure. The goal of the analysis was to obtain the EDS mapping for componental elements of the material: Ti, Zr, Nb, Si, Ca, Na, P, Ag, Cu, Zn. Additionally, the final powders after the mechanical alloying of Ti23Zr25Nb-BG composites were observed with the same instrument at two different magnifications to present both morphology and particle size. The porosities of the samples were calculated from the histograms in GIMP software based on the micrographs of non-etched samples obtained from the optical microscope Olympus GX51 (Olympus, Tokyo, Japan). Calculations included the pores of different sizes, revealed at two different magnifications.

Mechanical properties of the materials were tested with a Vickers microhardness tester Innovatest Nexus (Innovatest, Maastricht, The Netherlands). The measurement parameters were as follows: an applied load of 300 g and loading time of 10 s. Ten hardness measurements were conducted for each sample. Nanoindentation tests for selected samples with different contents of 45S5 Bioglass were also done with Picodentor HM500 (Fischer Technology Inc., Windsor, CT, USA). The measurement was carried out with DIN 50 359/ISO 14577 standard and load parameters: F = 300 mN/20 s, C = 5 s. Based on load-depth curves, the indentation modulus (EIT) was calculated.

A Kruss-DSA25 digital camera and Kruss-Advanced 1.5 software (Krüss, Hamburg, Germany) was used to measure diiodomethane and glycerol contact angles as well as calculate surface free

energies with dispersive (polar) parts for every bulk sample; each sample polished with the Al_2O_3 suspension, flushed with alcohol and dried. The ellipse method was used to fit the drop shape formed with 2 μL of the mentioned fluids. Tests were conducted at ambient conditions (23 °C) and three times for each sample.

Corrware and Corrview software, as well as the Solartron 1285 potentiostat (Solartron Analytical, Farnborough, UK), were used for the potentiodynamic corrosion measurements of all composites polished with 600 grit grinding paper and cleaned with the ethanol inside an ultrasonic bath before each measurement. Open-circuit potential measurement (OCP) was first conducted for 60 min. In the created electrochemical cells, Ringer's solution (NaCl: 9 g/L, KCl: 0.42 g/L, $CaCl_2$: 0.48 g/L, $NaHCO_3$: 0.2 g/L) was the electrolyte and Ag/AgCl was used as the reference electrode. Each material was examined three times with both corrosion potential and current calculated from Tafel curves. The measurement was conducted in the range of −1 V to 2.5 V vs. OCP, and the scan speed was equal to 1 mV/s.

### 2.3. Assessment of Biofilm Formation Inhibition

The strain of *S. mutans* was obtained from the American Type Culture Collection (ATCC 25175). A detailed description of the assessment of biofilm formation inhibition was previously presented [4].

The quantitative dilutions and surface spread method were applied to assess the bacterial adherence, after 4 h and 20 h, respectively, to the experimental biomaterial surfaces. All experiments were repeated three times. Statistical software R version 3.0.1 was applied to determine whether any significant difference existed in bacterial numbers in the antibacterial experiments. Analysis of variance (ANOVA) followed by Tukey's honest significant difference (HSD) test were performed on the bacterial counts. The statistical significance was defined as $p < 0.05$.

3. Results

Figure 2 presents the diffractograms of TiZrNb-based composites powders in the function of milling time. The 3 wt.% content of 45S5 Bioglass led to the longer form of the new Ti (β) phase in comparison to the Ti23Zr25Nb alloy [1]. The Ti (β) phase appeared after 10 h of milling and 16 h of mechanical alloying was needed to produce the single structure Ti (β) powder. For the biocomposites with the 6 and 9 wt.% 45S5 Bioglass content, after 10 h hours of milling peaks from all starting phases Ti (α), Nb/Ti (β), and Zr were still visible. However, in the case of the Ti23Zr25Nb-6BG composite after 16 h of milling, only Ti (β) peaks were visible with trace contents of others. The Ti23Zr25Nb-9BG composite still had a multi-phase structure after 16 h of milling with the presence of other starting phases among Ti (β). Milling between 10 h and 16 h led only to the further fraction of the structure of the powder because of their plastic deformation and hardening caused by the high density of dislocations and the amorphization of the material [53].
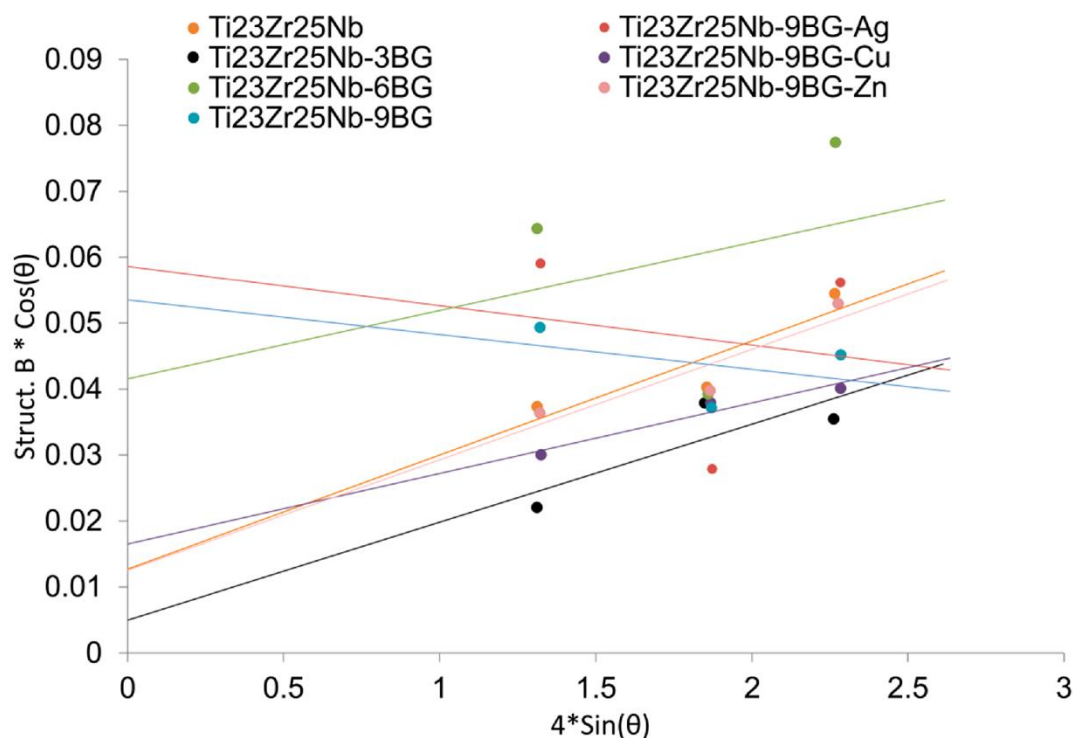
The content of 45S5 Bioglass also decreased the crystallite size of the materials in the as-milled state (Figure 3), which was equal to 2.6 nm for the 9 wt.% 45S5 Bioglass content. Further reduction could also be conducted with the 1 wt.% content of silver and made it equal to 2.4 nm. Both powders of Ti23Zr25Nb-9BG and Ti23Zr25Nb-9BG-Ag only produced samples with negative microstrains which corresponded to the tensile strains. Copper and zinc led to the increase in the crystallite size—8.4 and 11.1 nm, respectively, with positive microstrains corresponding to the compression strains.
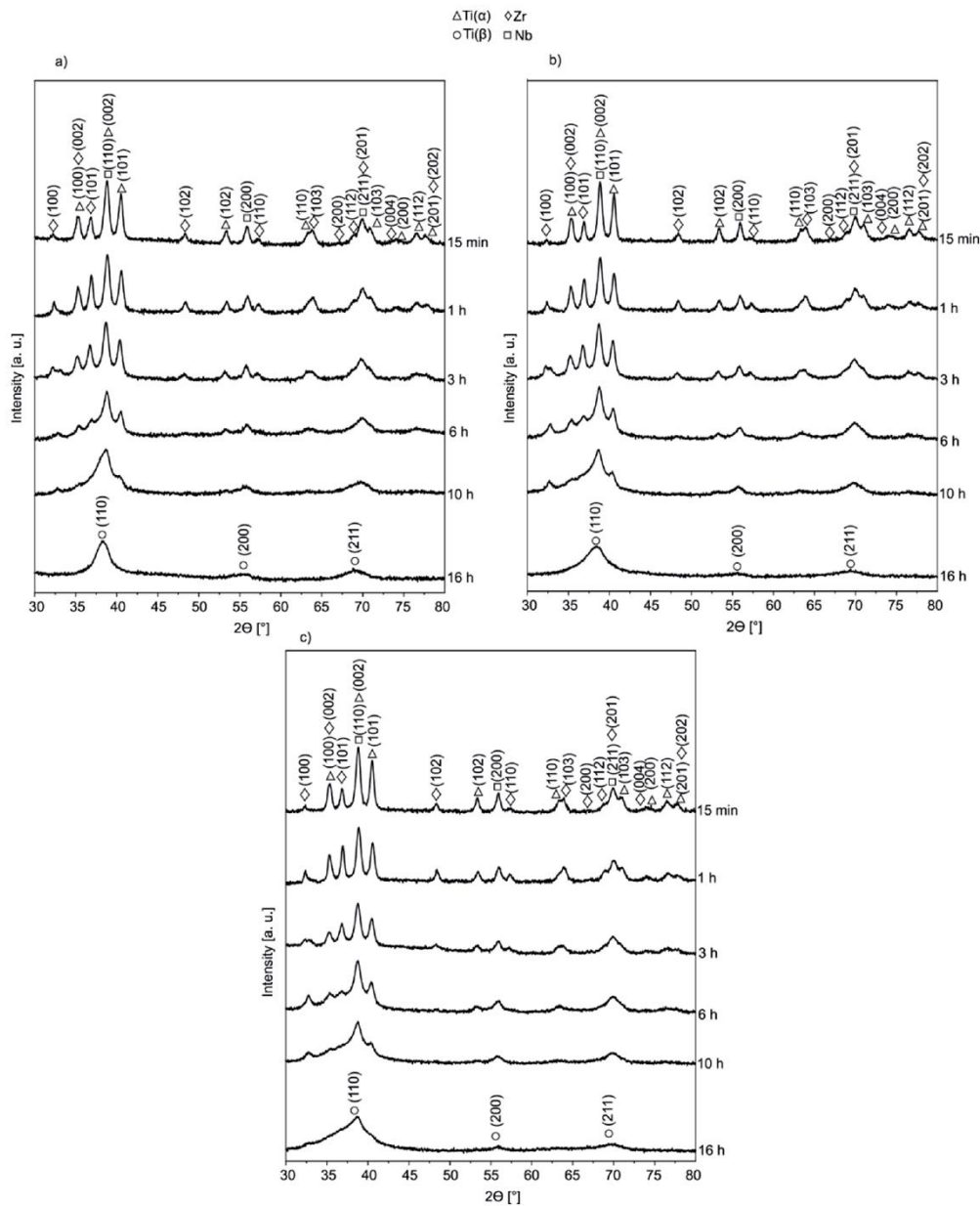
Figure 2. XRD spectra of Ti23Zr25Nb-based composites powders with (**a**) 3 wt.%, (**b**) 6 wt.%, and (**c**) 9 wt.% 45S5 Bioglass content mechanically alloyed over different times.

The micrographs of mechanically alloyed (16 h of MA) powders are presented in Figure 4. The morphology of powders particles of all composites was in an irregular shape within the wide size range in contrast to the non-modified Ti23Zr25Nb alloy [47]. Most of them varied from not strongly agglomerated particles in sizes of less than 10 microns to highly agglomerated particles in sizes of hundreds of microns with the biggest particles in sizes of approximately 500 μm. The variation of the particle size was much higher than in the non-modified alloys [1]. The structure of powder was lamellar, with the ceramic phases on the surface of the particles increasing in volume with the bioglass content.

Figure 3. Linear Williamson–Hall plots with estimated crystallite size (CS) and microstrain (MS) factors based on the XRD spectra of Ti23Zr25Nb-based composites powders after 16 h of mechanical alloying in contrast to the mechanically alloyed Ti23Zr25Nb alloy for 10 h.

The cold compaction and sintering of composites did not allow the formation of the single-phase Ti (β) structure (Figures 5 and 6). The amount of Ti (β) decreased to 65.02% in the Ti23Zr25Nb-based composite with the 9 wt.% 45S5 Bioglass content. The addition of Cu and Zn led to its further reduction below 60 wt.% (Table 2). However, despite not having the single-phase Ti (β) structure, Ti (β) was still the dominant phase in all the produced materials. The other phases appearing in materials were Ti (α), Ti_2ZrO, and Nb_5Si_3P. The Ti23Zr25Nb-based composite with the 3 wt.% content of 45S5 Bioglass was still the material with the highest amount of the Ti (β) phase which was above 95%.
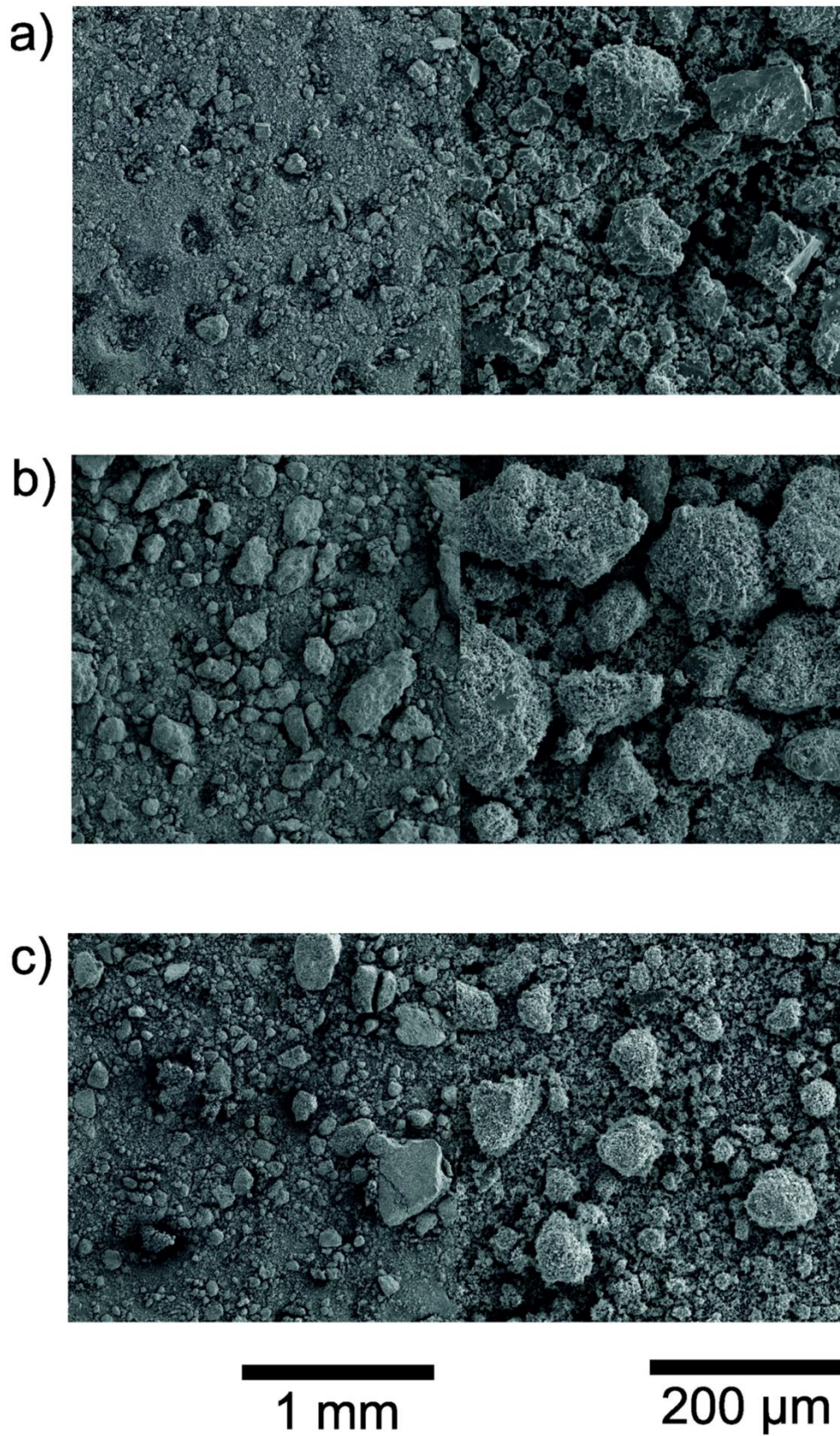
Figure 4. SEM microphotographs of Ti23Zr25Nb-based composites powder agglomerates with the (**a**) 3 wt.%, (**b**) 6 wt.%, and (**c**) 9 wt.% 45S5 Bioglass content mechanically alloyed for 16 h.
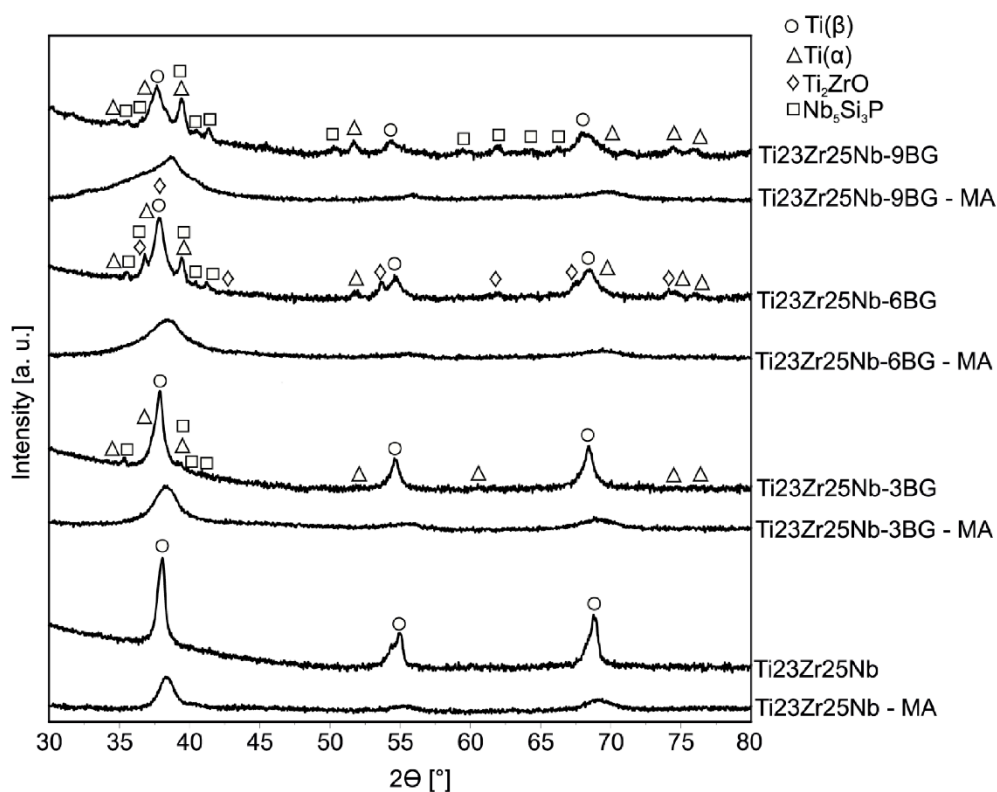
Figure 5. XRD spectra of Ti23Zr25Nb-based composites with the 3, 6, and 9 wt.% 45S5 Bioglass content sintered at 800 °C for 0.5 h in an argon atmosphere in contrast with the mechanically alloyed powders milled for 16 h and the Ti23Zr25Nb alloy sintered with the same parameters and mechanically alloyed for 10 h.
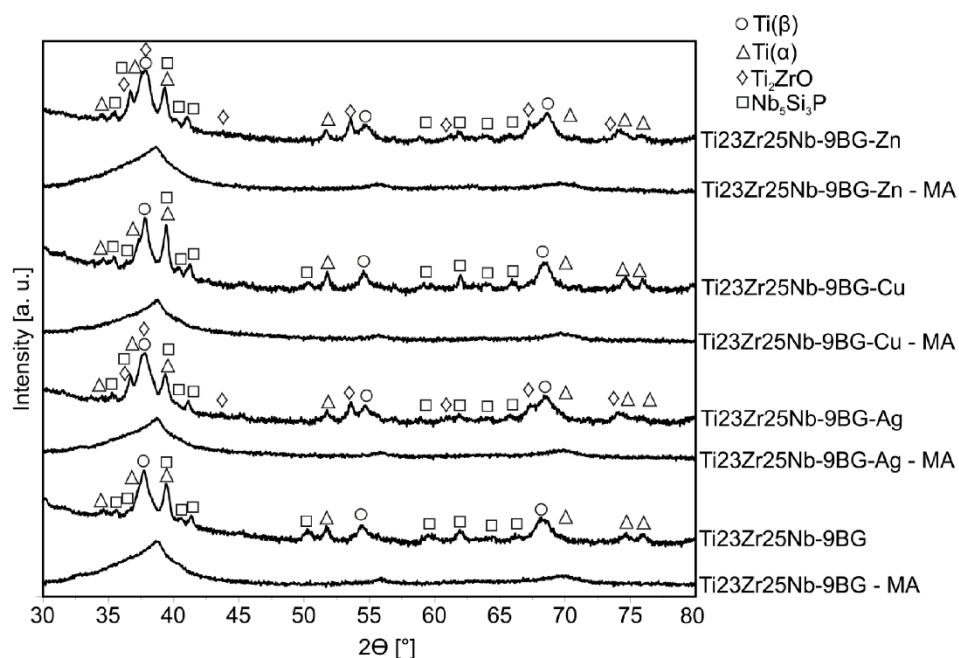
Figure 6. XRD spectra of Ti23Zr25Nb-based composites with the 9 wt.% 45S5 Bioglass and 1 wt.% Ag, Cu, Zn content sintered at 800 °C for 0.5 h in an argon atmosphere in contrast with mechanically alloyed powders for milled for 16 h and the based Ti23Zr25Nb-9BG composite sintered with the same parameters and mechanically alloyed for 16 h.

Table 2. Crystallographic data analysis of bulk Ti23Zr25Nb-based composites with the 3, 6, 9 wt.% 45S5 Bioglass and 1 wt.%. Ag, Cu, Zn content in contrast to the Ti23Zr25Nb alloy.

Sample	Tiα				Tiβ			Ti$_2$ZrO				Nb$_5$Si$_3$P				Rwp [%]	Rexp [%]	S
	a [Å]	c [Å]	V [Å3]	PA [%]	a [Å]	V [Å3]	PA [%]	a [Å]	c [Å]	V [Å3]	PA [%]	a [Å]	c [Å]	V [Å3]	PA [%]			
Ti23Zr25Nb	-	-	-	-	3.3524 (2)	37.68 (1)	100	-	-	-	-	-	-	-	-	6.28	3.65	1.72
Ti23Zr25Nb 3BG	2.9987 (35)	4.8192 (136)	37.53 (20)	2.08	3.3602 (2)	37.94 (1)	96.38	-	-	-	-	7.7633 (145)	5.3173 (135)	277.53 (1.74)	1.54	4.65	3.4	1.37
Ti23Zr25Nb 6BG	2.9967 (9)	4.7992 (35)	37.32 (5)	9.83	3.3577 (2)	37.86 (1)	75.63	4.7683 (11)	3.0281 (7)	59.62 (4)	10.47	7.7296 (34)	5.3123 (27)	274.87 (38)	4.07	3.83	3.22	1.19
Ti23Zr25Nb 9BG	3.0003 (6)	4.8085 (21)	37.49 (3)	28.13	3.3720 (4)	38.34 (2)	65.02	-	-	-	-	7.7132 (25)	5.2967 (20)	272.9 (28)	6.86	4.52	3.44	1.31
Ti23Zr25Nb 9BG-Ag	3.0011 (8)	4.7970 (32)	37.42 (5)	15.3	3.3579 (4)	37.86 (2)	65.98	4.7858 (10)	3.0329 (8)	60.16 (4)	13.73	7.7575 (29)	5.3213 (22)	277.33 (32)	4.99	3.97	3.1	1.28
Ti23Zr25Nb 9BG-Cu	2.9946 (4)	4.8229 (12)	37.46 (2)	31.89	3.3629 (3)	38.03 (1)	59.1	-	-	-	-	7.7398 (27)	5.3117 (21)	275.57 (30)	9.00	5.02	3.38	1.49
Ti23Zr25Nb 9BG-Zn	3.0033 (5)	4.8188 (21)	37.64 (3)	17.13	3.3557 (3)	37.79 (1)	54.68	4.7897 (7)	3.0301 (6)	60.20 (3)	19.47	7.7671 (24)	5.3331 (18)	278.63 (26)	8.73	3.64	2.96	1.23

EDS mapping confirms the homogenous distribution of all componential elements of the composites on the micro-scale (Figure 7). There were no inhomogeneities in the bulk materials which could have appeared during the consolidation of mechanically alloyed powders. Moreover, maps in Figure 8 presents the distribution of all antibacterial activities (Ag, Cu, and Zn) in the biocomposite matrix.
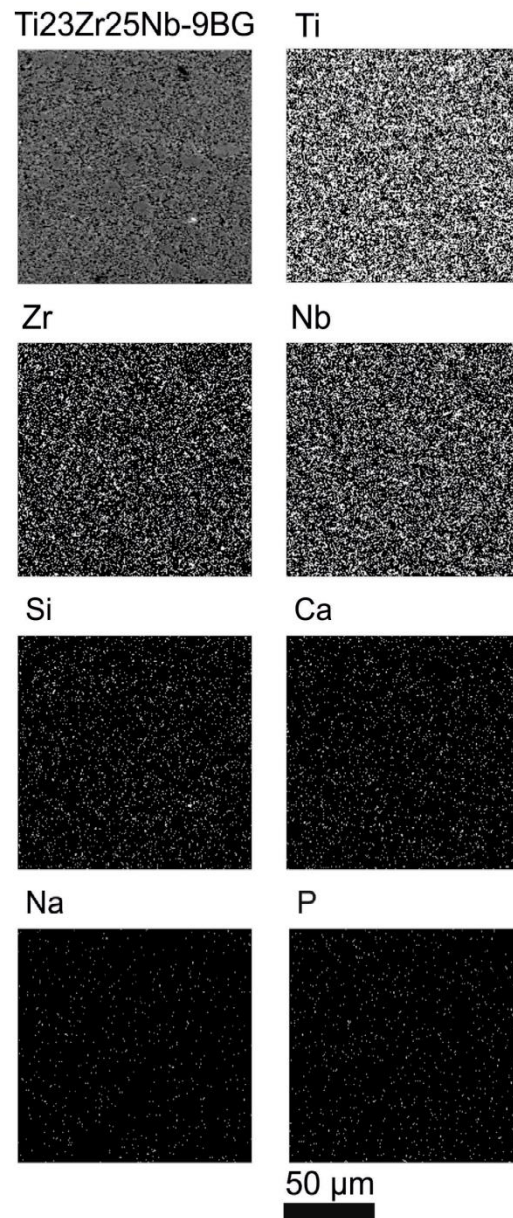
Figure 7. Energy-Dispersive Spectroscopy (EDS) maps of Ti, Nb, Zr, Si, Ca, Na in the Ti23Zr25Nb-based composite with the 9 wt.% 45S5 Bioglass content and within the area of the scan micrograph.
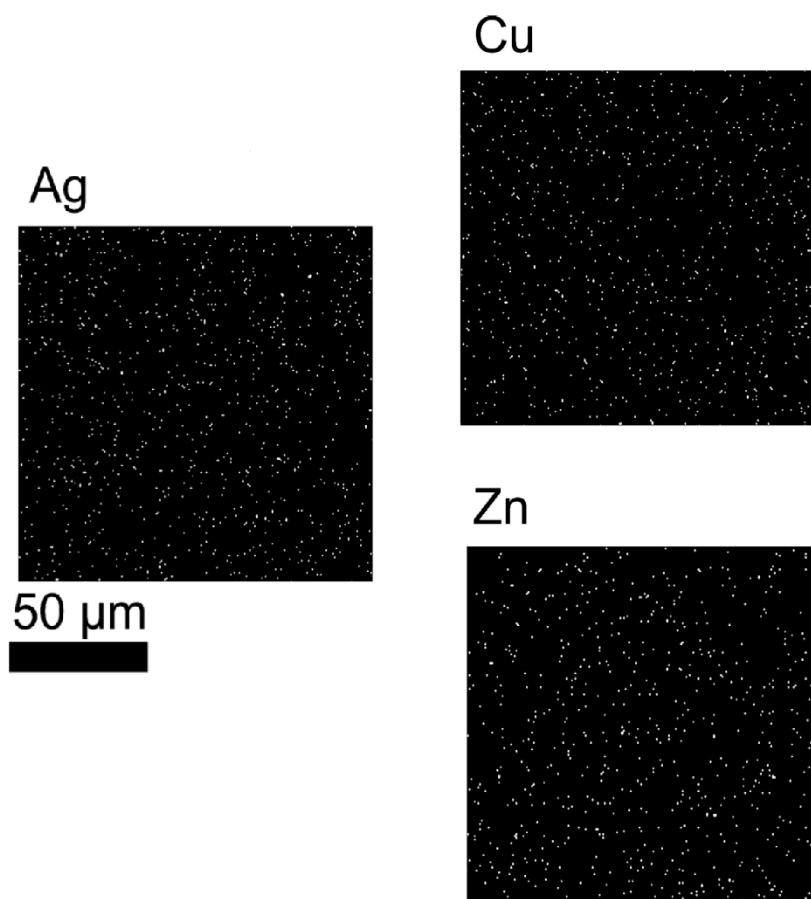
Figure 8. Energy-Dispersive Spectroscopy (EDS) maps of Ag, Cu and Zn in the bulk Ti23Zr25Nb-based composite with the 9 wt.% 45S5 Bioglass and 1 wt.% Ag, Cu, Zn.

The porosities of the biocomposites were calculated and are presented in Table 3 and differ between 13.7% (Ti23Zr25Nb-9BG-Zn) and 22.8% (Ti23Zr25Nb-9BG). The morphology of the pores is additionally presented in the micrographs in Figure 9. Porosities were homogeneously distributed on the microscale. Additionally, in Ti23Zr25Nb-6BG and slightly in Ti23Zr25Nb-9BG, a large number of porosities in the size of 10–100 μm were additionally visible with the lower magnifications.

Table 3. Porosities calculated with the use of optical micrographs and histograms in GIMP software.

Material	Porosity [%]
Ti23Zr25Nb-3BG	15.4 ± 3.6
Ti23Zr25Nb-6BG	22.1 ± 8.9
Ti23Zr25Nb-9BG	22.8 ± 6.5
Ti23Zr25Nb-9BG-Ag	14.0 ± 4.1
Ti23Zr25Nb-9BG-Cu	18.3 ± 7.8
Ti23Zr25Nb-9BG-Zn	13.7 ± 4.6

The mechanical properties of produced composites were superior to commercially pure titanium in terms of their biomedical application. The Young modulus was significantly lower and was lowest for the Ti23Zr25Nb-based composite with the 9 wt.% 45S5 Bioglass content in comparison to the 140.9 ± 2.0 GPa of titanium [1]. The Young modulus of this composite was in conjunction with the high porosity (around 20%) and the lowest hardness (218 HV0.3) (Figure 10 and Table 4). Despite the hardness similar to titanium, the drastic reduction of the Young modulus made it close to the modulus of human bone. Contact angles of all the materials were lower than 90 for both diiodomethane and

glycerol. It confirmed the good wettability of the produced composites. Surface free energies (SFEs) were similar and differed from 34.6 mN/m (Ti23Zr25Nb-6BG) to 42.3 mN/m (Ti23Zr25Nb-9BG-Ag).
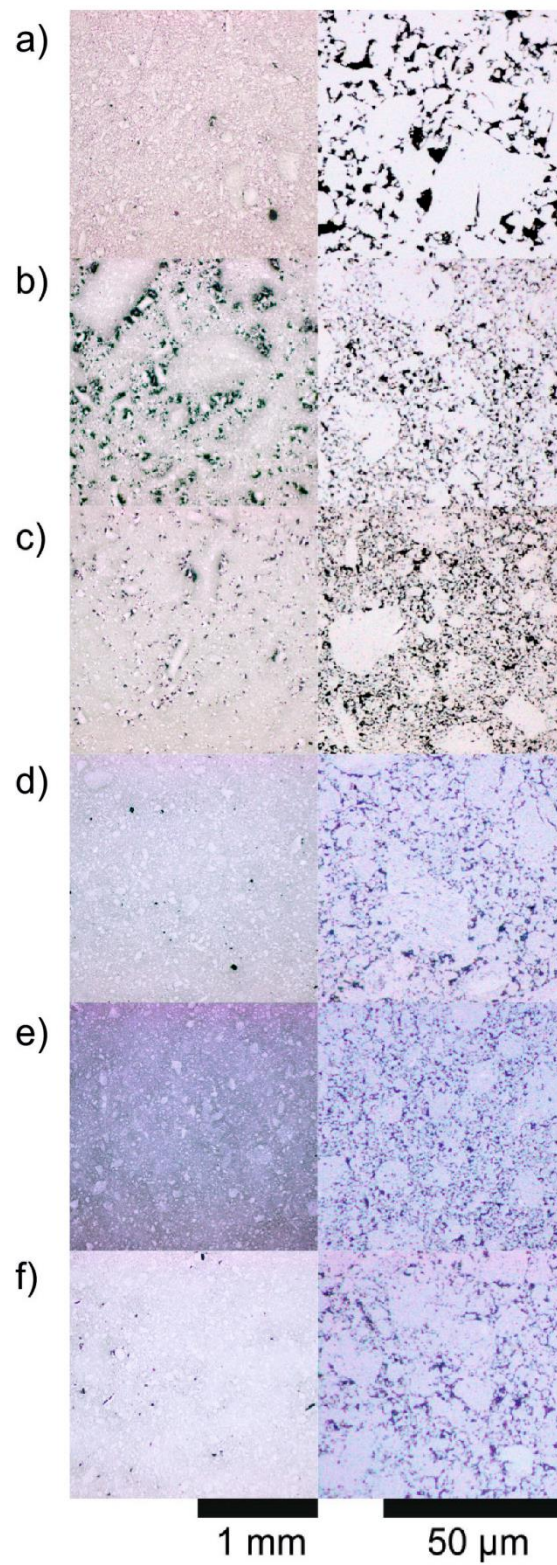
Figure 9. Micrographs of non-etched biocomposites revealing porosities (black in the graph) at 2 different magnifications: Ti23Zr25 (at.%) with (**a**) 3 wt.%, (**b**) 6 wt.% and (**c**) 9 wt.% of 45S5 Bioglass content and Ti23Zr25Nb-9BG doped with (**d**) Ag, (**e**) Cu and (**f**) Zn.
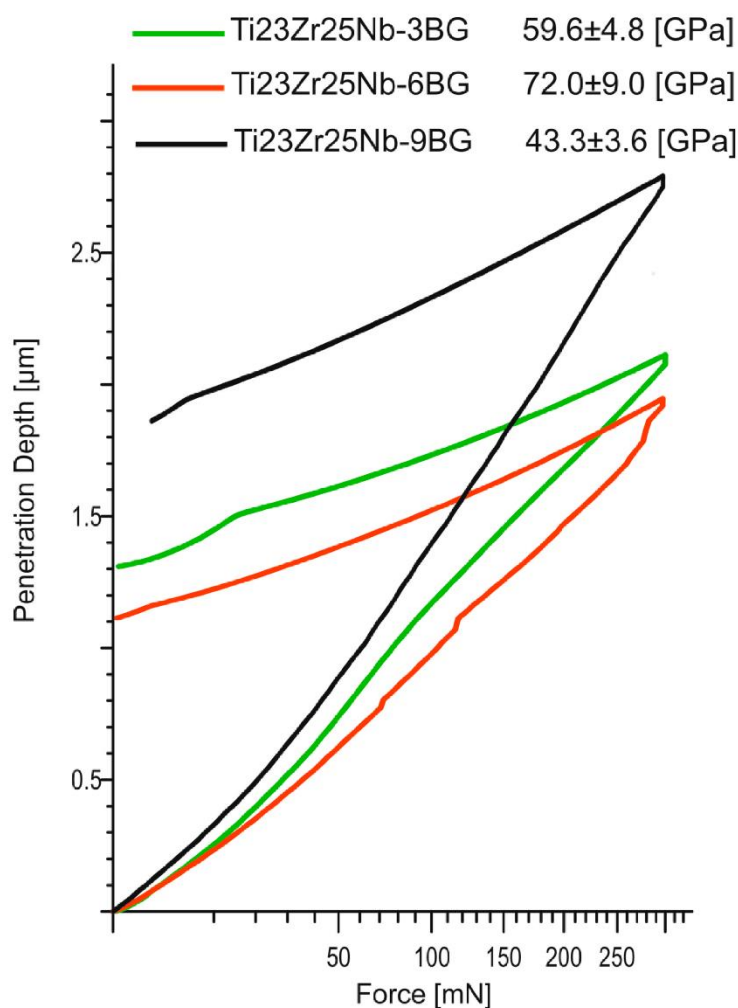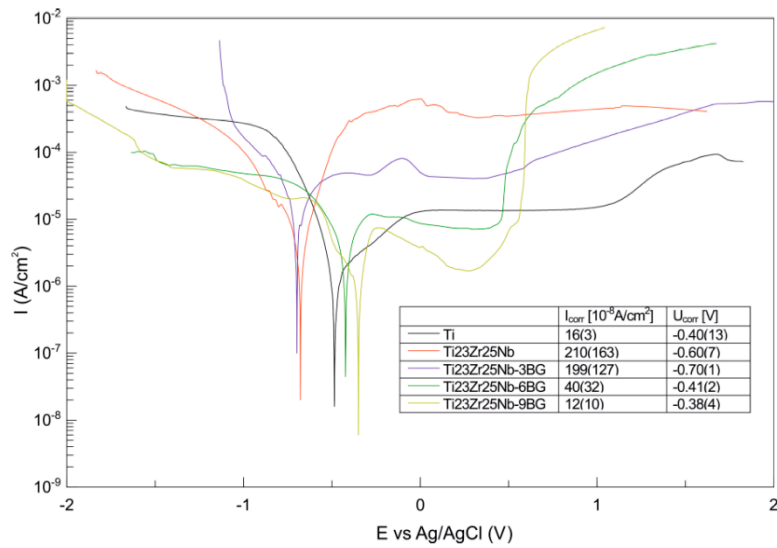
Figure 10. Load-depth curves of bulk Ti23Zr25Nb-based composites with the 3, 6, and 9 wt.% 45S5 Bioglass content.

Table 4. Vickers hardness (HV0.3), surface free energy (SFE), dispersive and polar parts of SFE, diiodomethane, and glycerol contact angles for Ti23Zr25Nb-based composites with the 3, 6, 9 wt.% 45S5 Bioglass and 1 wt.% Ag, Cu, Zn content in contrast to the Ti23Zr25Nb alloy.

Sample	HV0.3	CA [M] Diiodomethane [°]	CA [M] Glycerol [°]	SFE [mN/m]	Disperse [mN/m]	Polar [mN/m]
Ti23Zr25Nb	375 ± 33	62.2 ± 9.0	64.6 ± 4.9	35.1 ± 10.0	27.4 ± 5.6	7.7 ± 4.4
Ti23Zr25Nb-3BG	315 ± 36	50.8 ± 7.4	70.2 ± 4.5	36.1 ± 6.5	33.8 ± 4.4	2.3 ± 2.1
Ti23Zr25Nb-6BG	321 ± 22	56.0 ± 6.2	68.1 ± 7.4	34.6 ± 5.7	30.9 ± 3.7	3.7 ± 2.0
Ti23Zr25Nb-9BG	218 ± 23	57.7 ± 4.4	61.5 ± 4.2	36.9 ± 3.3	29.9 ± 2.5	7.0 ± 0.8
Ti23Zr25Nb-9BG-Ag	322 ± 24	44.9 ± 3.8	57.5 ± 2.4	42.3 ± 4.2	37.0 ± 2.2	5.3 ± 2.0
Ti23Zr25Nb-9BG-Cu	329 ± 49	49.3 ± 2.4	66.7 ± 4.7	37.5 ± 2.5	34.7 ± 1.3	2.8 ± 1.2
Ti23Zr25Nb-9BG-Zn	387 ± 49	50.5 ± 6.6	77.8 ± 3.1	34.6 ± 4.4	33.9 ± 3.9	0.7 ± 0.5

The corrosion resistance of Ti23Zr25Nb-9BG is also similar to that of titanium and significantly better than that of the Ti23Zr25Nb alloy sintered at the same temperature—800 °C (Figure 11) which was based on the lower corrosion current and higher corrosion potential results. The corrosion current can be further limited by doping this material with silver. However, the corrosion potential of the Ti23Zr25Nb-9BG-Ag composite was higher and there was no clear and visible passivation as in the Ti23Zr25Nb-9BG composite. There was no passivation also in the Ti23Zr25Nb-9BG-Cu alloy (Figure 12).

Figure 11. Potentiodynamic curves of bulk Ti23Zr25Nb-based composites with the 3, 6, and 9 wt.% 45S5 Bioglass content in contrast to cp-Ti and the Ti23Zr25Nb alloy.
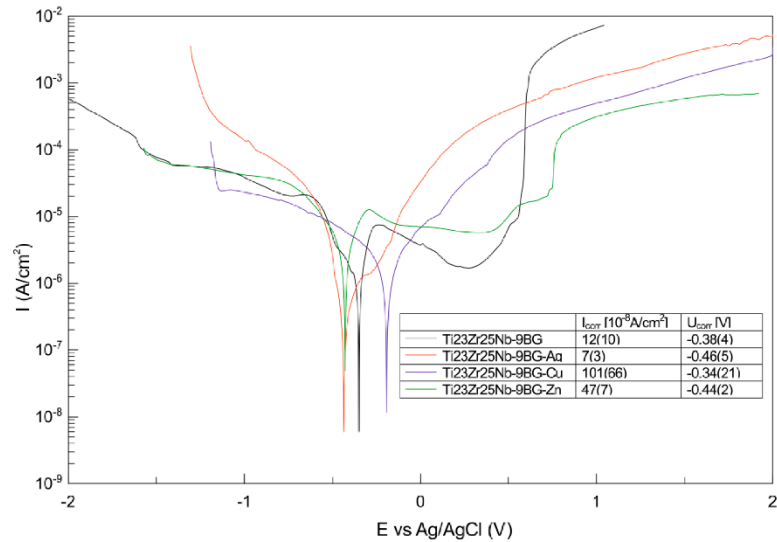
Figure 12. Potentiodynamic curves of bulk Ti23Zr25Nb-based composites with the 9 wt.% 45S5 Bioglass and 1 wt.% Ag, Cu, Zn content in contrast with the Ti23Zr25Nb-9BG composite.

Figure 13 shows the results of viable bacteria adhered to the different experimental material surfaces when exposed to *S. mutans* ATCC 25175. The bacterial adhesion was significantly reduced on the surface of Ti23Zr25Nb-9BG-Ag, Ti23Zr25Nb-9BG-Cu, and Ti23Zr25Nb-9BG-Zn composites compared to microcrystalline titanium. These biomaterials were observed to have significantly lower adhesion levels ($p < 0.05$) of *S. mutans* ATCC 25175, suggesting that these composites have inhibited biofilm formation. On the other hand, many bacteria were found on the Ti23Zr25Nb, Ti23Zr25Nb-9BG composites, as shown in Figure 13, displaying that these composites have low antibacterial activity against the reference strain of *S. mutans* (Table 5).
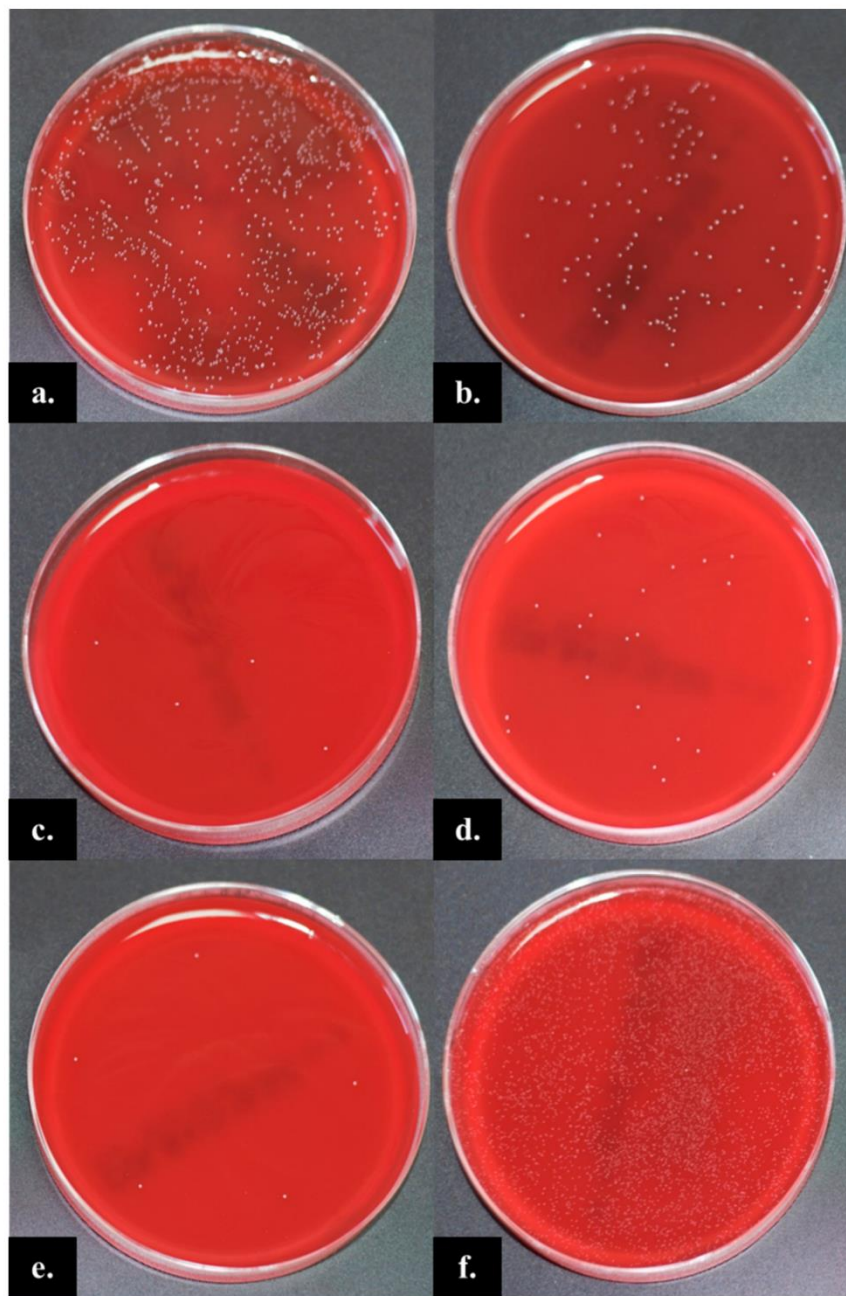
Figure 13. Antibacterial activity against *S. mutans* ATCC 25175 growth on agar plates from the same dilution after 24 h incubation on different composites: (**a**) Ti23Zr25Nb, (**b**) Ti23Zr25Nb-9BG, (**c**) Ti23Zr25Nb-9BG-Ag, (**d**) Ti23Zr25Nb-9BG-Cu, (**e**) Ti23Zr25Nb-9BG-Zn, (**f**) control (Ti).

Table 5. Antibacterial activity of composites against *S. mutans* ATCC 25175.

Sample	CFU/mL After 4 h of Incubation	CFU/mL After 20 h of Incubation	RF %
Ti23Zr25Nb	$<1.0 \times 10^3$	3.2×10^4	78.67
Ti23Zr25Nb-9BG	$<1.0 \times 10^3$	2.4×10^4	84
Ti23Zr25Nb-9BG-Ag	$<1.0 \times 10^3$	3.1×10^3	97.93
Ti23Zr25Nb-9BG-Cu	$<1.0 \times 10^3$	8.5×10^3	94.33
Ti23Zr25Nb-9BG-Zn	$<1.0 \times 10^3$	3.5×10^3	97.67
microcrystalline Ti (control)	$<1.0 \times 10^3$	2.0×10^5	-

CFU—colony-forming unit; RF—reduction factor.

4. Discussion

The crystal structure evaluation of the obtained materials clearly shows that the addition of 45S5 Bioglass limits the β stabilizing effect of niobium and zirconium. In its lower concentrations, only α and β phases peaks were visible. However, with higher concentrations of 45S5 Bioglass and elements such as silicon, calcium, sodium, and phosphorous, completely different phases than thos evident titanium-based solutions were present (Figure 2). It means that mechanical alloying leads to the homogenous distribution of 45S5 Bioglass components in the titanium matrix (Figure 7) but also destabilizes it during both milling and sintering. It could have been changed with the short milling of the proposed 45S5 Bioglass powders with the pre-milled Ti23Zr25Nb powders. This type of composite producing technique should lead to the mainly homogenous distribution of the amorphous 45S5 Bioglass phase in the beta-phase Ti23Zr25Nb alloy matrix. The main disadvantage of this method would be an aggregation of the 45S5 Bioglass and limitation of the fine-grained structure biocomposite formation. The proposed method of producing TiNbZr-based composites destabilized 45S5 Bioglass during the process but gave interesting mechanical, corrosion, and antibacterial results in terms of their biomedical applications.

With the higher content of 45S5 Bioglass, a significant reduction in the crystallite size could be observed. It was because of the limitation of the cold welding effect during milling and the intensification of plastic deformation and structure fracturing of the powders. It was visible both with much broader Ti (β) XRD peaks (Figure 5) and based on the Williamson–Hall linear plots. The size of the crystallite size can be limited even below 4 nm for Ti23Zr25Nb-6BG, Ti23Zr25Nb-9BG, Ti23Zr25Nb-9BG-Ag (Figure 3).

The limitation of Ti (β) with 45S5 Bioglass content was caused by its α-stabilizing effect, which was mainly caused by the major oxygen presence in its composition. This type of effect has also been observed in other β-type alloys as Ti-Mo alloys [54]. An increase in the Ti (β) lattice constant was observed in the Ti23Zr25Nb-3BG composite (Rietveld refinement results—Table 2). This content of 45S5 Bioglass did not allow the formation of phases other than titanium solutions: Ti (α) and Ti (β). That means that all of the 45S5 Bioglass elements were dissolved in the titanium solutions and mainly in the major Ti (β) phase leading to its extension.

Significant changes can be observed in the behavior of the alloy with the 6 wt.% content of 45S5 Bioglass. The precipitation of interstitial phases of Ti_2ZrO and Nb_5Si_3P were present because introduced elements could not be dissolved in the titanium solutions. Furthermore, the limitation of Zr content in the cubic Ti (β) phase led to the drastic decrease in its amount and contraction of its lattice constants (in contrast to the 3 wt.% content of 45S5 Bioglass).

The further increase in the 45S5 Bioglass content to 9 wt.% led to the progressing precipitation of the Nb_5Si_3P and finally to a 65% content of Ti (β) in the produced composites. Furthermore, because of no Ti_2ZrO participation, the Ti (β) lattice constant extended to the highest values of all the produced materials—3.3720 Å.

The addition of silver was proven to have some beta-stabilizing effect on the Ti23Zr25Nb-9BG composite. Despite the Zr limitation in the titanium solution because of the Ti_2ZrO phase formation, the addition of Ag increased the amount of the Ti (β) phase. The drastic contraction of a unit cell and a decrease in the lattice constant to 3.3579 Å was also observed.

In the case of alloys with other antibacterial additives, a reduction in the Ti (β) phase content was visible despite the beta-stabilizing effect of Cu and Zn. The loss of niobium in Nb_5Si_3P precipitates was too high and could not be replaced with both these elements, which tend to create eutectoid phase diagrams with titanium [55,56] and not isomorphous ones as does niobium [57].

In Ti23Zr25Nb-9BG-Ag and Ti23Zr25Nb-9BG-Zn, similar phenomenon as to those observed in Ti23Zr25Nb-6BG can be observed. The formation of Ti_2ZrO limited the Zr soluted in the Ti (β) phase, which led to its contraction in contrast to Ti23Zr25Nb-9BG and Ti23Zr25Nb-9BG-Cu composites.

Ti_2ZrO presence in the selected materials: Ti23Zr25Nb-6BG, Ti23Zr25Nb-9BG-Ag, and Ti23Zr25Nb-9BG-Zn might have been caused by the interfacial reaction between titanium and

zirconia formed from the oxygen being in the 45S5 Bioglass content during sintering. This type of reaction could lead to the formation of a hexagonal and oxygen-deficient Ti_2ZrO phase [58].

The distribution of all elements in the titanium matrix was homogenous, which also corresponded to the homogenous distribution of all precipitates (Figure 7). The same type of distribution can also be observed in materials with the addition of Ag, Cu, and Zn (Figure 8) with none of this element being aggregated in produced composites but regularly dispersed in its volume and materials matrix. This type of composite is possible and easy to produce with mechanical alloying, which is absolutely the novel approach.

The Young modulus of all composites makes them suitable for biomedical applications. The most interesting could be the modulus of Ti23Zr25Nb-9BG, which is equal to 43.3 GPa and significantly lower than that of other β-type titanium alloys produced by members of our group [1–3]. However, there are still porous structures with significantly lower Young modulus' than those or Ti-based materials produced with the gel casting techniques, which could be one of the methods of reducing the modulus' of this type of material further [59]. The elastic modulus of the human bone can be measured as a wide range of values (from 4 to 30 GPa), depending on the testing parameters such as measuring direction and the exact type of the examined bone tissue [60,61]. With the nanoindentation using the Berkovich tip and the Oliver–Pharr indentation method, the Young modulus of bone was estimated as equal to 20 GPa and 10 GPa for dry and wet bone, respectively [62]. That means that the Ti23Zr25Nb-9BG Young modulus is still far from the modulus of bone but much closer than most titanium-based alloys. This composite allows us to limit the stress-shielding effect caused by the high elastic modulus of the implant and all the harmful effects of that phenomenon such as bone resorption, implant loosening, and implant failure [61,63]. The lower modulus of this composite could also be caused by its high porosity (around 20%), which should also lead to intensified osseointegration [64]. This limitation of the Young modulus goes in tandem with a decrease in the hardness of this composite. However, it is still beneficial in contrast to commercially pure titanium [1]. The mechanical properties of this composite are also coincidentally similar to the lattice constant of the T (β) phase, which is significantly the highest of all the tested materials (3.3720 Å). It might prove that in the Ti (β) phase, most bioglass components such as phosphorous and calcium, along with zirconium, which was proven in our previous research to have a high impact on the lattice constant, have dissolved. In contrast, for the hardest Ti23Zr25Nb-9BG-Zn, the hardness and lattice constant were equal to 387 HV0.3 and 3.3557 Å, respectively.

The surface free energy of all alloys was in the range of about 30–40 mN/m, contact angles were in the range of about 45–60° for diiodomethane, and about 60–80° for glycerol. That means that the wettability of all the composites was high, and all of them can be named as hydrophilic, with no significant differences between all of them (Table 4). Formation of the hydrophilic surface should not inhibit bone tissue growth on the produced materials, which could happen with the hydrophobic surface due to the high affinity to the broad types of proteins of this type of surface [65].

The corrosion current decreased, and the corrosion potential increased with the 45S5 Bioglass content (Figure 11). However, Ti23Zr25Nb-6BG and Ti23Zr25Nb-9BG alloys showed a drastic increase in the corrosion current around +0.5 V potential, which corresponds to the changes in the passive film. Both these composites should not be used in these ranges. Above +1 V there was once again the constant corrosion current and the composites should not corrode, being in the range of anodic protection. The Ti23Zr25Nb-3BG composite potentiodynamic curve was similar to that of Ti23Zr25Nb and pure titanium despite the higher corrosion current and the lower corrosion potential. The increase in the corrosion resistance of alloys containing 45S5 Bioglass could be caused by the significant changes in its passive film composition. This was observed by other researches on other types of alloys as magnesium alloys. The surface of the composite might be enriched with calcium and phosphate, leading to the formation of chemical compounds containing both of these elements [66,67].

The Ti23Zr25Nb-9BG-Ag composite had the lowest corrosion current of all the composites (Figure 12). It is well known and researched that the addition of a noble metal such as silver to the alloy

can lead to that because of the increase in the passive film stability and the easiness of passivation [68]. The addition of copper tends to increase the corrosion current to the highest corrosion current among all the composites. It could be caused by the copper enrichment of the passive film and its impoverishment with the other alloy components such as Ti, Zr, Nb, Ca, and P. Other research groups previously observed this type of change in the passivation behavior of titanium-based alloys [69]. The same type of mechanism may provide the increase in corrosion current of the Ti23Zr25Nb-9BG-Cu composite in contrast to the Ti23Zr25Nb-9BG composite. The curve of Ti23Zr25Nb-9BG-Zn looks most familiar to Ti23Zr25Nb-9BG, with the same type of passivation observed in its anodic part. Furthermore, Ti23ZrNb-9BG-Zn and Ti23Zr25Nb-9BG corrosion currents and potentials were in the same order of magnitude.

In the present research, the ability of *S. mutans* ATCC 25175 to form biofilm on the ultrafine-grained Ti23Zr25Nb alloy and subjected to the different types of chemical modifications, including 45S5 Bioglass, Ag, Cu or Zn was evaluated. *S. mutans* is a Gram-positive bacteria commonly found in the human oral cavity and is the main contributor to tooth decay. The microbe was first described by J. Kilian Clarke in 1924 [70].

The obtained results indicate that the tested *S. mutans* reference strain can adhere to the Ti23Zr25Nb-9BG composites produced by the powder metallurgical method. Additionally, the type of chemical modification (Ag, Cu, Zn) influences the ability of *S. mutans* to form biofilm on the tested biomaterial.

According to published research, when a Ti23Zr25Nb-9BG-Ag composite stays immersed in body fluid, silver could react with the environment and release ionized Ag into the surrounding area [71]. A release of the silver biocide at a concentration level (0.1 ppb) is capable of rendering the antibacterial efficacy [71,72].

The mechanism for bacterial toxicity of the tested Ti23Zr25Nb-9BG-Ag alloy may include the free metal ion toxicity arising from the dissolution of metals from the surface of the silver particles (e.g., Ag+ from Ag) [72,73] or the oxidative stress via the generation of reactive oxygen species (ROS) on crystal surfaces of some nanoparticles [74].

Copper and copper alloys were able to decrease the counts of bacteria, including pathogens such as methicillin-resistant *Staphylococcus aureus* (MRSA), by seven to eight logs within hours [75]. The mechanism for bacterial toxicity of the tested Ti23Zr25Nb-9BG-Cu alloy was the same as in the case of Ag containing biomaterials.

Zinc is an environmentally friendly material and has little toxicity [76]. It is naturally present in dental plaque and saliva. At higher concentrations Zinc is toxic. For many years, Zn was incorporated into many dental materials due to the ability of zinc ions to inhibit the growth of cariogenic bacteria. Recently, it has been shown that zinc oxide nanoparticles (ZnO-NPs) have an antibacterial property [77]. Our findings allowed us to assess the effectiveness of zinc against *S. mutans*.

Titanium remains mostly neutral and is certainly not poisonous for the human body environment, which can tolerate this metal in large doses. Therefore, the composites based on the Ti containing 45S5 Bioglass and Ag (or Cu, Zn) additions have the potential to be used in dentistry with infection control. Generally, the Ti-base alloy containing niobium, zirconium (TiZrNb) is beneficial in dental and other medical device applications. Even though zirconium and other elements in Ti-based alloys for dental and medical uses are nontoxic, there are still ongoing studies to ensure that the materials themselves don't have adverse side effects over the long term [78]. Cossellu et al. found that there might be a link between zirconium implants and some health problems, such as inflammation and skeletal and connective tissue disorders [78]. Ultrafine-grained Ti23Zr25Nb-9BG-based composites possess unique mechanical properties and are thus considered to represent the next generation of biomaterials. Additionally, the addition of the Ag, Cu or Zn to Ti23Zr25Nb-9BG composites significantly lowered the adhesion of *S. mutans*, suggesting that these composites had antibacterial activity.

107

5. Conclusions

The main goal of these studies was to produce biocomposites based on the Ti23Zr25Nb alloy previously tested by our group [1]. The composites were formed by the addition of 45S5 Bioglass and three different antibacterial additives: silver, copper, and zinc. All experiments conducted on these novel materials allow us to withdraw some conclusions:

–   the content of Ti (β) increases with milling time and 45S5 Bioglass decreases it,
–   Ti23Zr25Nb-3BG and Ti23Zr25Nb-6BG need longer milling time (16 h) than Ti23Zr25Nb (10 h) to produce fully single-phase β-type powders,
–   45S5 Bioglass limits the content of Ti (β) as a beta non-stabilizer in the bulk samples,
–   Cu and Zn decrease the content of Ti (β) despite their β–stabilizing properties in the bulk samples,
–   the corrosion, mechanical properties, and wettability of the produced materials are beneficial in contrast to the Ti23Zr25Nb alloy,
–   Ti23Zr25Nb-9BG-Ag, Ti23Zr25Nb-9BG-Cu, Ti23Zr25Nb-9BG-Zn are proved to have high antibacterial activity against *S. mutans* being present in the human oral cavity,
–   produced materials based on the performed experiments are highly recommended for biomedical use (especially as dental implants) because of their high corrosion resistance, low Young modulus, and good antibacterial activity.

Author Contributions: Conceptualization, M.M., M.J.; Formal analysis, M.M.; Funding acquisition, M.J.; Investigation, M.M., P.P., M.R., M.G. and M.U.J.; Supervision, M.J.; Writing—original draft, M.M.; Writing—review and editing, M.M., M.J., P.P., M.R., M.G. and M.U.J. All authors have read and agreed to the published version of the manuscript.

Conflicts of Interest: The authors declare no conflict of interest.

References

1.   Marczewski, M.; Miklaszewski, A.; Jurczyk, M. Structure evolution analysis in ultrafine-grained Zr and Nb-based beta titanium alloys. *J. Alloy. Compd.* **2018**, *765*, 459–469. [CrossRef]
2.   Sochacka, P.; Miklaszewski, A.; Jurczyk, M. Development of β-type Ti-x at. % Mo alloys by mechanical alloying and powder metallurgy: Phase evolution and mechanical properties (10 ≤ x ≤ 35). *J. Alloy. Compd.* **2019**, *776*, 370–378. [CrossRef]
3.   Sochacka, P.; Miklaszewski, A.; Kowalski, K.; Jurczyk, M. Influence of the processing method on the properties of Ti-23 at.% mo alloy. *Metals* **2019**, *9*, 931. [CrossRef]
4.   Jurczyk, K.; Kubicka, M.M.; Ratajczak, M.; Jurczyk, M.U.; Niespodziana, K.; Nowak, D.M.; Gajecka, M.; Jurczyk, M. Antibacterial activity of nanostructured Ti-45S5 bioglass-Ag composite against Streptococcus mutans and Staphylococcus aureus. *Trans. Nonferrous Met. Soc.* **2016**, *26*, 118–125. [CrossRef]
5.   Jurczyk, K.; Niespodziana, K.; Jurczyk, M.U.; Jurczyk, M. Synthesis and characterization of titanium-45S5 Bioglass nanocomposites. *Mater. Des.* **2011**, *32*, 2554–2560. [CrossRef]
6.   Moskalewicz, T.; Seuss, S.; Boccaccini, A.R. Microstructure and properties of composite polyetheretherketone/ Bioglass® coatings deposited on Ti-6Al-7Nb alloy for medical applications. *Appl. Surf. Sci.* **2013**, *273*, 62–67. [CrossRef]
7.   Ananth, K.P.; Suganya, S.; Mangalaraj, D.; Ferreira, J.M.F.; Balamurugan, A. Electrophoretic bilayer deposition of zirconia and reinforced bioglass system on Ti6Al4V for implant applications: An in vitro investigation. *Mater. Sci. Eng. C* **2013**, *33*, 4160–4166. [CrossRef]
8.   López, M.M.M.; Fauré, J.; Cabrera, M.I.E.; García, M.E.C. Structural characterization and electrochemical behavior of 45S5 bioglass coating on Ti6Al4V alloy for dental applications. *Mater. Sci. Eng. B* **2016**, *206*, 30–38. [CrossRef]
9.   Xue, B.; Guo, L.; Chen, X.; Fan, Y.; Ren, X.; Li, B.; Ling, Y.; Qiang, Y. Electrophoretic deposition and laser cladding of bioglass coating on Ti. *J. Alloy. Compd.* **2017**, *710*, 663–669. [CrossRef]

10. Boccaccini, A.R.; Peters, C.; Roether, J.A.; Eifler, D.; Misra, S.K.; Minay, E.J. Electrophoretic deposition of polyetheretherketone (PEEK) and PEEK/Bioglass® coatings on NiTi shape memory alloy wires. *J. Mater. Sci.* **2006**, *41*, 8152–8159. [CrossRef]

11. Estrada-Cabrera, E.; Torres-Ferrer, L.R.; Aztatzi-Aguilar, O.G.; De Vizcaya-Ruiz, A.; Meraz-Rios, M.A.; Zarate-Triviño, D.G.; Arizmendi-Morquecho, A.; Bugallo, A.D.L.; Prokhorov, E.; Luna-Barcenas, G. Chitosan-bioglass coatings on partially nanostructured anodized Ti-6Al-4V alloy for biomedical applications. *Surf. Coatings Technol.* **2019**, *375*, 468–476. [CrossRef]

12. Jugowiec, D.; Łukaszczyk, A.; Cieniek, Ł.; Kot, M.; Reczyńska, K.; Cholewa-Kowalska, K.; Pamuła, E.; Moskalewicz, T. Electrophoretic deposition and characterization of composite chitosan-based coatings incorporating bioglass and sol-gel glass particles on the Ti-13Nb-13Zr alloy. *Surf. Coatings Technol.* **2017**, *319*, 33–46. [CrossRef]

13. Moskalewicz, T.; Kot, M.; Seuss, S.; Kędzierska, A.; Czyrska-Filemonowicz, A.; Boccaccini, A.R. Electrophoretic deposition and characterization of HA/chitosan nanocomposite coatings on Ti6Al7Nb alloy. *Met. Mater. Int.* **2015**, *21*, 96–103. [CrossRef]

14. Popa, A.C.; Stan, G.E.; Enculescu, M.; Tanase, C.; Tulyaganov, D.U.; Ferreira, J.M.F. Superior biofunctionality of dental implant fixtures uniformly coated with durable bioglass films by magnetron sputtering. *J. Mech. Behav. Biomed. Mater.* **2015**, *51*, 313–327. [CrossRef]

15. Stan, G.E.; Popescu, A.C.; Mihailescu, I.N.; Marcov, D.A.; Mustata, R.C.; Sima, L.E.; Petrescu, S.M.; Ianculescu, A.; Trusca, R.; Morosanu, C.O. On the bioactivity of adherent bioglass thin films synthesized by magnetron sputtering techniques. *Thin Solid Films* **2010**, *518*, 5955–5964. [CrossRef]

16. Bellucci, D.; Bianchi, M.; Graziani, G.; Gambardella, A.; Berni, M.; Russo, A.; Cannillo, V. Pulsed Electron Deposition of nanostructured bioactive glass coatings for biomedical applications. *Ceram. Int.* **2017**, *43*, 15862–15867. [CrossRef]

17. Goller, G. The effect of bond coat on mechanical properties of plasma sprayed bioglass-titanium coatings. *Ceram. Int.* **2004**, *30*, 351–355. [CrossRef]

18. Chalisgaonkar, V.; Das, M.; Balla, V.K. Laser processing of Ti composite coatings reinforced with hydroxyapatite and bioglass. *Addit. Manuf.* **2018**, *20*, 134–143. [CrossRef]

19. Szesz, E.M.; Lepienski, C.M. Anodic bonding of titanium alloy with bioactive glass. *J. Non. Cryst. Solids* **2017**, *471*, 19–27. [CrossRef]

20. Krause, D.; Thomas, B.; Leinenbach, C.; Eifler, D.; Minay, E.J.; Boccaccini, A.R. The electrophoretic deposition of Bioglass® particles on stainless steel and Nitinol substrates. *Surf. Coatings Technol.* **2006**, *200*, 4835–4845. [CrossRef]

21. Durgalakshmi, D.; Balakumar, S.; Raja, C.A.; George, R.P.; Mudali, U.K. Structural, morphological and antibacterial investigation of Ag-impregnated sol-gel-derived 45S5 nanoBioglass systems. *J. Nanosci. Nanotechnol.* **2015**, *15*, 4285–4295. [CrossRef] [PubMed]

22. Durgalakshmi, D.; Rakkesh, R.A.; Balakumar, S. Stacked Bioglass/TiO$_2$ nanocoatings on titanium substrate for enhanced osseointegration and its electrochemical corrosion studies. *Appl. Surf. Sci.* **2015**, *349*, 561–569. [CrossRef]

23. Raja, C.A.; Balakumar, S.; Bargavi, P.; Rajashree, P.; Anandkumar, B.; George, R.P. Decoration of 1-D nano bioactive glass on reduced graphene oxide sheets: Strategies and in vitro bioactivity studies. *Mater. Sci. Eng. C* **2018**, *90*, 85–94.

24. Raja, C.A.; Balakumar, S.; Durgalakshmi, D.; George, R.P.; Anandkumar, B.; Kamachi Mudali, U. Reduced graphene oxide/nano-Bioglass composites: Processing and super-anion oxide evaluation. *RSC Adv.* **2016**, *6*, 19657–19661. [CrossRef]

25. Jin, G.; Cao, H.; Qiao, Y.; Meng, F.; Zhu, H.; Liu, X. Osteogenic activity and antibacterial effect of zinc ion implanted titanium. *Colloids Surfaces B Biointerfaces* **2014**, *117*, 158–165. [CrossRef]

26. Sergi, R.; Bellucci, D.; Candidato, R.T.; Lusvarghi, L.; Bolelli, G.; Pawlowski, L.; Candiani, G.; Altomare, L.; De Nardo, L.; Cannillo, V. Bioactive Zn-doped hydroxyapatite coatings and their antibacterial efficacy against Escherichia coli and Staphylococcus aureus. *Surf. Coatings Technol.* **2018**, *352*, 84–91. [CrossRef]

27. Wang, Y.; Zhao, S.; Li, G.; Zhang, S.; Zhao, R.; Dong, A.; Zhang, R. Preparation and in vitro antibacterial properties of anodic coatings co-doped with Cu, Zn, and P on a Ti–6Al–4V alloy. *Mater. Chem. Phys.* **2020**, *241*, 122360. [CrossRef]

28. Sedelnikova, M.B.; Komarova, E.G.; Sharkeev, Y.P.; Ugodchikova, A.V.; Mushtovatova, L.S.; Karpova, M.R.; Sheikin, V.V.; Litvinova, L.S.; Khlusov, I.A. Zn-, Cu- or Ag-incorporated micro-arc coatings on titanium alloys: Properties and behavior in synthetic biological media. *Surf. Coatings Technol.* **2019**, *369*, 52–68. [CrossRef]

29. Jin, G.; Qin, H.; Cao, H.; Qian, S.; Zhao, Y.; Peng, X.; Zhang, X.; Liu, X.; Chu, P.K. Synergistic effects of dual Zn/Ag ion implantation in osteogenic activity and antibacterial ability of titanium. *Biomaterials* **2014**, *35*, 7699–7713. [CrossRef]

30. Zhang, E.; Wang, X.; Chen, M.; Hou, B. Effect of the existing form of Cu element on the mechanical properties, bio-corrosion and antibacterial properties of Ti-Cu alloys for biomedical application. *Mater. Sci. Eng. C* **2016**, *69*, 1210–1221. [CrossRef]

31. Ma, Z.; Li, M.; Liu, R.; Ren, L.; Zhang, Y.; Pan, H.; Zhao, Y.; Yang, K. In vitro study on an antibacterial Ti-5Cu alloy for medical application. *J. Mater. Sci. Mater. Med.* **2016**, *27*. [CrossRef] [PubMed]

32. Wang, X.; Dong, H.; Liu, J.; Qin, G.; Chen, D.; Zhang, E. In vivo antibacterial property of Ti-Cu sintered alloy implant. *Mater. Sci. Eng. C* **2019**, *100*, 38–47. [CrossRef]

33. Liu, J.; Li, F.; Liu, C.; Wang, H.; Ren, B.; Yang, K.; Zhang, E. Effect of Cu content on the antibacterial activity of titanium-copper sintered alloys. *Mater. Sci. Eng. C* **2014**, *35*, 392–400. [CrossRef] [PubMed]

34. Zhang, E.; Ren, J.; Li, S.; Yang, L.; Qin, G. Optimization of mechanical properties, biocorrosion properties and antibacterial properties of as-cast Ti-Cu alloys. *Biomed. Mater.* **2016**, *11*, 065001. [CrossRef] [PubMed]

35. Zhang, E.; Li, F.; Wang, H.; Liu, J.; Wang, C.; Li, M.; Yang, K. A new antibacterial titanium-copper sintered alloy: Preparation and antibacterial property. *Mater. Sci. Eng. C* **2013**, *33*, 4280–4287. [CrossRef]

36. Zhang, Z.; Zheng, G.; Li, H.; Yang, L.; Wang, X.; Qin, G.; Zhang, E. Anti-bacterium influenced corrosion effect of antibacterial Ti-3Cu alloy in Staphylococcus aureus suspension for biomedical application. *Mater. Sci. Eng. C* **2019**, *94*, 376–384. [CrossRef]

37. Liu, R.; Tang, Y.; Zeng, L.; Zhao, Y.; Ma, Z.; Sun, Z.; Xiang, L.; Ren, L.; Yang, K. In vitro and in vivo studies of anti-bacterial copper-bearing titanium alloy for dental application. *Dent. Mater.* **2018**, *34*, 1112–1126. [CrossRef]

38. Liu, C.; Zhang, E. Biocorrosion properties of antibacterial Ti-10Cu sintered alloy in several simulated biological solutions. *J. Mater. Sci. Mater. Med.* **2015**, *26*, 142. [CrossRef]

39. Liu, R.; Memarzadeh, K.; Chang, B.; Zhang, Y.; Ma, Z.; Allaker, R.P.; Ren, L.; Yang, K. Antibacterial effect of copper-bearing titanium alloy (Ti-Cu) against *Streptococcus mutans* and *Porphyromonas gingivalis*. *Sci. Rep.* **2016**, *6*, 29985. [CrossRef]

40. Zhang, E.L.; Fu, S.; Wang, R.X.; Li, H.X.; Liu, Y.; Ma, Z.Q.; Liu, G.K.; Zhu, C.S.; Qin, G.W.; Chen, D.F. Role of Cu element in biomedical metal alloy design. *Rare Met.* **2019**, *38*, 476–494. [CrossRef]

41. Chen, M.; Yang, L.; Zhang, L.; Han, Y.; Lu, Z.; Qin, G.; Zhang, E. Effect of nano/micro-Ag compound particles on the bio-corrosion, antibacterial properties and cell biocompatibility of Ti-Ag alloys. *Mater. Sci. Eng. C* **2017**, *75*, 906–917. [CrossRef] [PubMed]

42. Lei, Z.; Zhang, H.; Zhang, E.; You, J.; Ma, X.; Bai, X. Antibacterial activities and biocompatibilities of Ti-Ag alloys prepared by spark plasma sintering and acid etching. *Mater. Sci. Eng. C* **2018**, *92*, 121–131. [CrossRef] [PubMed]

43. Vale, A.C.; Pereira, P.R.; Barbosa, A.M.; Torrado, E.; Alves, N.M. Optimization of silver-containing bioglass nanoparticles envisaging biomedical applications. *Mater. Sci. Eng. C* **2019**, *94*, 161–168. [CrossRef] [PubMed]

44. Sotoudehbagha, P.; Sheibani, S.; Khakbiz, M.; Ebrahimi-Barough, S.; Hermawan, H. Novel antibacterial biodegradable Fe-Mn-Ag alloys produced by mechanical alloying. *Mater. Sci. Eng. C* **2018**, *88*, 88–94. [CrossRef] [PubMed]

45. Vasilev, K.; Cook, J.; Griesser, H.J. Antibacterial surfaces for biomedical devices. *Expert Rev. Med. Devices* **2009**, *6*, 553–567. [CrossRef] [PubMed]

46. Chouirfa, H.; Bouloussa, H.; Migonney, V.; Falentin-Daudré, C. Review of titanium surface modification techniques and coatings for antibacterial applications. *Acta Biomater.* **2019**, *83*, 37–54. [CrossRef] [PubMed]

47. Marczewski, M.; Miklaszewski, A.; Maeder, X.; Jurczyk, M. Crystal Structure Evolution, Microstructure Formation, and Properties of Mechanically Alloyed Ultrafine-Grained Ti-Zr-Nb Alloys at $36 \leq \text{Ti} \leq 70$ (at. %). *Materials* **2020**, *13*, 587. [CrossRef]

48. Kowalski, K.; Jurczyk, M.U.; Wirstlein, P.K.; Jakubowicz, J.; Jurczyk, M. Influence of 45S5 Bioglass addition on microstructure and properties of ultrafine grained (Mg-4Y-5.5Dy-0.5Zr) alloy. *Mater. Sci. Eng. B* **2017**, *219*, 28–36. [CrossRef]

49. Miklaszewski, A.; Jurczyk, M.; Kaczmarek, M.; Paszel-Jaworska, A.; Romaniuk, A.; Lipińska, N.; Żurawski, J.; Urbaniak, P.; Jurczyk, M. Nanoscale size effect in in situ titanium based composites with cell viability and cytocompatibility studies. *Mater. Sci. Eng. C* **2017**, *73*, 525–536. [CrossRef]

50. Boyan, B.D.; Cohen, D.J.; Schwartz, Z. Bone Tissue Grafting and Tissue Engineering Concepts. In *Comprehensive Biomaterials II*; Elsevier: Amsterdam, The Netherlands, 2017; Volume 7, pp. 298–313, ISBN 9780128035818.

51. Van Vugt, T.A.; Geurts, J.A.P.; Arts, J.J.; Lindfors, N.C. Biomaterials in treatment of orthopedic infections. In *Management of Periprosthetic Joint Infections (PJIs)*; Woodhead Publishing: Sawston, UK, 2017; pp. 41–68, ISBN 9780081002421.

52. Mote, V.; Purushotham, Y.; Dole, B. Williamson-Hall analysis in estimation of lattice strain in nanometer-sized ZnO particles. *J. Theor. Appl. Phys.* **2012**, *6*, 6. [CrossRef]

53. Adamek, G.; Jakubowicz, J. Microstructure of the mechanically alloyed and electrochemically etched Ti-6Al-4V and Ti-15Zr-4Nb nanocrystalline alloys. *Mater. Chem. Phys.* **2010**, *124*, 1198–1204. [CrossRef]

54. Jurczyk, K.; Miklaszewski, A.; Jurczyk, M.U.; Jurczyk, M. Development of β type Ti23Mo-45S5 bioglass nanocomposites for dental applications. *Materials* **2015**, *8*, 8032–8046. [CrossRef] [PubMed]

55. Murray, J.L. The Cu-Ti (Copper-Titanium) system. *Bull. Alloy Phase Diagrams* **1983**, *4*, 81–95. [CrossRef]

56. Okamoto, H. Ti-Zn (Titanium-Zinc). *J. Phase Equilibria Diffus.* **2008**, *29*, 211–212. [CrossRef]

57. Murray, J.L. The Nb-Ti (Niobium-Titanium) System. *Bull. Alloy Phase Diagrams* **1981**, *2*, 55–61. [CrossRef]

58. Lin, K.L.; Lin, C.C. Ti₂ZrO phases formed in the titanium and zirconia interface after reaction at 1550 °C. *J. Am. Ceram. Soc.* **2005**, *88*, 1268–1272. [CrossRef]

59. Yang, D.; Guo, Z.; Shao, H.; Liu, X.; Ji, Y. Mechanical properties of porous Ti-Mo and Ti-Nb alloys for biomedical application by gelcasting. *Procedia Eng.* **2012**, *36*, 160–167. [CrossRef]

60. Cullinane, D.M.; Einhorn, T.A. Chapter 2—Biomechanics of Bone. In *Principles of Bone Biology*, 2nd ed.; Academic Press: Cambridge, MA, USA, 2002; pp. 17–32, ISBN 978-0-12-098652-1.

61. Geetha, M.; Singh, A.K.; Asokamani, R.; Gogia, A.K. Ti based biomaterials, the ultimate choice for orthopaedic implants—A review. *Prog. Mater. Sci.* **2009**, *54*, 397–425. [CrossRef]

62. Rodriguez-Florez, N.; Oyen, M.L.; Shefelbine, S.J. Insight into differences in nanoindentation properties of bone. *J. Mech. Behav. Biomed. Mater.* **2013**, *18*, 90–99. [CrossRef]

63. Nagels, J.; Stokdijk, M.; Rozing, P.M. Stress shielding and bone resorption in shoulder arthroplasty. *J. Shoulder Elb. Surg.* **2003**, *12*, 35–39. [CrossRef]

64. Apostu, D.; Lucaciu, O.; Berce, C.; Lucaciu, D.; Cosma, D. Current methods of preventing aseptic loosening and improving osseointegration of titanium implants in cementless total hip arthroplasty: A review. *J. Int. Med. Res.* **2018**, *46*, 2104–2119. [CrossRef] [PubMed]

65. Tang, L.; Thevenot, P.; Hu, W. Surface Chemistry Influences Implant Biocompatibility. *Curr. Top. Med. Chem.* **2008**, *8*, 270–280. [CrossRef] [PubMed]

66. Huan, Z.G.; Leeflang, M.A.; Zhou, J.; Duszczyk, J. ZK30-bioactive glass composites for orthopedic applications: A comparative study on fabrication method and characteristics. *Mater. Sci. Eng. B* **2011**, *176*, 1644–1652. [CrossRef]

67. Zaludin, M.A.F.; Jamaludin, S.B.; Idris, M.S.; Llah, N.A. Effect of 45S5 Bio-Glass Particles on Physical Properties and Corrosion Resistance of the Mg-5Zn Matrix Composite. *Open J. Met.* **2014**, *04*, 1–8. [CrossRef]

68. Tomashov, N.D.; Altovsky, R.M.; Chernova, G.P. Passivity and Corrosion Resistance of Titanium and Its Alloys. *J. Electrochem. Soc.* **1961**, *108*, 113. [CrossRef]

69. Gu, J.L.; Shao, Y.; Zhao, S.F.; Lu, S.Y.; Yang, G.N.; Chen, S.Q.; Yao, K.F. Effects of Cu addition on the glass forming ability and corrosion resistance of Ti-Zr-Be-Ni alloys. *J. Alloys Compd.* **2017**, *725*, 573–579. [CrossRef]

70. Clarke, J.K. On the Bacterial Factor in the Aetiology of Dental Caries. *Br. J. Exp. Pathol.* **1924**, *5*, 141.

71. Kumar, R.; Münstedt, H. Silver ion release from antimicrobial polyamide/silver composites. *Biomaterials* **2005**, *26*, 2081–2088. [CrossRef]

72. Ciobanu, C.S.; Massuyeau, F.; Constantin, L.V.; Predoi, D. Structural and physical properties of antibacterial Ag-doped nano-hydroxyapatite synthesized at 100 °C. *Nanoscale Res. Lett.* **2011**, *6*, 1–8. [CrossRef]

73. Kim, J.S.; Kuk, E.; Yu, K.N.; Kim, J.H.; Park, S.J.; Lee, H.J.; Kim, S.H.; Park, Y.K.; Park, Y.H.; Hwang, C.Y.; et al. Antimicrobial effects of silver nanoparticles. *Nanomed. Nanotechnol. Biol. Med.* **2007**, *3*, 95–101. [CrossRef]

74. Wong, M.S.; Chu, W.C.; Sun, D.S.; Huang, H.S.; Chen, J.H.; Tsai, P.J.; Lin, N.T.; Yu, M.S.; Hsu, S.F.; Wang, S.L.; et al. Visible-light-induced bactericidal activity of a nitrogen-doped titanium photocatalyst against human pathogens. *Appl. Environ. Microbiol.* **2006**, *72*, 6111–6116. [CrossRef] [PubMed]

75. Vincent, M.; Hartemann, P.; Engels-Deutsch, M. Antimicrobial applications of copper. *Int. J. Hyg. Environ. Health* **2016**, *219*, 585–591. [CrossRef] [PubMed]

76. Almoudi, M.M.; Hussein, A.S.; Abu Hassan, M.I.; Zain, N.M. A systematic review on antibacterial activity of zinc against *Streptococcus mutans*. *Saudi Dent. J.* **2018**, *30*, 283–291. [CrossRef] [PubMed]

77. Sirelkhatim, A.; Mahmud, S.; Seeni, A.; Kaus, N.H.M.; Ann, L.C.; Bakhori, S.K.M.; Hasan, H.; Mohamad, D. Review on zinc oxide nanoparticles: Antibacterial activity and toxicity mechanism. *Nano-Micro Lett.* **2015**, *7*, 219–242. [CrossRef]

78. Cossellu, G.; Motta, V.; Dioni, L.; Angelici, L.; Vigna, L.; Farronato, G.; Pesatori, A.C.; Bollati, V. Titanium and Zirconium levels are associated with changes in MicroRNAs expression: Results from a human cross-sectional study on obese population. *PLoS ONE* **2016**, *11*, e0161916. [CrossRef]

Oświadczenia współautorów o udziale w publikacjach

Poznań, dnia 5 listopada 2020 r.

dr hab. inż. Andrzej Miklaszewski
Instytut Inżynierii Materiałowej
Politechnika Poznańska
e-mail: andrzej.miklaszewski@put.poznan.pl

Oświadczenie

Niniejszym oświadczam, że w pracy M. Marczewski, **A. Miklaszewski**, M. Jurczyk, Structure evolution analysis in ultrafine-grained Zr and Nb-based beta titanium alloys, J. Alloys Compd. 765 (2018) 459–469. https://doi.org/10.1016/j.jallcom.2018.06.224. Mój udział polegał w wytworzeniu stopów Ti14Zr16Nb oraz Ti23Zr25Nb (at. %) metodą prasowania na gorąco, na wsparciu merytorycznym podczas analizy wyników i redagowania artykułu oraz byciu autorem korespondencyjnym. Jednocześnie wyrażam zgodę na wykorzystanie danych z tej publikacji na potrzeby przewodu doktorskiego Pana mgr inż. Mateusza Marczewskiego.
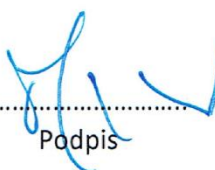
....
Podpis

prof. dr hab. Mieczysław Jurczyk
Instytut Inżynierii Materiałowej
Politechnika Poznańska
e-mail: mieczyslaw.jurczyk@put.poznan.pl

Poznań, dnia 5 listopada 2020 r.

Oświadczenie

Niniejszym oświadczam, że w pracy M. Marczewski, A. Miklaszewski, **M. Jurczyk**, Structure evolution analysis in ultrafine-grained Zr and Nb-based beta titanium alloys, J. Alloys Compd. 765 (2018) 459–469. https://doi.org/10.1016/j.jallcom.2018.06.224. Mój udział polegał na merytorycznej ocenie opracowanych wyników oraz artykułu. Jednocześnie wyrażam zgodę na wykorzystanie danych z tej publikacji na potrzeby przewodu doktorskiego Pana mgr inż. Mateusza Marczewskiego.

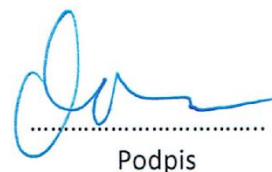...
Podpis

Poznań, dnia 5 listopada 2020 r.

dr hab. inż. Andrzej Miklaszewski
Instytut Inżynierii Materiałowej
Politechnika Poznańska
e-mail: andrzej.miklaszewski@put.poznan.pl

Oświadczenie

Niniejszym oświadczam, że w pracy M. Marczewski, **A. Miklaszewski**, X. Maeder, M. Jurczyk, Crystal Structure Evolution, Microstructure Formation, and Properties of Mechanically Alloyed Ultrafine-Grained Ti-Zr-Nb Alloys at 36 ≤ Ti ≤ 70 (at. %), Materials (Basel). 13 (2020). https://doi.org/10.3390/ma13030587. Mój udział polegał na wsparciu merytorycznym podczas analizy wyników oraz redagowania artykułu. Jednocześnie wyrażam zgodę na wykorzystanie danych z tej publikacji na potrzeby przewodu doktorskiego Pana mgr inż. Mateusza Marczewskiego.

....
Podpis

Thun, Switzerland, 05.11.2020

Xavier Maeder, Ph. D
Laboratory of Mechanics of Materials and Nanostructures
Swiss Federal Laboratories for Materials Science and Technology
(EMPA, Thun, Switzerland)
e-mail: xavier.maeder@empa.ch

Declaration

I hereby declare that as a part of scientific contribution, I was the co-author of the following paper:
M. Marczewski, A. Miklaszewski, **X. Maeder**, M. Jurczyk, Crystal Structure Evolution, Microstructure
Formation, and Properties of Mechanically Alloyed Ultrafine-Grained Ti-Zr-Nb Alloys at $36 \leq$ Ti ≤ 70 (at.
%), Materials (Basel). 13 (2020). https://doi.org/10.3390/ma13030587. My contribution to that paper
included electron backscatter diffraction (EBSD) measurements and analysis support of EBSD results. I
also approve of using the data from that paper in M.Eng. Mateusz Marczewski's Ph.D. dissertation

Signature

Poznań, dnia 5 listopada 2020 r.

prof. dr hab. Mieczysław Jurczyk
Instytut Inżynierii Materiałowej
Politechnika Poznańska
e-mail: mieczyslaw.jurczyk@put.poznan.pl

Oświadczenie

Niniejszym oświadczam, że w pracy M. Marczewski, A. Miklaszewski, X. Maeder, **M. Jurczyk**, Crystal Structure Evolution, Microstructure Formation, and Properties of Mechanically Alloyed Ultrafine-Grained Ti-Zr-Nb Alloys at $36 \leq Ti \leq 70$ (at. %), Materials (Basel). 13 (2020). https://doi.org/10.3390/ma13030587. Mój udział polegał na merytorycznej ocenie opracowanych wyników oraz artykułu. Jednocześnie wyrażam zgodę na wykorzystanie danych z tej publikacji na potrzeby przewodu doktorskiego Pana mgr inż. Mateusza Marczewskiego.

....
Podpis

Poznań, dnia 23 listopada 2020 r.

dr hab. n. med. Mieczysława Urszula Jurczyk
Katedra i Klinika Zdrowia Matki i Dziecka
Uniwersytet Medyczny im. Karola Marcinkowskiego w Poznaniu
e-mail: mjur@poczta.onet.pl

Oświadczenie

Niniejszym oświadczam, że w pracy M. Marczewski, **M.U. Jurczyk**, K. Kowalski, A. Miklaszewski, P.K. Wirstlein, M. Jurczyk, Composite and surface functionalization of ultrafine-grained Ti23Zr25Nb alloy for medical applications, Materials (Basel). 13 (2020). https://doi.org/10.3390/ma13225252. mój udział polegał w przeprowadzeniu testów biokompatybilności in vitro oraz analizie wyników tych badań. Jednocześnie wyrażam zgodę na wykorzystanie danych z tej publikacji na potrzeby przewodu doktorskiego Pana mgr inż. Mateusza Marczewskiego.

....
Podpis

dr inż. Kamil Kowalski
Instytut Inżynierii Materiałowej
Politechnika Poznańska
e-mail: kamil.kowalski@put.poznan.pl

Poznań, dnia 23 listopada 2020 r.

Oświadczenie

Niniejszym oświadczam, że w pracy M. Marczewski, M.U. Jurczyk, **K. Kowalski**, A. Miklaszewski, P.K. Wirstlein, M. Jurczyk, Composite and surface functionalization of ultrafine-grained Ti23Zr25Nb alloy for medical applications, Materials (Basel). 13 (2020). https://doi.org/10.3390/ma13225252. mój udział polegał na obserwacji powłoki po osadzaniu elektrochemicznym z wykorzystaniem skaningowego mikroskopu optycznego (widok przekroju poprzecznego) oraz wsparciu merytorycznym podczas analizy wyników oraz redagowania artykułu. Jednocześnie wyrażam zgodę na wykorzystanie danych z tej publikacji na potrzeby przewodu doktorskiego Pana mgr inż. Mateusza Marczewskiego.
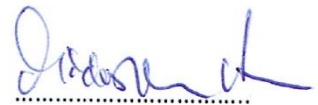
Podpis

dr hab. inż. Andrzej Miklaszewski
Instytut Inżynierii Materiałowej
Politechnika Poznańska
e-mail: andrzej.miklaszewski@put.poznan.pl

Poznań, dnia 23 listopada 2020 r.

Oświadczenie

Niniejszym oświadczam, że w pracy M. Marczewski, M.U. Jurczyk, K. Kowalski, **A. Miklaszewski,** P.K. Wirstlein, M. Jurczyk, Composite and surface functionalization of ultrafine-grained Ti23Zr25Nb alloy for medical applications, Materials (Basel). 13 (2020). https://doi.org/10.3390/ma13225252. mój udział polegał na obserwacji powłoki po osadzaniu elektrochemicznym z wykorzystaniem skaningowego mikroskopu optycznego (widok pochylony pod kątem 51° oraz analiza EDS – spektroskopii dyspersji energii) oraz wsparciu merytorycznym podczas analizy wyników oraz redagowania artykułu. Jednocześnie wyrażam zgodę na wykorzystanie danych z tej publikacji na potrzeby przewodu doktorskiego Pana mgr inż. Mateusza Marczewskiego.
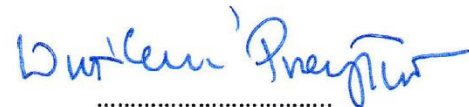
Podpis

Poznań, dnia 23 listopada 2020 r.

dr n. med. Przemysław Krzysztof Wirstlein
Katedra Ginekologii, Położnictwa i Onkologii Ginekologicznej,
Klinika Rozrodczości
Uniwersytet Medyczny im. Karola Marcinkowskiego w Poznaniu
e-mail: abys@wp.pl

Oświadczenie

Niniejszym oświadczam, że w pracy M. Marczewski, M.U. Jurczyk, K. Kowalski, A. Miklaszewski, **P.K. Wirstlein**, M. Jurczyk, Composite and surface functionalization of ultrafine-grained Ti23Zr25Nb alloy for medical applications, Materials (Basel). 13 (2020). https://doi.org/10.3390/ma13225252. mój udział polegał w przeprowadzeniu testów biokompatybilności in vitro oraz analizie wyników tych badań. Jednocześnie wyrażam zgodę na wykorzystanie danych z tej publikacji na potrzeby przewodu doktorskiego Pana mgr inż. Mateusza Marczewskiego.

....
Podpis

prof. dr hab. Mieczysław Jurczyk
Instytut Inżynierii Materiałowej
Politechnika Poznańska
e-mail: mieczyslaw.jurczyk@put.poznan.pl

Poznań, dnia 23 listopada 2020 r.

Oświadczenie

Niniejszym oświadczam, że w pracy M. Marczewski, M.U. Jurczyk, K. Kowalski, A. Miklaszewski, P.K. Wirstlein, **M. Jurczyk**, Composite and surface functionalization of ultrafine-grained Ti23Zr25Nb alloy for medical applications, Materials (Basel). 13 (2020). https://doi.org/10.3390/ma13225252 mój udział polegał na merytorycznej ocenie opracowanych wyników badań oraz artykułu a także kierowaniu projektem NCN. Jednocześnie wyrażam zgodę na wykorzystanie danych z tej publikacji na potrzeby przewodu doktorskiego Pana mgr inż. Mateusza Marczewskiego.
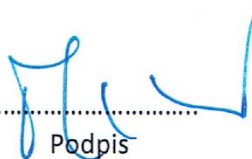
....
Podpis

prof. dr hab. Mieczysław Jurczyk
Instytut Inżynierii Materiałowej
Politechnika Poznańska
e-mail: mieczyslaw.jurczyk@put.poznan.pl

Poznań, dnia 5 listopada 2020 r.

Oświadczenie

Niniejszym oświadczam, że w pracy M. Marczewski, **M. Jurczyk**, P. Pecyna, M. Ratajczak, M. Gajecka, M.U. Jurczyk, The Effect of 45S5 Bioglass and Ag, Cu, or Zn Addition on the Crystal Structure, Properties, and Antibacterial Effect of Bulk Ti23Zr25Nb Biocomposites, Metals (Basel). 10 (2020) 1–23. https://doi.org/10.3390/met10091115. Mój udział polegał na merytorycznej ocenie opracowanych wyników oraz artykułu. Jednocześnie wyrażam zgodę na wykorzystanie danych z tej publikacji na potrzeby przewodu doktorskiego Pana mgr inż. Mateusza Marczewskiego.

....
Podpis

Poznań, dnia 5 listopada 2020 r.

mgr anal. med. Paulina Pecyna
Katedra i Zakład Genetyki i Mikrobiologii Farmaceutycznej
Uniwersytet Medyczny im. Karola Marcinkowskiego w Poznaniu
e-mail: paulinasawicka@ump.edu.pl

Oświadczenie

Niniejszym oświadczam, że w pracy M. Marczewski, M. Jurczyk, P. Pecyna, M. Ratajczak, M. Gajecka, M.U. Jurczyk, The Effect of 45S5 Bioglass and Ag, Cu, or Zn Addition on the Crystal Structure, Properties, and Antibacterial Effect of Bulk Ti23Zr25Nb Biocomposites, Metals (Basel). 10 (2020) 1–23. https://doi.org/10.3390/met10091115 mój udział polegał na realizacji badań aktywności bakteryjnej wytworzonych materiałów oraz współpracy w analizie wyników tych badań. Jednocześnie wyrażam zgodę na wykorzystanie danych z tej publikacji na potrzeby przewodu doktorskiego Pana mgr inż. Mateusza Marczewskiego.
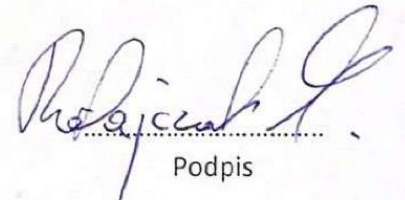
Paulina Pecyna
Podpis

dr n. farm. Magdalena Ratajczak
Katedra i Zakład Genetyki i Mikrobiologii Farmaceutycznej
Uniwersytet Medyczny im. Karola Marcinkowskiego w Poznaniu
e-mail: mratajczak@ump.edu.pl

Poznań, dnia 5 listopada 2020 r.

Oświadczenie

Niniejszym oświadczam, że w pracy M. Marczewski, M. Jurczyk, P. Pecyna, **M. Ratajczak**, M. Gajecka, M.U. Jurczyk, The Effect of 45S5 Bioglass and Ag, Cu, or Zn Addition on the Crystal Structure, Properties, and Antibacterial Effect of Bulk Ti23Zr25Nb Biocomposites, Metals (Basel). 10 (2020) 1–23. https://doi.org/10.3390/met10091115 mój udział polegał na wykonaniu badań aktywności bakteryjnej wytworzonych materiałów oraz współpracy w analizie wyników tych badań. Jednocześnie wyrażam zgodę na wykorzystanie danych z tej publikacji na potrzeby przewodu doktorskiego Pana mgr inż. Mateusza Marczewskiego.

....
Podpis

UNIWERSYTET MEDYCZNY IM. KAROLA MARCINKOWSKIEGO W POZNANIU
KATEDRA I ZAKŁAD GENETYKI I MIKROBIOLOGII FARMACEUTYCZNEJ
Kierownik Katedry prof. dr hab. Marzena Gajęcka
Adres:
ul. Święcickiego 4
60-781 Poznań

tel./fax. (061) 854 67 20
e-mail: bakterio@ump.edu.pl

Poznań, dnia 5 listopada 2020 r.

Oświadczenie

Oświadczam, że w pracy autorstwa M. Marczewski, M. Jurczyk, P. Pecyna, M. Ratajczak, **M. Gajecka**, M.U. Jurczyk, pt.: "The Effect of 45S5 Bioglass and Ag, Cu, or Zn Addition on the Crystal Structure, Properties, and Antibacterial Effect of Bulk Ti23Zr25Nb Biocomposites", Metals (Basel). 10 (2020) 1–23. https://doi.org/10.3390/met10091115, mój udział polegał na ocenie merytorycznej badań aktywności przeciwbakteryjnej wytworzonych materiałów. Jednocześnie wyrażam zgodę na wykorzystanie danych z tej publikacji na potrzeby przewodu doktorskiego Pana mgr inż. Mateusza Marczewskiego.

KIEROWNIK
Katedry i Zakładu
Genetyki i Mikrobiologii Farmaceutycznej

prof. dr hab. Marzena Gajęcka

dr hab. n. med. Mieczysława Urszula Jurczyk, prof. UM
Katedra i Klinika Zdrowia Matki i Dziecka
Uniwersytet Medyczny im. Karola Marcinkowskiego w Poznaniu
e-mail: mjur@poczta.onet.pl

Poznań, dnia 5 listopada 2020 r.

Oświadczenie

Niniejszym oświadczam, że w pracy M. Marczewski, M. Jurczyk, P. Pecyna, M. Ratajczak, M. Gajecka, **M.U. Jurczyk**, The Effect of 45S5 Bioglass and Ag, Cu, or Zn Addition on the Crystal Structure, Properties, and Antibacterial Effect of Bulk Ti23Zr25Nb Biocomposites, Metals (Basel). 10 (2020) 1–23. https://doi.org/10.3390/met10091115. Mój udział polegał w pomocy przy badaniach aktywności bakteryjnej wytworzonych materiałów oraz współpracy w analizie wyników tych badań. Jednocześnie wyrażam zgodę na wykorzystanie danych z tej publikacji na potrzeby przewodu doktorskiego Pana mgr inż. Mateusza Marczewskiego.

....
Podpis